

DESIGN OF BOOST CONVERTERS IN CORRELATION WITH  
EARTH-ABUNDANT MATERIAL BASED INDOOR  
PHOTOVOLTAIC DEVICES FOR LOW-POWER ELECTRONIC  
APPLICATIONS

by

Khandaker Akramul Haque

Student ID: 1015062116 P

A thesis submitted in partial fulfillment of the requirements of the degree

of

Master of Science in Electrical and Electronic Engineering



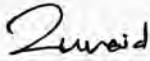

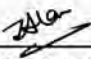


Department of Electrical and Electronic Engineering  
Bangladesh University of Engineering and Technology (BUET)  
Dhaka, Bangladesh

February 8, 2020

© Khandaker Akramul Haque 2020  
All Rights Reserved

The thesis titled "DESIGN OF BOOST CONVERTERS IN CORRELATION WITH EARTH-ABUNDANT MATERIAL BASED INDOOR PHOTOVOLTAIC DEVICES FOR LOW-POWER ELECTRONIC APPLICATIONS" submitted by Khandaker Akramul Haque, Student ID: 1015062116 P, Session: October 2015 has been accepted as satisfactory in partial fulfillment of the requirement for the degree of Master of Science in Electrical and Electronic Engineering on February 8, 2020.

### **BOARD OF EXAMINERS**

1.   
\_\_\_\_\_  
Dr. Md. Zunaid Baten  
Assistant Professor  
Department of Electrical and Electronic Engineering  
Bangladesh University of Engineering and Technology  
Dhaka, Bangladesh. Chairman  
(Supervisor)
2.   
\_\_\_\_\_  
Dr. Md. Shafiqul Islam  
Professor and Head  
Department of Electrical and Electronic Engineering  
Bangladesh University of Engineering and Technology  
Dhaka, Bangladesh. Member  
(Ex-Officio)
3.   
\_\_\_\_\_  
Dr. Mohammad Jahangir Alam  
Professor  
Department of Electrical and Electronic Engineering  
Bangladesh University of Engineering and Technology  
Dhaka, Bangladesh. Member
4.   
\_\_\_\_\_  
Dr. Md. Ziaur Rahman Khan  
Professor  
Department of Electrical and Electronic Engineering  
Bangladesh University of Engineering and Technology  
Dhaka, Bangladesh. Member
5.   
\_\_\_\_\_  
Dr. Md. Anwarul Abedin  
Professor  
Department of Electrical and Electronic Engineering  
Dhaka University of Engineering and Technology  
Gazipur, Bangladesh. Member  
(External)

# Declaration

It is hereby declared that this thesis or any part of it has not been submitted elsewhere for the award of any degree or diploma.

Signature of the student

A handwritten signature in black ink, consisting of stylized letters 'K' and 'H' followed by a horizontal line extending to the right.

---

(Khandaker Akramul Haque)

# Acknowledgement

First and foremost, all the praises and thanks to Allah, the Almighty for His showers of blessings throughout my research work to complete the research successfully.

I would like to express my sincere gratitude to my adviser Dr. Md Zunaid Baten, Assistant Professor of the Department of Electrical and Electronic Engineering, BUET, Dhaka for giving me the opportunity to do my research and providing invaluable guidance throughout my research work. I cannot thank enough for his vision, dynamism, sincerity and motivation. He has taught me the methodology to carry out my research work and present them as clearly as possible. In this pursuit he always encouraged me to push my boundaries towards excellence and for which I am greatly indebted to him. I would also like to thank him for his patience he had during the discussion of my work.

Finally, I would like to thank my parents and the members of my family for believing in me and constantly providing me support towards the completion of this work.

Khandaker Akramul Haque

February 8, 2020

# Abstract

This study focuses on the utilization of earth abundant materials for absorber layer of photovoltaic device, Cu based I<sub>2</sub>-II-IV-VI<sub>4</sub> quaternary kesterite Cu<sub>2</sub>ZnSn(S<sub>x</sub>Se<sub>1-x</sub>)<sub>4</sub> (CZTSSe) can be regarded as potential candidate. The constituent elements of this photo-absorber material are earth abundant and possess no severe threats in the environment sector. The theoretical Shockley-Queisser efficiency of CZTSSe is ~32% under AM 1.5. But unfortunately, the maximum possible efficiency achieved is 12.6% having  $V_{oc} = 513.4\text{mV}$ ,  $J_{sc} = 35.2 \text{ mA/cm}^2$  and fill factor = 69.8%. The chief reason for the lower efficiency is its lower  $V_{oc}$ . So, in this study the current champion cell termed as device A is taken as the standard and numerical modeling is done. In order to achieve higher efficiency an improved structure termed as device B has been proposed and compared with the current champion cell. The improved structure has a type II staggered type band structure unlike the type I straddling type band structure seen in device A. This resulted high  $V_{oc}$  but low  $J_{sc}$ . But the overall performance gain was the increase in efficiency. For indoor lighting condition the theoretical Shockley-Queisser efficiency limit is ~60%. Under indoor lighting condition the device A achieved an efficiency of 13.77% whereas device achieved an efficiency of 15.85%. The increase in the efficiency is attributed to higher photon yield for indoor lighting. As part of the study both the modeled device was connected with a power electronic converter to drive a small sensor node operating with a bias voltage of 5V. The converter used is a self-oscillating dc-dc converter based on the concept of boost converter. Since it is self-oscillating it does not require additional circuitry for driving the switch used in the converter and operates in discontinuous conduction mode (DCM). Device A performed better than device B with the self oscillating converter. On the other hand device B had better performance with a conventional boost converter in continuous conduction mode (CCM).

# Contents

<b>Declaration</b>	<b>iii</b>
<b>Acknowledgement</b>	<b>iv</b>
<b>Abstract</b>	<b>v</b>
<b>List of Figures</b>	<b>ix</b>
<b>List of Tables</b>	<b>xiii</b>
<b>1 Introduction</b>	<b>1</b>
1.1 Preface . . . . .	1
1.2 Literature Review . . . . .	3
1.3 Motivation of the Work . . . . .	8
1.4 Objectives of the Work . . . . .	10
1.5 Outline of the Dissertation . . . . .	11
<b>2 Theoretical Background</b>	<b>12</b>
2.1 Generalized Terms . . . . .	14
2.1.1 Short Circuit Current and Quantum Efficiency . . . . .	14
2.1.2 Dark Current, Photocurrent and Open Circuit Voltage . . . . .	15
2.1.3 Efficiency and Fill Factor . . . . .	17
2.1.4 Parasitic Resistance . . . . .	18
2.1.5 Spectral Irradiance . . . . .	20
2.1.6 Theory of Solar Cell . . . . .	21
2.2 Thin Film Solar Cell and Some Common Terms . . . . .	23
2.2.1 Vacuum Technique . . . . .	23
2.2.2 Non Vacuum Technique . . . . .	24

2.3	Material for Thin Film Solar Cell . . . . .	24
2.4	The Challenges of CZTSSe . . . . .	29
2.5	Theory of DC-DC Converters . . . . .	30
2.5.1	Linear Regulator . . . . .	30
2.5.2	Switched Mode Regulator . . . . .	31
<b>3</b>	<b>Performance Improvement</b>	<b>35</b>
3.1	Modeling of Device A . . . . .	36
3.1.1	Theoretical Modeling of Device A . . . . .	36
3.1.2	Theoretical Validation of Device A in AM 1.5 . . . . .	39
3.1.3	Parameters of Device A . . . . .	41
3.1.4	Performance Enhancement of Device A in Indoor Lighting Condition . . . . .	42
3.1.4.1	Detailed Balance Theory . . . . .	42
3.1.4.2	Generalized Shockley-Queisser Limit . . . . .	45
3.1.4.3	Performance Enhancement with White LED . . . . .	46
3.2	Modeling of Device B . . . . .	54
3.2.1	Type I and Type II Band Type Structure . . . . .	54
3.2.2	Performance Enhancement . . . . .	56
3.2.3	Parameters of Device B . . . . .	60
<b>4</b>	<b>Converter Circuit for Energy Harvesting with CZTSSe-based Solar Cell</b>	<b>62</b>
4.1	Converter Technology for Energy Harvesting . . . . .	64
4.1.1	Conventional Converter for Up Conversion of Voltage . . . . .	64
4.1.1.1	Output Response by Varying $V_{oc}$ of conventional boost converter . . . . .	66
4.1.1.2	Output Response by Varying $J_{sc}$ of conventional boost converter . . . . .	66
4.1.2	Oscillator Based Converter . . . . .	69
4.1.3	Output Response of Oscillator Based Converter . . . . .	71
4.1.3.1	Output Response by Varying $FF$ of Oscillator Based Converter . . . . .	72



4.1.3.2	Output Response by Varying $V_{oc}$ of Oscillator Based Converter . . . . .	72
4.1.3.3	Output Response by Varying $J_{sc}$ of Oscillator Based Converter . . . . .	72
4.2	Transient Analysis with Conventional Boost Converter . . . . .	75
4.2.1	Transient Analysis of Device A with Conventional Converter .	76
4.2.2	Transient Analysis of Device B with Conventional Converter .	76
4.3	Transient Analysis with Oscillator Based Converter . . . . .	78
4.3.1	Transient Analysis of Device A with Oscillator Based Converter	78
4.3.2	Transient Analysis of Device B with Oscillator Based Converter	79
4.4	Optimization of Oscillator Converter . . . . .	80
4.5	Output Response in Array Formation . . . . .	86
4.6	Discussion of Results . . . . .	89
<b>5</b>	<b>Conclusion</b>	<b>91</b>
5.1	Summary of the Work . . . . .	91
5.2	Scopes of Future Works . . . . .	95

# List of Figures

2.1	Quantum efficiency of CZTSSe as a function of wavelength . . . . .	15
2.2	Generalized photovoltaic response equivalent to an ideal diode in illuminated condition . . . . .	16
2.3	The current-voltage [red] and power-voltage [blue] relation with the maximum power point shown . . . . .	17
2.4	Equivalent circuit of a practical photovoltaic cell . . . . .	18
2.5	The effect of increasing $R_s$ on the current-voltage curve . . . . .	19
2.6	The effect of decreasing $R_{sh}$ on the current-voltage curve . . . . .	20
2.7	Indoor white LED and AM 1.5 spectral irradiance . . . . .	22
2.8	Electron-hole pair generation of a generalized solar cell . . . . .	23
2.9	The ideal dependence of $V_{oc}$ with band gap as compared to an ideal solar cell and various other thin film cells . . . . .	25
2.10	A basic linear regulator . . . . .	31
2.11	Circuit realization of (a) Buck Converter (b) Boost Converter and (c) Buck-Boost Converter . . . . .	33
3.1	$E$ plotted as a function of $k$ curve for a direct band gap semiconductor	36
3.2	$E$ plotted as a function of $k$ curve for an indirect band gap semiconductor	37
3.3	Illustration of the geometric description of device A . . . . .	38
3.4	Theoretically calculated current density vs. voltage and power density vs. voltage relations along with experimentally measured values reported for the champion CZTSSe solar cell . . . . .	40
3.5	Shockley-Queisser efficiency as a function of band gap for both indoor [white LED] and outdoor [AM 1.5 solar] lighting condition. [Inset: Spectral irradiance for indoor and outdoor lighting condition varying with wavelength] . . . . .	47
3.6	Current and power densities as a function of voltage in Device A . . . .	48

3.7	Efficiency and $FF$ as a function intensity under both indoor and solar illumination conditions in Device A . . . . .	49
3.8	Open circuit voltage ( $V_{oc}$ ) and short circuit current density ( $J_{sc}$ ) as a function intensity under both indoor and solar illumination conditions in Device A . . . . .	50
3.9	Relative enhancement of $J_{sc}$ , $V_{oc}$ , $FF$ and efficiency with respect to outdoor solar illumination conditions for varying intensities of the illuminating source . . . . .	50
3.10	Normalized integrated intensity (photon yield) as a function of photon energy for white LED and solar spectra . . . . .	51
3.11	External quantum efficiency (EQE) profiles for indoor and solar illumination condition in Device A along with the relative enhancement of EQE .	52
3.12	Spectral response for indoor and solar illumination along with the relative increase of spectral response for indoor illumination with respect to solar illumination condition . . . . .	53
3.13	Generation rates in different regions of Device A . . . . .	53
3.14	Generalized energy band diagram of type I (straddling) pn-heterojunction photovoltaic cell . . . . .	54
3.15	Generalized energy band diagram of type II (staggered) pn-heterojunction photovoltaic cell . . . . .	55
3.16	Schematic diagram of proposed device B . . . . .	56
3.17	J-V characteristics of Device B for both indoor and solar illumination conditions . . . . .	57
3.18	(a)Energy band diagram of device A and (b) Energy band diagram of device B at equilibrium condition . . . . .	57
3.19	(a) Energy band diagram of device A and (b) Energy band diagram of device B under indoor illumination condition . . . . .	58
3.20	$J_{sc}$ and $V_{oc}$ of device A and device B for different intensities of the illuminating white LED source. . . . .	59
3.21	Efficiency and $FF$ of device A and device B plotted as a function of the intensity of illuminating white LED . . . . .	59
4.1	A simple charge pump circuit diagram . . . . .	64

4.2	Circuit diagram of conventional boost converter with equivalent circuit of CZTSSe PV cell . . . . .	66
4.3	(a) $V_{out}$ as a function of $V_{oc}$ and (b) Efficiency as a function of $V_{oc}$ of conventional boost converter [Device A and Device B indicate the actual operating point] . . . . .	67
4.4	(a) $V_{out}$ as a function of $J_{sc}$ and (b) Efficiency as a function of $J_{sc}$ of conventional boost converter [Device A and Device B indicate the actual operating point] . . . . .	68
4.5	Block diagram of the design . . . . .	70
4.6	Circuit diagram of the converter . . . . .	71
4.7	(a) $V_{out}$ as a function of $V_{oc}$ and (b) Efficiency as a function of $V_{oc}$ [Device A and Device B indicate the actual operating point] . . . . .	73
4.8	(a) $V_{out}$ as a function of $J_{sc}$ and (b) Efficiency as a function of $J_{sc}$ of oscillator based converter [Device A and Device B indicate the actual operating point] . . . . .	74
4.9	Device A in CCM with conventional boost converter (a) $V_{in}$ and $I_{in}$ with time (b) $V_{out}$ with time [inset: $V_{out}$ with time in steady state] and (c) Inductor current ( $I_L$ ) with time . . . . .	77
4.10	Device A in DCM with conventional boost converter (a) $V_{in}$ and $I_{in}$ with time (b) $V_{out}$ with time [inset: $V_{out}$ with time in steady state] and (c) Inductor current ( $I_L$ ) with time . . . . .	78
4.11	Device B in CCM with conventional boost converter (a) $V_{in}$ and $I_{in}$ with time (b) $V_{out}$ with time [inset: $V_{out}$ with time in steady state] and (c) Inductor current ( $I_L$ ) with time . . . . .	79
4.12	Device B in DCM with conventional boost converter (a) $V_{in}$ and $I_{in}$ with time (b) $V_{out}$ with time [inset: $V_{out}$ with time in steady state] and (c) Inductor current ( $I_L$ ) with time . . . . .	80
4.13	Device A with oscillator-based converter (a) $V_{in}$ and $I_{in}$ with time (b) $V_{out}$ with time [inset: $V_{out}$ with time in steady state] and (c) Inductor current ( $I_L$ ) with time . . . . .	81

4.14	Device B with oscillator-based converter (a) $V_{in}$ and $I_{in}$ with time (b) $V_{out}$ with time [inset: $V_{out}$ with time in steady state] and (c) Inductor current ( $I_L$ ) with time . . . . .	82
4.15	(a) $V_{out}$ as a function of ripple capacitor $C_{out}$ and (b) Efficiency as a function of ripple capacitor $C_{out}$ of oscillator based converter . . . . .	84
4.16	(a) $V_{out}$ as a function of RC oscillator value pairs and (b) Efficiency as a function of RC oscillator value pairs of oscillator based converter	85
4.17	(a) Transient value of $V_{out}$ with $R_{out}$ at the highest optimized value, $C_{out}$ at the lowest optimized value and varying R, C [inset: steady state value of $V_{out}$ ]; (b) Transient value of $V_{out}$ with $R_{out}$ at the lowest optimized value, $C_{out}$ at the highest optimized value and varying R, C [inset: steady state value of $V_{out}$ ]; (c) Transient value of inductor current ( $I_L$ ) with $R_{out}$ at the highest optimized value, $C_{out}$ at the lowest optimized value and varying R, C; (d) Transient value of inductor current ( $I_L$ ) with $R_{out}$ at the lowest optimized value, $C_{out}$ at the highest optimized value and varying R, C . . . . .	87

# List of Tables

2.1	Voltage and current relation of common DC-DC converter [Here, $D$ is the duty cycle, $out$ and $in$ subscripts represent output and input parameters respectively] . . . . .	32
3.1	Values of material parameters used for Device A . . . . .	41
3.2	Values of material parameters used for Device B . . . . .	60
4.1	Varying $V_{oc}$ while keeping $FF$ and $J_{sc}$ constant for both device A and device B (CCM parameters are tabulated without parenthesis and DCM parameters are tabulated in parenthesis of conventional boost converter) . . . . .	67
4.2	Varying $J_{sc}$ while keeping $FF$ and $V_{oc}$ constant for both device A and device B (CCM parameters are tabulated without parenthesis and DCM parameters are tabulated in parenthesis of conventional boost converter) . . . . .	68
4.3	Parametric value of both device . . . . .	72
4.4	Varying $FF$ while keeping $V_{oc}$ and $J_{sc}$ constant for device B . . . . .	73
4.5	Varying $V_{oc}$ while keeping $FF$ and $J_{sc}$ constant for both device A and device B of oscillator based converter . . . . .	73
4.6	Varying $J_{sc}$ while keeping $FF$ and $V_{oc}$ constant for both device A and device B . . . . .	74
4.7	Opimization of the oscillator converter varying the output load and ripple capacitor . . . . .	83
4.8	Optimization of the oscillator converter varying the RC parameters of the oscillator taking the optimized value of the output load and ripple capacitor [the numerical values in parenthesis indicate optimization value pair for $R_{out}$ and $C_{out}$ ] . . . . .	84

4.9	Output response in array formation of the oscillator circuit with device B [The average values are tabulated] . . . . .	88
-----	---	----

# Chapter 1

## Introduction

### 1.1 Preface

The modern era has seen a rapid increase in the consumption of energy with everything now a days becoming interconnected and the term ‘smart’ is associated with every electrical apparatus that is seen around everywhere. Though these smart appliances are meant to be efficient in energy consumption the bulk increase in their sheer number means a massive rise in energy consumption. In order to meet this growing demand, an increase in the production of energy is required. Though many technological breakthroughs have been achieved in nanometer scale electronic devices by exploiting Moore’s law and operating these devices at a frequency unimaginable to the creators in their earlier phases, still a lot of reliance is seen in the conventional means for producing energy to drive these devices for their intended use. The conventional means of producing energy, means depending on fossil fuels which are rather depleting at an alarming state as of this day. The main leaders in charge of controlling such fossil fuels are imposing some of the harshest sanctions and as a result the price of such fossil fuels are increasing exponentially. This is just the economic side of things and when the environmental impact left by such conventional means are factored in a rather disastrous stage is seen. These means are producing most of the greenhouse gases which are further contributing to the global warming at an alarming level. The cumulative impact is the increase in the earth temperature leading to a rise in sea level and flooding the lower part of the earth. Then there is the impact of radiation which are the chief by product



of nuclear plants in the production of energy. All these effects have influenced the researchers to look for other forms of energy which are green and economical. With these ends in mind renewable sources can be viewed as a potential replacement.

Solar energy as a renewable form of energy has been the major focus of research for quite some time now. Solar cells connected in array formation are providing energy to the national grid though in limited amount and this has led to the traditional form of research in this field. Silicon is playing a major impact in this research where the main focus is to bulk produce energy economically. Though silicon is related with photovoltaic cells since its infant stage, it is getting rather expensive and with the bulk amount being mined every year it is being depleted from the earth crust at a rate unprecedented before. Despite silicon photovoltaic cells having the highest efficiency, current research has shifted its focus in finding alternative material which does not have the performance supremacy like silicon but can still provide energy at a degraded level by being economical. So, this traditional research has paved the path to modern research where the main focus is the heterojunction thin film photovoltaic cells which include GaAs, silicon, CdTe, GaInP, perovskites, kesterite, organics and dye sensitized materials.

Thin film photovoltaic cell is economical compared to silicon because most of the materials used in the thin film technology is direct optical band gap type where as in silicon it is indirect in nature. This particular characteristic causes the absorber layer in thin film to be a lot thinner (lying in the vicinity of 1 to 3  $\mu m$ ) compared to silicon (lying in the vicinity of 300 to 400  $\mu m$ ) which reduces the cost for material requirement. As a result, a lot more material throughput can be achieved with thin film technology which means better logistic handling capability as it is light weight; this impact could be cumulatively added with the decrease in cost of material fabrication in thin film technology. Besides they could also be fabricated in cheap substrates like plastic and glass. All these perks have their inherent disadvantages. Some of the materials used in the thin film photovoltaic cells are either expensive (being classified as rare earth element) or toxic to the environment which includes germanium (Ge), arsenic (As), gallium (Ga), cadmium

(Cd), indium (In) and tellurium (Te). This particular disadvantage has opened the door for yet another research group which deems it necessary for finding a cheap, easily available and non-toxic material for fabricating the absorber layer in thin film photovoltaic cell. A potential material in this regard is the quaternary kesterite  $\text{Cu}_2\text{ZnSnS}_4$  (CZTS) and its selenized counterpart  $\text{Cu}_2\text{ZnSn}(\text{S}_x\text{Se}_{1-x})_4$  (CZTSSe). All the constituent elements in this material is easily available and no particular toxicity that could affect the environment is reported with this material.

## 1.2 Literature Review

During 1973 the solar cells were becoming popular in the terrestrial environment along with its intended use in space. The bulk crystalline flat-plate silicon solar cell with an efficiency of 25% was used here [1, 2]. Also, at this time a shift towards multi-crystalline solar cells were also seen in terrestrial usage. It was revealed through research that highly efficient solar cells could be formed with multi-crystalline wafer when the individual crystals were more than 20 times larger than the optical absorption length [3].

After the discovery of electroless plating and light induced plating in current collecting technologies of single crystalline silicon solar cell technology highly efficient cells were made possible [4, 5]. Using the concept of electroless plating, laser buried grid PV cell was produced. In this cell laser grooves were formed in the front side of the cell which led to the formation of deep emitter resulting in lower contact resistance [6].

In 1989, a new type of silicon crystal cell called PERC (Passivated Emitter Rear Cell) with a photoconversion efficiency of 23.2% were developed having  $V_{oc}$  and  $J_{sc}$  as 700mV and  $41\text{mAcm}^{-2}$  respectively. This efficiency was achieved with efficient passivation of front and rear surface with silicon oxide layer which led to low recombination in the bulk silicon crystal [7]. In 1990 the PERC was further improved by the same group with a new concept leading to a cell known as the PERL (Passivated Emitter Rear Locally-diffused) cell. The PERL cell had an

efficiency of 24.7% having an improvement in both  $V_{oc}$  and  $J_{sc}$  to be 706mV and  $42.2\text{mAcm}^{-2}$ . This was achieved with three fold step firstly a highly boron-diffused area was introduced underneath the rear aluminum contact which reduced the contact resistance, secondly a deep junction was introduced which ensured effective isolation of recombination areas in the bulk material and finally a reduction of the distance of the rear contact as compared to PERC [8]. In 2003, a new concept of current collecting contact was introduced in the PV cell which is basically composed of copper wire with a low melting alloy coating in an optically transparent adhesive layer [9, 10]. In 2007, 22% efficient HIT (Heterojunction with Intrinsic Thin layer) cell was developed [11, 12]. In this cell high passivation of both the front and rear end was achieved by sandwiching ultrathin amorphous silicon layer with high quality n-type mono-crystalline silicon layer. In 2008, 23.4% efficient solar cell was developed by including localized current collecting contact, minimizing front-side recombination by removing front-side metallic current collecting contact and by optimization of light trapping [12, 13].

Thin film solar cell technology had its origin in the 1960s where  $\text{Cu}_2\text{S}/\text{CdS}$  (Copper Sulphide/Cadmium Sulphide) is regarded as the first flexible thin film solar cell and also the first to achieve a power conversion efficiency of 10% in 1981 [14]. The most common thin film solar cell technologies are the amorphous and micro-crystalline silicon cell,  $\text{Cu}(\text{In},\text{Ge})\text{Se}_2$  (Copper Indium Gallium Selenide) – based solar cell and  $\text{CdTe}$  (Cadmium Telluride) – based solar cell [15–17].

Hydrogenated amorphous silicon (a-Si:H) - based solar cell has its basic foundation in its energy band gap. It is known that the energy gap is derived from the crystal lattice, the amorphous silicon lacks the long-range periodic order unlike the crystalline silicon. This feature causes the formation of localized states leading to dangling bonds but still it is regarded as a useful material in the thin film solar cell technology [18]. In 1976 the first amorphous solar cell was made possible by incorporating two techniques. Firstly, hydrogen passivation lowered the defect density which led to photoconductivity and secondly, the novel breakthrough in the doping of amorphous silicon [19, 20]. With passivation taking into consideration

the defect density was still high in amorphous silicon so unlike other thin film technology a p-n junction cannot be incorporated in this thin film technology, instead a p-i-n structure is incorporated here [21]. There is another interesting feature in the amorphous silicon known as the Staebler–Wronski Effect (SWE) which is also known as the metastability of amorphous silicon. The conductivity of a-Si:H decreases with illumination but this can again be restored with annealing at 425K. This metastability created further recombination center and was a major limitation in thin film technology [22–24]. a-Si:H has a high band gap of 1.75eV which is rather high for a single junction solar cell and this caused the further research leading to the discovery of hydrogenated micro-crystalline silicon ( $\mu c$ -Si:H) having a band gap of 1.12eV. In 1990s the first successful fabrication of the  $\mu c$ -Si:H solar cell happened [25]. Cu(In,Ge)Se<sub>2</sub> and CdTe – based solar cells along with other relevant thin film technologies are detailed in **Chapter 2**.

In order to overcome the Shockley-Queisser efficiency limit the use of multijunction or tandem solar cell design made its way in the thin film technology [26]. Here each absorber layer has its own p-n or p-i-n junction. The optimum band-gap for a tandem solar cell are calculated in [27]. In this regard the III-V (Gallium Arsenide, GaAs; Germanium, Ge; Gallium Indium Arsenide, GaInAs and Gallium Indium Phosphide, GaInP) multijunction cells achieved great prominence and by using high optical concentration the power conversion efficiency of 40% is achieved under sunlight [28]. In 2008, power conversion efficiency of 40.8% under AM 1.5 was achieved with inverted III-V multijunction solar cell [29]. In order to achieve this efficiency grading of the lattice constant at the substrate surface was done.

The works described above are the most state-of-the-art technologies used in the inorganic photovoltaic industry starting from crystalline silicon to thin film and the present hybrid multijunction photovoltaic cells taking the advantage of concentrator. They all are tested under standard testing condition which is basically AM 1.5 solar spectrum.

The possible product design for operating photovoltaic devices under indoor lighting condition was undertaken by SYN-Energy project [30]. In this project crystalline silicon (c-Si), micro crystalline silicon ( $\mu c$ -Si), Gallium Arsenide (GaAs) and Copper Indium Sulphide (CIS) – based solar cells were taken into consideration. Here artificial lighting condition was used to mimic the solar spectrum. The underlying feature of this work was to vary the irradiance of the artificial lighting from 1 to 1000  $\text{Wm}^{-2}$  and plot the power conversion efficiencies of the solar cells used so that a possible trend could be obtained to get insight about the performance of such devices under low level of irradiance or what could be possibly described as the low lighting condition. Similar work has been done with twenty-one different solar cells based on eight different solar cell materials [31]. In this work fluorescent tube was used as the lighting source to vary the irradiance at an interval of 1 to 10  $\text{Wm}^{-2}$  and similar results of power conversion efficiency were obtained.

Another group of researchers used three types of thin film solar cell based on AlGaAs (Aluminum Gallium Arsenide), GaAs (thin) and GaAs (thick) material and compared the efficiency with a standard c-Si solar cell with a white phosphor LED [32]. They achieved an efficiency of 21% with AlGaAs - based solar cell under indoor lighting condition and based on their result such a solar cell could be used to power a mm-scale wireless sensor nodes. The same group modeled the GaAs-based thin film solar cell under indoor lighting condition and obtained a power conversion efficiency of 19% [33]. In this work they identified that the efficiency is limited by the open circuit voltage which is further limited by the dark current. The recombination taking place on both the bulk and side wall of the photovoltaic cell limited the performance and they predicted that by lowering the recombination, theoretical limit of 40% efficiency could be reached with the GaAs solar cell under indoor lighting condition.

Unlike the power conversion efficiency, power density could also be an underlying parameter for research of solar cell under indoor lighting condition [34]. Two types of lighting sources CFL (Compact Fluorescent Lamp) and commercial white LED

were used to compare the power density of III-V (GaAs and GaInP)- based solar cell with c-Si cell and dye sensitized solar cell (DSSC). In this work the III-V material based solar cell showed two times power density with respect to both c-Si and DSSC under both indoor lighting condition.

Taking the indoor lighting condition and the narrow spectrum LED source, a PV material based on the band gap is chosen for optimum performance [35]. The homojunction InGaP (Indium Gallium Phosphide) showed high power density and a power conversion efficiency of 29% as it has the lowest leakage current under both narrow and low lighting condition in this work.

One particular solar cell synthesized from  $\text{Sb}_2\text{S}_3$  (Antimony Sulphur) showed an efficiency of 9% under very low light intensity which is 5% of the sun's radiation and hence taken as analogous to indoor lighting condition. This experimental model is compared with amorphous silicon solar cell under same lighting condition and the synthesized solar cell proved superior [36].

Some organic solar cells are also experimentally modeled under indoor lighting. Flexible perovskite solar cell prepared by sol-gel method achieved an efficiency of 12.1% which is significantly higher when compared with a flexible dye sensitized solar cells [37]. Mesoscopic perovskite solar cell taking advantage of the low temperature fabrication process achieved an efficiency of 25% under indoor lighting condition [38].

Apart from the experimental work with photovoltaic cells under indoor lighting condition some theoretical models are also suggested. One diode and two resistor model solar cell used as an energy harvester under indoor lighting is compared with a commercially available photovoltaic cell to achieve an error level of 4.85% under visible lighting condition [39]. Another group developed a generalized model for calculating the performance of a solar cell under fluorescent, halogen and LED lighting. The model was used along side twelve commercially available photovoltaic cells and the performance was predicted as a function of increased distance from

the lighting source [40]. A numerical model was also developed to calculate the thermal performance of a photovoltaic cell under indoor lighting condition and hence predicted an optimized design for the solar cell [41].

A lot of work has been done regarding the device physics of a photovoltaic cell but little information is available about the output performance of a single photovoltaic cell when it is used to power a remote sensor node. Traditional DC-DC converters are employed as the driver circuit in between the solar cell and the sensor. But recent work had exploited the solid-state engineering and energy harvester driver circuit was fabricated by CMOS-MEMS process [42]. Other popular converter circuits are based on charge-pumps which is basically a voltage multiplier circuit taking the help of inverter in CMOS technology and DC-DC converter based on oscillator circuit [43, 44]. But a complete parametric understanding of the photovoltaic technology starting from the device physics to converter circuit and finally powering a sensor node is yet to be investigated in detail.

### 1.3 Motivation of the Work

Copper based  $I_2-II-IV-VI_4$  quaternary kesterite material, CZTSSe has two properties particularly inherent in the thin film technology. They are direct type optical band gap material and their width lies within a certain optimal range for photovoltaic cells. As a result, many research groups have been using it to fabricate thin film photovoltaic cell using vacuum, non-vacuum techniques. The particular IBM Watson (USA) group has achieved supremacy with CZTSSe material having a power conversion efficiency 12.6% which is regarded as the current champion CZTSSe thin film photovoltaic cell in this work despite the CZTSSe material has theoretical Shockley-Queisser efficiency of 32% under air mass 1.5 (AM 1.5) [45, 46]. The lower efficiency reported by this group is attributed to low open circuit voltage. In this work it has been reported about one particular structure that could achieve even higher efficiency under AM 1.5 compared to the current champion CZTSSe cell. This is referred here as the improved structure where the improvement has been achieved by a knowledge of band engineering and the change of the transparent conducting

oxide layer. All these researches are mere an incremental improvement to the earlier research based on silicon photovoltaic cells which in this study is referred as the traditional research focusing on the cheap means of energy production with the help of renewable source, the sun. This traditional research has also encouraged researchers to realize other aspects of thin film technology which has not been deemed important earlier. Such as the deployment of these thin film photovoltaic cells in strategic points without having any particular sun light. The new form of research is known as photovoltaic energy harvesting which is the conversion of light energy to electrical energy from diversified light sources without taking the sun light as a standard. This form of research takes the advantage of internet of things (IoT) where modern advancement both in computer and electronic fields have reduced the size of every electronic apparatus to such a minute level that all of the devices are forming an interconnected network mesh and this is basically IoT. These interconnections mean more energy and conventional form of energy supply may not be always suitable because such interconnections are most often situated at a remote location and having a source of energy particularly dedicated for each interconnection is both a waste of economy and the energy supply itself as such interconnections require very low energy. In these remote locations energy harvesting units may be placed which converts lights from commercially available LEDs and drives the interconnection. In this work a particular type of commercially available LED having 497 lumen and watt rating of 15W is taken as the standard which here is referred as the indoor lighting condition. Every lighting condition has a different spectral intensity which is explored with the CZTSSe photovoltaic cells and methods to improve the performance of the device under the given lighting condition are discussed. For the standard indoor lighting condition, the theoretical Shockley-Queisser efficiency limit is approximately 60% for the thin film CZTSSe single junction photovoltaic cell. This particular finding suggests that a lot of head room for the improvement of performance of the CZTSSe cell under the given indoor lighting condition is available. The next venture of this work is to form a physical link between the design physics realized with CZTSSe thin film photovoltaic cell and its performance with an energy harvesting power electronic converter. The energy harvesting unit is generally composed of a transducer which in this study



is both the champion CZTSSe cell (Device A) and the improved cell (Device B). The transducer converts ambient energy into electrical energy. The ambient energy in this study is varied from indoor lighting condition to outdoor lighting condition in order to gain physical insight with the performance of both the cells with the energy harvester. The energy harvester used in this study is a self-powered type requiring no additional supply for the harvester. The transducer itself drives the energy harvester. The energy harvester is required because at the interconnected mesh there are sensor nodes which typically have a bias voltage of approximately 5V but the output voltage from a single CZTSSe cell varies from 514 to 690 mV. So, the energy harvesting unit amplifies the voltage and since these nodes require very small power the current to drive such node sensor is sufficient from the CZTSSe cell. Being self-powered such energy harvesting unit is suitable for providing power in remote sensor node as it is light weight. This particular arrangement will replace the use of battery in such nodes and thus removes two drawbacks. Firstly, battery needs replacement and thus the life span of the harvesting unit is superior compared to the battery. Secondly, battery has toxic emission that is harmful for the environment and energy harvesting unit does not have such emission. These advantages will lead to the concept of deploy and forget, making the arrangement of self-powering in the truest sense.

## 1.4 Objectives of the Work

A lot of work has been done in thin film photovoltaic technology and particularly CZTSSe-based thin film photovoltaic cells. But very limited work has been done to model CZTSSe-based solar cell for indoor lighting condition. Also, the work related to the driver circuit to drive an external load with CZTSSe-based solar cell is little to none. Based on these concepts the main objectives of the works could be as follows:

1. To design and optimize a CZTSSe-based PV device in order to attain optimum performance characteristics considering operation under an indoor solid-state light source.

2. To correlate physics-based design parameters of the CZTSSe-based PV device with output characteristics of boost converters operating in continuous and discontinuous conduction modes and optimize the overall design accordingly.

## 1.5 Outline of the Dissertation

**Chapter 2** discusses the basic equations, definition and methodology particularly suitable for photovoltaic device physics. It focusses on a detailed background in thin film technology and particularly CZTSSe-based thin film photovoltaic cells, the present condition and future of this technology. It also discusses the theoretical concepts of common DC-DC converters.

**Chapter 3** discusses the theoretical model for the validation of CZTSSe-based thin film photovoltaic cell which uses Poisson's equation and continuity equation under optical generation-recombination conditions. This model is first validated for AM 1.5 solar radiation and taking these results as the standard this model is further validated for white LED, considered as the indoor lighting condition and under this indoor lighting condition improved performance is calculated. In order to improve the performance even more the device physics of the model is changed to obtain a better structure which is again modeled for both solar radiation (outdoor condition) and indoor condition. A better performance is documented for both the conditions.

**Chapter 4** discusses the converter circuit used for powering a sensor node with the modeled photovoltaic structures as discussed in chapter 3. The output performance of both the photovoltaic device is compared with an oscillator-based converter circuit and a conventional converter circuit. The inherent distinguishing feature between both these circuits are discussed further to obtain a general trend.

**Chapter 5** discusses the result of the works done in this study. Here focus is also given on the future work that could be done with the obtained results and finally draws a conclusion.

## Chapter 2

# Theoretical Background

Photovoltaic energy conversion takes the concept of light made of packets of energy called photons. The photons are frequency dependent energy source, visible in nature, which are sufficient to excite electrons bound into solids to higher energy levels. In basic matter these excited electrons within a short time relaxes back to their ground state but in photovoltaic matter because of having an asymmetry these excited electrons are pulled back before they can relax which forms a potential difference. Since they have a potential difference, they are suitable for driving an external load when the photovoltaic material is connected in a closed-circuit formation. This is just the basis of photovoltaic concept but the effectiveness of such concept in the practical world greatly depends on the choice of the appropriate photovoltaic material together with the external circuit in which it should be connected. In 1839 a similar effect was reported by Edmund Becquerel. In 1876 this concept was further enhanced by William Adams and Richard Day with a sample of selenium connected with heated platinum contact. But in 1894 Charles Fritts endeavor could be termed as large-scale production of solar cell where he used selenium in combination with gold and other material. In subsequent years more and more photovoltaic effect was observed in copper oxide, lead sulphide and thallium sulphide. The particular concept that lead to the development of such photovoltaic device lies in the asymmetric electronic junction with a semitransparent metal layer on top of a semiconductor layer. This asymmetric concept was observed by Goldman and Brodsky in 1914 where a barrier to current flow in metal-semiconductor junction was found. Later during 1930s, the theoretical

concept of metal-semiconductor barrier layer was developed by Walter Schottky.

During the earlier stage of research, the photoconductivity of the material had encouraged the researchers where they found that the photocurrent was proportional to the intensity of the light absorbed. All this encouragement led to the development of high-quality silicon wafer in 1950s with crystalline silicon. This development had a positive impact with manufacturing p-n junction in silicon. These p-n junctions had superior performance when compared to Schottky barriers. As a result, Chaplin, Fuller and Pearson together in 1954 developed the first silicon solar cell having a power conversion efficiency of 6% which was actually six times higher when compared to earlier attempts. But due to their exorbitant price tags they were not considered a suitable substitute for power production. Since they were light weight and had high reliability, they were widely used in space paired with satellite from 1950s to 1960s where cost was not a major concern.

During the 1970s the oil producing countries imposed sanctions which resulted much interest to look for alternate means of production energy, this was the time where actual research towards wide spread development of photovoltaic cells began. A lot of investment in photovoltaic technology resulted in much affordable price which actually caused photovoltaic cells to be used for practical usage other than in space. This was the time where interest was shown in other type of material apart from crystalline silicon. At this time research began with polycrystalline silicon, amorphous silicon and 'thin-film' material. Though the outcome was not very convincing but actual research towards the development of consumer grade photovoltaic technology began from this time.

Towards the later part of the 1990s deregulation in electricity market resulted in viable means of producing energy alternative to fossil fuel. In order to prove the viability of the deregulated electricity market a lot of investment resulted in the development of photovoltaic cell to be used as a substitute of conventional form of energy dependent on fossil fuel. This time could be attributed for the development of grid connected solar cells. Research towards the development modules and PV

systems began from this time.

In order to get a better understanding at the most advanced level of photovoltaic cell like thin film technology based on heterojunction material on which this study is greatly dependent some concepts basic to photovoltaic cells needs to be familiarized with.

## 2.1 Generalized Terms

The terms most commonly used in photovoltaic technology are discussed here.

### 2.1.1 Short Circuit Current and Quantum Efficiency

Photocurrent is dependent on the incident light which is further dependent on the quantum efficiency ( $QE$ ) and short circuit current ( $J_{sc}$ ). Quantum efficiency,  $QE(E)$  is the probability by which an incident photon having energy  $E$  will deliver an electron to the external circuit. This is as follows:

$$J_{sc} = q \int_0^{\infty} b_s(E)QE(E)dE \quad (2.1)$$

Here,  $q$  is the charge of an electron,  $b_s(E)$  is the photon flux density of the incident spectrum having photons within an energy band of  $E$  and  $E + dE$  per unit area per unit time.  $QE(E)$  is the inherent feature of a particular material and is dependent on the absorption coefficient, efficiency of charge separation and charge collection. In Figure 2.1 quantum efficiency profile of the CZTSSe material is shown with respect to wavelength,  $\lambda$ .

The quantum efficiency can be treated as a function of energy or wavelength. The basic relation between energy and wavelength follows:

$$E = \frac{hc}{\lambda} \quad (2.2)$$

Here,  $h$  is regarded as the Planck's constant and  $c$  is the speed of light in vaccum.

## 2.1.2 Dark Current, Photocurrent and Open Circuit Voltage

Connecting a load across the photovoltaic cell produces a potential difference and as a result a current is generated. This current flows opposite to the photocurrent which is found by subtracting the dark current from the short circuit current. The dark current can be generalized as the current that flows under bias voltage of  $V$  volt in the dark. This could be related to the ideal diode current equation to obtain the dark current having a rectifying behavior by the following:

$$J_{dark}(V) = J_0 \left( e^{\frac{qV}{kT}} - 1 \right) \quad (2.3)$$

Here,  $J_0$  is a characteristic constant,  $k$  is the Boltzmann constant and  $T$  is the degree in Kelvin.

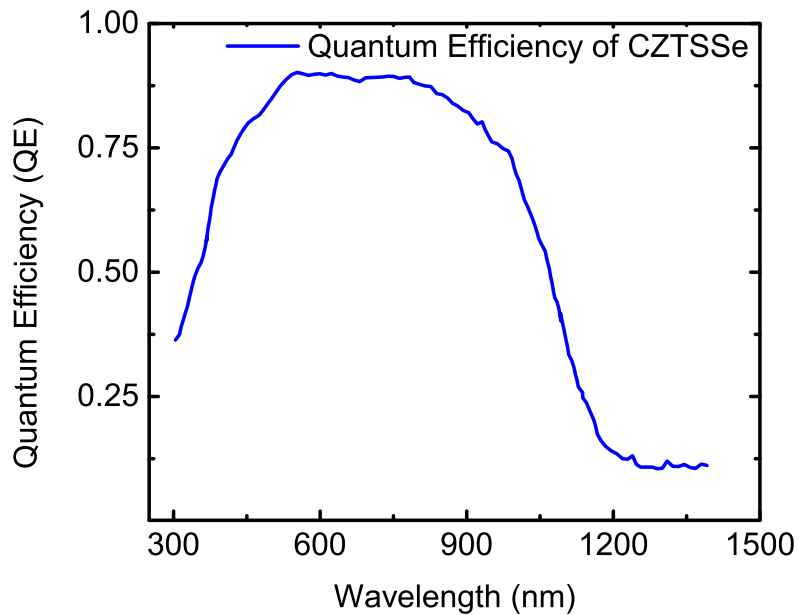


Figure 2.1: Quantum efficiency of CZTSSe as a function of wavelength

Thus, by using the concept of superposition, the photocurrent as the sum of the short circuit current and the dark current can be reached. There is a simplification involved in this concept as the dark current that generally flows under a bias voltage in illuminated condition is not exactly equal to the dark current that flows under a bias voltage in the dark, this simplification provides reasonable solution for most photovoltaic material and such this simplification is utilized in this study. The simplified result is as follows:

$$J(V) = J_{sc} - J_{dark}(V) = J_{sc} - J_0 \left( e^{\frac{qV}{kT}} - 1 \right) \quad (2.4)$$

The open circuit voltage ( $V_{oc}$ ) condition can be reached when the short circuit current ( $J_{sc}$ ) and the dark current ( $J_{dark}$ ) cancel each other out. This is given below:

$$V_{oc} = \frac{kT}{q} \ln \left( \frac{J_{sc}}{J_0} + 1 \right) \quad (2.5)$$

The simplified result is depicted in Figure 2.2.

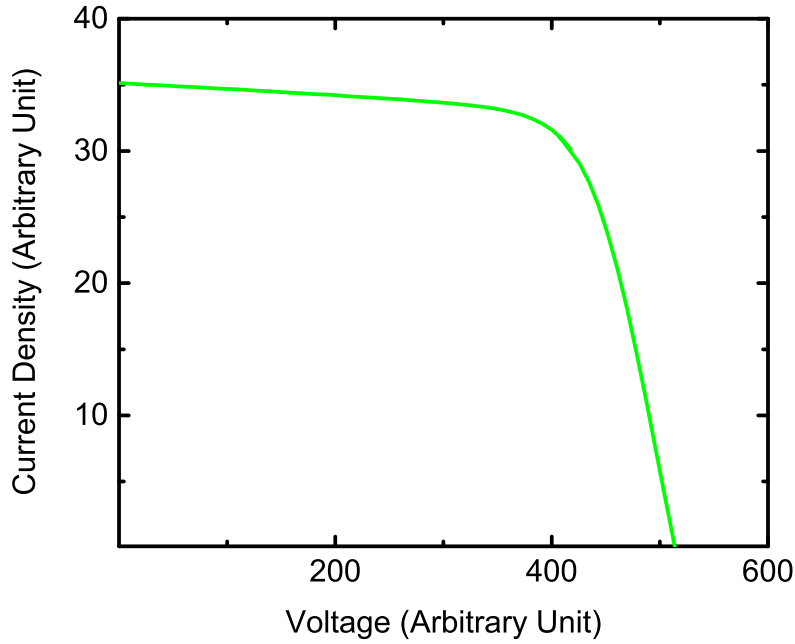


Figure 2.2: Generalized photovoltaic response equivalent to an ideal diode in illuminated condition

### 2.1.3 Efficiency and Fill Factor

Power density ( $P$ ) of a photovoltaic device follows:

$$P = JV \quad (2.6)$$

The power density reaches a maximum value at a particular point of voltage and current density which are symbolized as  $V_m$  and  $J_m$  respectively. This particular point is popularly known as the maximum power point. If a particular load having a resistance equal to the ratio  $V_m/J_m$  connected across the photovoltaic device, the photovoltaic device can be said to be operating at the maximum power point. From this concept fill factor ( $FF$ ) can be calculated which provides a lot of information regarding the efficiency and inherent property of the photovoltaic device as given below:

$$FF = \frac{J_m V_m}{J_{sc} V_{oc}} \quad (2.7)$$

The maximum power point of a photovoltaic device is depicted in Figure 2.3.

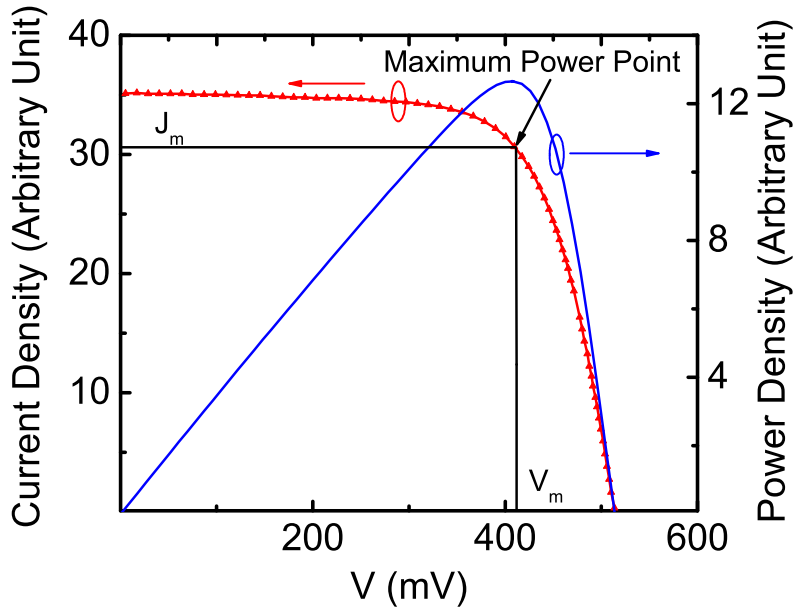


Figure 2.3: The current-voltage [red] and power-voltage [blue] relation with the maximum power point shown

The power conversion efficiency ( $\eta$ ) can be defined from the power density ( $P_s$ )



of the incident spectrum at the maximum power from the knowledge of the  $FF$  by the following:

$$\eta = \frac{J_m V_m}{P_s} = \frac{J_{sc} V_{oc} FF}{P_s} \quad (2.8)$$

The basic parameters that could be regarded as the performance indicator of a particular photovoltaic device are the  $V_{oc}$ ,  $J_{sc}$ ,  $V_m$ ,  $J_m$ ,  $FF$  and  $\eta$ . These parameters are widely used throughout this study.

### 2.1.4 Parasitic Resistance

In a practical photovoltaic cell due to having imperfections power is dissipated through contacts. There are also the effects of leakage current around the side of the device. These effects could be lumped up together in the broad term of the parasitic resistance which are commonly known as the series resistance ( $R_s$ ) and the shunt resistance ( $R_{sh}$ ). These are shown in the real equivalent circuit of a photovoltaic cell which is an ideal current source in parallel with a diode and parasitic resistances connected accordingly in Figure 2.4.

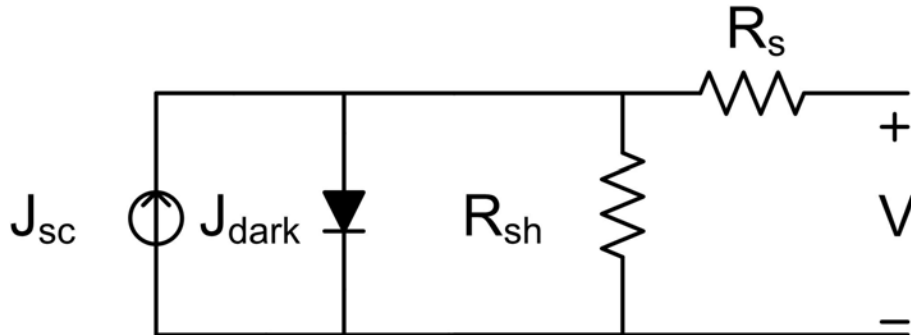


Figure 2.4: Equivalent circuit of a practical photovoltaic cell

The effect of parasitic resistances is shown in Figure 2.5 and Figure 2.6 from which a clear understanding that it drastically reduces the  $FF$  of the photovoltaic cell can be reached.

When the cumulative effect of the parasitic resistance is considered the photocurrent equation deviates from the ideal diode equation as given below:

$$J = J_{sc} - J_0 \left( e^{\frac{q(V+JAR_s)}{kT}} - 1 \right) - \frac{V + JAR_s}{R_{sh}} \quad (2.9)$$

So far, it has been discussed about the ideality of a diode while describing the photovoltaic cell which seldom holds true. In order to get a real understanding of the photovoltaic cell it is needed to consider non ideality effect ( $n$ ) which is a voltage dependent parameter usually lying between 1 and 2. It is as per the following equation:

$$J = J_{sc} - J_0 \left( e^{\frac{qV}{nkT}} - 1 \right) \quad (2.10)$$

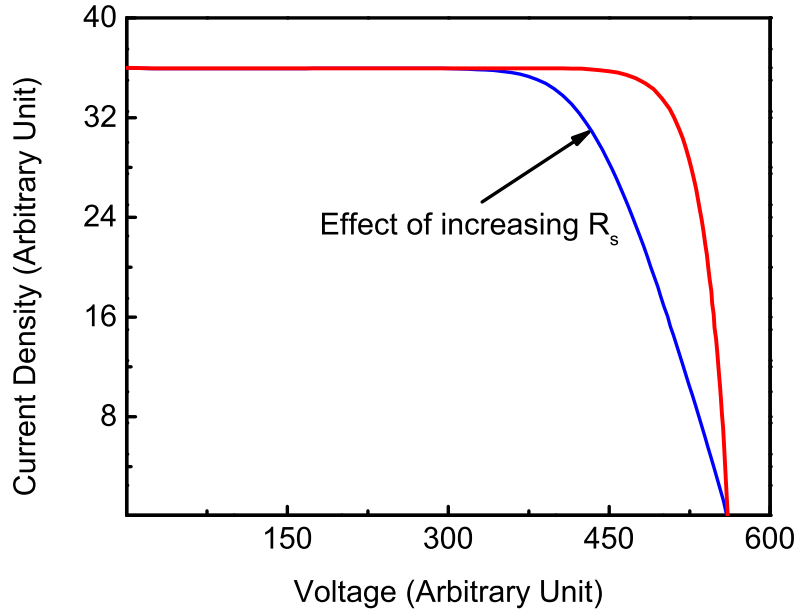


Figure 2.5: The effect of increasing  $R_s$  on the current-voltage curve

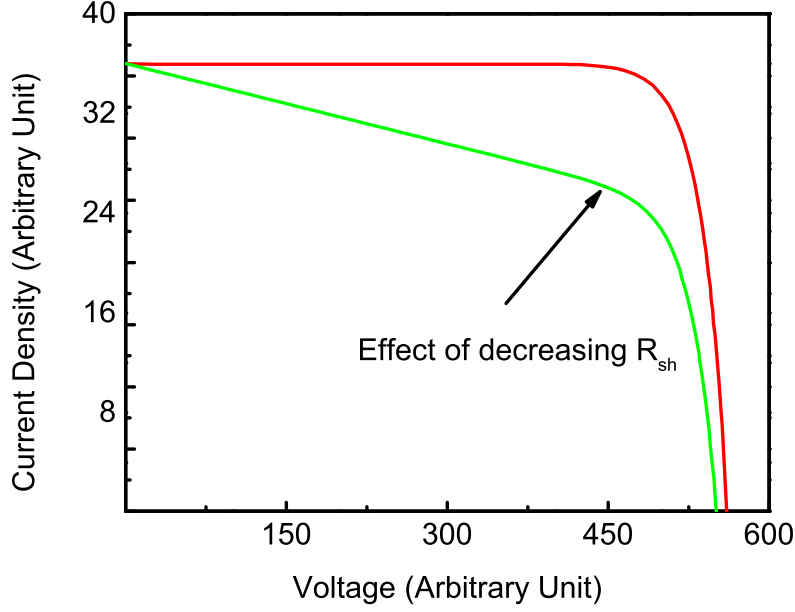


Figure 2.6: The effect of decreasing  $R_{sh}$  on the current-voltage curve

### 2.1.5 Spectral Irradiance

While describing a photovoltaic cell the most common form of spectrum that is encountered is the sunlight. The spectrum can be considered as a packet of energy or photon. This photon is modeled as unit of energy following Planck's equation as discussed previously in Equation 2.2.

The irradiance from a source is the amount of radiant energy per unit area per unit time. The solar spectrum is the combination of light having wavelength ranging from the ultraviolet region to the infrared region. This has most of the irradiance lumped up in the visible wavelength (300nm to 800nm).

The solar spectrum is modeled using a black body. The black body radiates photon with a distribution of energy. The shape of such is dependent on the characteristic temperature ( $T_s$ ).  $T_s$  having the value of 5760 K is usually taken as standard while describing black body. The spectral photon flux of a black body follows:

$$b_s(E) = \frac{2F_s}{h^3 c^2} \left( \frac{E^2}{e^{\left(\frac{E}{kT_s}\right)} - 1} \right) \quad (2.11)$$

Here  $F_s$  is the geometrical factor which describes the angular range from the

black body to the surface. This is further given by the following:

$$F_s = \pi \sin^2 \theta_{sun} \quad (2.12)$$

Here,  $\theta_{sun}$  is the half angle subtended by the black body to the surface from where the flux is measured. From earth the standard value of this angle is taken to be  $0.26^\circ$ . As a result, the value of  $F_s$  becomes  $2.16 * 10^{-5} \pi$ . Thus, the irradiance of the black body follows:

$$L(E) = E b_s(E) \quad (2.13)$$

Integrating the Equation 2.13 over the full energy range of the spectrum gives the total power density emitted from a black body. This gives the power density on the surface of the sun to be  $62 \text{ MWm}^{-2}$ . Just outside the earth's atmosphere this value reduces to  $1353 \text{ Wm}^{-2}$ . The earth's atmosphere further filters out part of spectrum reducing the value to be around  $900 \text{ Wm}^{-2}$  as measured on the earth's surface. It has become a generic convention to use a standard value for the solar irradiance while measuring the performance of a photovoltaic cell. This is regarded as air mass 1.5 or in more general case AM 1.5.  $1000 \text{ Wm}^{-2}$  is the value of this standard.

Moreover, photovoltaic cell could be used to harvest energy from indoor lighting condition. Its methodology is provided in the next chapter. The Figure 2.7 shows the solar irradiance with an indoor LED light spectrum used in this study.

## 2.1.6 Theory of Solar Cell

When photon having sufficient energy impinges on a solar cell three particular phenomena may take place. They are given in the next page:

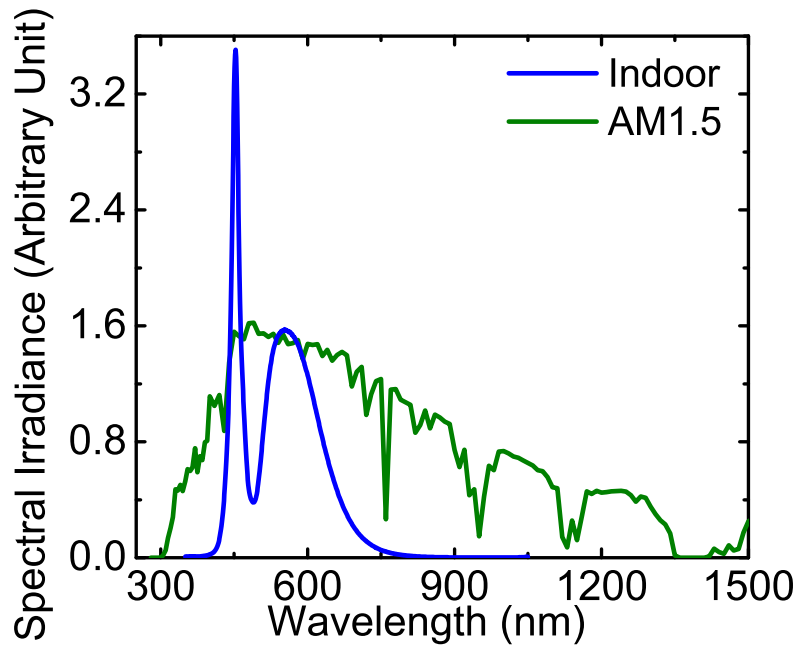


Figure 2.7: Indoor white LED and AM 1.5 spectral irradiance

1. The photon may pass straight through the solar cell when the energy of photon is very low.
2. The photon may get reflected off from the solar cell.
3. In most cases when the energy of photon is higher than the band gap of the solar cell, the photon energy gets absorbed by the solar cell and this particular phenomenon is the driving force behind the operation of solar cell.

When photon energy gets absorbed by the solar cell, the amount of energy which is higher than the band gap of the solar cell may get radiated either as phonon (heat) or photon (light) depending on the particular structure of the solar cell. The amount of energy which gets absorbed by the solar cell is given to an electron residing on the valence band of the solar cell. This excites the electron into the conduction band and a subsequent vacancy is created in the valence band which is popularly regarded as hole. Now in this case neighboring electrons in the valence band come up to fill up this hole and the process continues as long as there is the presence of photon energy. Thus photon energy causes the generation of electron-hole pair. Now if this solar cell is connected to a load the electron-hole pair causes the generation of current in the load. This particular phenomenon is depicted in Figure 2.8.

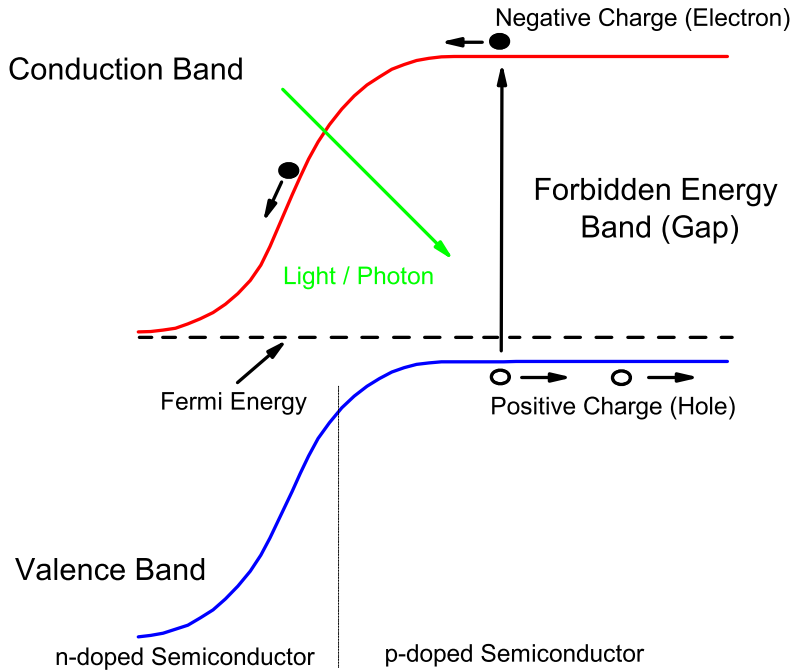


Figure 2.8: Electron-hole pair generation of a generalized solar cell

## 2.2 Thin Film Solar Cell and Some Common Terms

In the basic device structure of thin film solar cell substrate and superstrate configuration are quite popular. The substrate configuration is such that light first enters the solar cell and then it impinges on the substrate. This method allows for using any type of material like glass, stainless steel or the choice demanded by deposition technique used. In superstrate configuration light first hits the substrate and then enters the solar cell. So, in this case the material should be transparent and glass is the first choice of preference.

### 2.2.1 Vacuum Technique

It is the expensive form of deposition technique used in thin film technology which takes into consideration of co-sputtering, co-evaporation and pulsed laser deposition. Besides there is other method broadly incorporated in vacuum technique which is popularly known as a two-step method. In this method a layer known as the precursor is first incorporated with sputtering or evaporation followed by annealing.

## 2.2.2 Non Vacuum Technique

This form of deposition technique is the cost effective one and does not require any complex methodology and expensive tools used in the vacuum technique. This is a broad term which includes the process of spin on deposition, screen printing and spray deposition (spray pyrolysis).

## 2.3 Material for Thin Film Solar Cell

Towards the later part of the 1960s different types of experimental combination both with n-type and p-type absorber layer was done. Indium phosphide (InP) was a material of higher interest during that time as it had an inherent n-type conductivity in its undoped state. This particular material when doped with zinc (Zn) or cadmium (Cd) to make InP, a p-type material showed better rectification in the dark compared with the n-type single crystal. From a generic concept it is often found that the dark current-voltage curve is proportional to the illuminated curve. This particular discovery paved the way of using more p-type material to be used as the absorber layer. In the Figure 2.9 a basic relation between  $V_{oc}$  and band gap compared to an ideal solar cell and the materials that are used in the thin film technology are shown. This graph provides a reference for an optimal absorber layer and how far the theoretical limit of  $V_{oc}$  could be reached with that absorber layer [47, 48].

Zinc phosphide has a naturally occurring polymorphic characteristic. First successful use of polycrystalline  $Zn_3P_2$  as a Schottky barrier solar cell showed a conversion efficiency of 6% [49]. This research showed that zinc phosphide has a direct band gap and because of its much abundance in the earth, it became a major subject in the research of thin film technology. It was reported later that though the value of the band gap is 1.38 eV, the transition of electron is of indirect nature [50]. This group later fabricated solar cell with an efficiency of 4.5% and  $V_{oc}$  of 0.41 V [51]. In later attempt a heterojunction was formed with n-type  $In_2O_3$  and p-type  $ZnP_2$  which improved  $V_{oc}$  to be 0.5 V [52]. This attempt proved that the band gap of the material is within optimal limit to consider zinc phosphide as

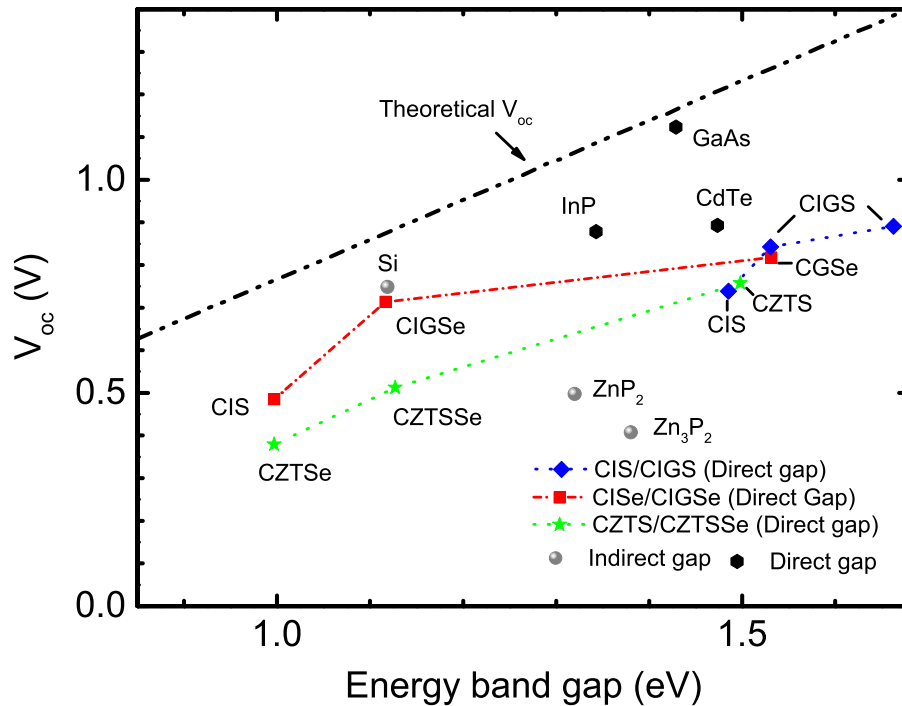


Figure 2.9: The ideal dependence of  $V_{oc}$  with band gap as compared to an ideal solar cell and various other thin film cells

a suitable photovoltaic material but the open circuit voltage obtained was quite low. This further imposed that the band gap of this material is of indirect type. Another possible reason behind the low open circuit voltage is the Fermi level pinning which happens due to the presence of high interface state density (more than  $10^{13} \text{ eV}^{-1}\text{cm}^{-2}$ ) preventing the formation of barrier [53]. This caused the researcher to look for other thin film material.

The use of gallium arsenide (GaAs) in thin film technology introduced a form of etching known as epitaxial lift off which became quite popular in manufacturing of highly efficient solar cell. The researcher used n-type GaAs on p-type GaAs layer. Then they later peeled off the n-type GaAs with a selective chemical etchant. The efficiency of this particular solar cell reached 13.5% [54]. Currently the record 29.1% efficient GaAs solar cell has been developed by Alta Devices [12].

A new line of researchers formed a heterojunction with n-type cadmium sulphide (CdS) and p-type indium phosphide (InP) having a power conversion efficiency of 4.2%. The low efficiency resulted due to the formation of a thick window layer



of CdS and undesirable reaction at the heterojunction interface [55]. In a later attempt the CdS layer was replaced with indium oxide ( $\text{In}_2\text{O}_3$ ). This resulted in a conversion efficiency of 11.6% [56]. It was also revealed in a following research that the efficiency of the  $\text{In}_2\text{O}_3$  and InP heterojunction photovoltaic cell could be increased to 16.3% if the oxide films were deposited in two steps [57]. A unique method was realized with a window layer of n-type zinc oxide (ZnO), a buffer layer of n-type CdS and an absorber layer of InP. The open circuit voltage and  $FF$  of this particular formation reached 0.75 V and 72% respectively. This resulted in a power conversion efficiency of 17.4% which is the highest among InP material without lattice matching [58]. In this method it was also found that the efficiency deteriorated to 10.6% when the buffer layer is removed. This was attributed to the formation of a dead zone resulting in the decrease of both short circuit current and  $FF$ . The dead zone is regarded as the conversion of the surface of p-type InP to n-type. It is reported that a pn-homojunction InP solar cell holds the record of 22% power conversion efficiency [59]. The degraded performance of the heterojunction solar cell was mainly due to the discontinuity of conduction band and parameter mismatch between CdS, ZnO and InP.

The initial development of cadmium telluride (CdTe) based solar cell used n-type CdS and p-type CdTe on top of glass. This though had a power conversion efficiency of only 1% which was very low but this structure paved the way for most of the modern CdTe-based solar cell [60]. A heterojunction solar cell was formed by creating a junction between p-type CdTe and n-type indium oxide ( $\text{In}_2\text{O}_3$ ) with a power conversion efficiency of 14.4% and open circuit voltage of 0.892 V [61]. This is the highest  $V_{oc}$  achieved with a CdTe-based solar cell. This solar cell further influenced research where it was revealed that CdTe which is generally heavily doped could be paired with lightly doped  $\text{In}_2\text{O}_3$  to improve the open circuit voltage [62]. Another finding of the highest  $V_{oc}$  of CdTe-based solar cell also proved quite influential which is the removal of a buffer layer between the window and absorber layer. The common trend was to use a buffer layer to eliminate any cause of radiation damage in the absorber layer but this was not the case in the CdTe-based solar cell. A record efficiency of 20.4% was manufactured

by First Solar using this very concept [12]. Moreover, in CdTe band engineering is possible by addition of mercury (Hg) and manganese (Mn) [63]. This feature gave rise to a concept of two terminal tandem solar cell by incorporating  $\text{Cd}_{1-x}\text{Hg}_x\text{Te}$  and  $\text{Cd}_{1-x}\text{Mn}_x\text{Te}$  as absorber layer [64].

During the initial phase of copper indium gallium selenide (CIGS)-based solar cell instead of the quaternary material the ternary CIS material was the major material used in the development of solar cells. A heterojunction solar cell with  $\text{In}_2\text{O}_3/\text{CdS}/\text{CIS}$  with an efficiency of 9.7% was the initial cell that influenced the researchers to further investigate the CIS and CIGS material [65]. This also led to the use of sulphide in the first commercially available module [21]. In later research it was revealed that the alloying of CIS absorber layer with Ga improved the efficiency of solar cell to be more than 10% [66]. In order to achieve this alloyed configuration Ga was first deposited on molybdenum (Mo) coated glass. On top of this layer Cu/In in a ratio of 1.5 was deposited and the whole configuration was sulfurized. This led to an efficiency of 10.5% and  $V_{oc}$  of 0.717V. This procedure allowed Ga to be deposited near the film-substrate interface which meant an effective back surface field with a diminishing nature towards the top surface having  $\text{Ga}/(\text{Ga}+\text{In})$  to be 2%. But in the formation of such layer enough care is necessary that secondary phase does not form which could reduce both short circuit current density and  $FF$ . A unique way to achieve this was to keep the ratio of  $\text{Ga}/(\text{Ga}+\text{In})$  less than 0.2 [67]. In the following research it was revealed that performance of the CIGS actually increased with addition of Ga, though at first it was observed that CdS/CIS heterojunction had a type II, staggered type band gap, which means low  $V_{oc}$ , it was not to be the case as  $V_{oc}$  actually increased with Ga. Using this concept, a new form of solar cell was formed with CIS absorber and  $\text{CuGaS}_2$  bottom layer. This solar cell had an efficiency of 13% [68]. A record efficiency of 20.8% was reached with CIGS absorber layer, cadmium sulphide (CdS) buffer layer and zinc oxide (ZnO) window layer [12, 69].

All the thin film technology described before contain one common inherent feature which is the direct type band gap structure. But in describing such material

it is come into contact with some elements like *In* and *Te* which are very much limited in the surface of the earth. The extraction of such elements also requires expensive measures. Though these novel elements put forward some best efficient solar cells ever to be achieved with thin film technology, the current trend of energy crisis cannot be met up with such rare and expensive technology. So, the pursuit of discovering earth abundant material was initiated. A unique approach to such finding is the use of quaternary semiconducting component as the absorber layer which replaces chalcopyrite content especially the *In* content with zinc (Zn) and tin (Sn).

The quaternary compound copper zinc tin sulphide and its selenized form copper zinc tin sulphide selenide are abbreviated as CZTS and CZTSSe respectively. The kesterite CZTS has a lot of similarity with chalcopyrite CIS compound both in atomic arrangement and band gap. There is also another variant of the CZTS crystal which is termed as the stannite type having a similarity with copper iron tin sulphide ( $\text{Cu}_2\text{FeSnS}_4$ ) and zinc blende. In 1988 after much research it was found that CZTS could be used as a potential material for thin film technology because of its band gap, absorption coefficient and as it is free from any rare and toxic element. The first CZTS-based solar cell was manufactured with cadmium tin oxide (CTO) layer on top of the CZTS absorber layer and the substrate used was stainless steel. The cell had a  $V_{oc}$  of 0.25 V. It was revealed here that both kesterite and stannite-based phase could coexist together [70]. Spray pyrolysis a replacement of the expensive vacuum technique was used in the manufacturing process of CZTS-based solar cell. The solution content of spray technique was copper chloride (CuCl), zinc chloride ( $\text{ZnCl}_2$ ) and tin chloride ( $\text{SnCl}_4$ ). The sulfurization was done by flowing hydrogen sulphide ( $\text{H}_2\text{S}$ ) in argon flow. This method increased the Sulphur content to 38% as compared to the earlier method which had Sulphur content of 28% [71]. The earlier solar cell designed with CZTSSe had a power conversion efficiency of 4.22% with short circuit current density and open circuit voltage as  $31.7 \text{ mAcm}^{-2}$  and 300 mV respectively having the formula  $\text{Cu}_2\text{ZnSn}(\text{S}_{0.23} \text{Se}_{0.77})_4$  [72]. It was pointed out earlier that CZTS had a polycrystalline p-type structure, this caused enough problems when it was doped with shallow donor. In order to alleviate this problem

a thin n-type semiconductor was needed between the window layer and the absorber layer. This particular layer is called the buffer layer. The buffer layer should have a wide enough band gap with type I, straddling type, band gap; a moderate spike equivalent to type II, staggered type, band gap is also permitted here. Cadmium sulphide possesses such characteristics and hence it is used as the buffer layer with CZTS absorber. The first reported CZTS solar cell had an efficiency of 0.66% with CZTS absorber layer and CdS as buffer layer having molybdenum (Mo) and zinc oxide alloyed with aluminum (ZnO/Al) as back and front contact respectively [73]. A two-step sulphurization process of CZTS absorber layer increased the efficiency to 2.62% in the first try [74]. In the next try the sulphurization process was further optimized to improve the efficiency to 5.4% [75]. Further etching (removing out extra metal) after the annealing process improved the efficiency to 6.7% [76]. The first reported CZTSe-based solar cell had an efficiency of 0.6% and later it was increased to 3.2% [77, 78]. Then intermixing of Sulphur with CZTSe the efficiency of the solar cell was improved to 9.7% and then by the same group a record efficiency of 12.6% was achieved [46, 79].

## 2.4 The Challenges of CZTSSe

Thin film technology had a major impact in the market share of solar cell from 2005 to 2009 where it reached a massive 20% share. The main reason behind this rise is attributed to the temporary shortage of silicon during this time frame. But from then on, the market of thin film technology has dropped drastically. There are some reasons behind this downfall but three reasons are prominent enough. Firstly, the polysilicon production caused a fall in the price of silicon. Secondly, a massive investment in the thin film technology led to overcapacity and thirdly, the thin film technology could not possibly keep up with the expectation it had promised since its inception as compared with silicon solar cell and thereby many of the commercial industries have move onto the research and development phase.

The most promising thin film material that dominated the market is CIGS but because of the presence of In and Ga in it which are some of the most expensive

elements as they are very rare in the earth crust the thin film technology market suffered a major setback. In this case a similar material which is CZTSSe could provide a promising result as all of the elements of this semiconducting compound is freely available. It could be used in the already established CIGS industry. Also, a radical change in the manufacturing process could be achieved with CZTSSe as it could be mass produced with non-vacuum technique and cutting down the cost drastically.

## **2.5 Theory of DC-DC Converters**

DC-DC converters play an important role in energy harvesting application for powering electrical load. The energy transducers such as photovoltaic cells, piezoelectric generators and thermogenerators have variegated output voltage ranging from too low to too high a value and as such DC-DC converters provide an effective mean to maintain a stable and optimal output voltage. The DC-DC converters are divided into two categories. The linear regulators and the switched mode regulators.

### **2.5.1 Linear Regulator**

The linear regulators produce a constant output voltage in its simplest form taking advantage of the output current and input voltage. It consists of one or more transistor as the regulating element with an added loop amplifier for giving further flexibility to the operation of the transistor. A basic linear regulator arrangement (without the loop amplifier) is shown in Figure 2.10. Here the load current is controlled by varying the base current of the transistor and thereby controlling the output voltage. It is called a linear regulator since the transistor operates in the linear region other than the saturation region or the cut off region. This provides a simpler method to supply a DC voltage to a lower voltage but it is not used in power application for its much lower efficiency.

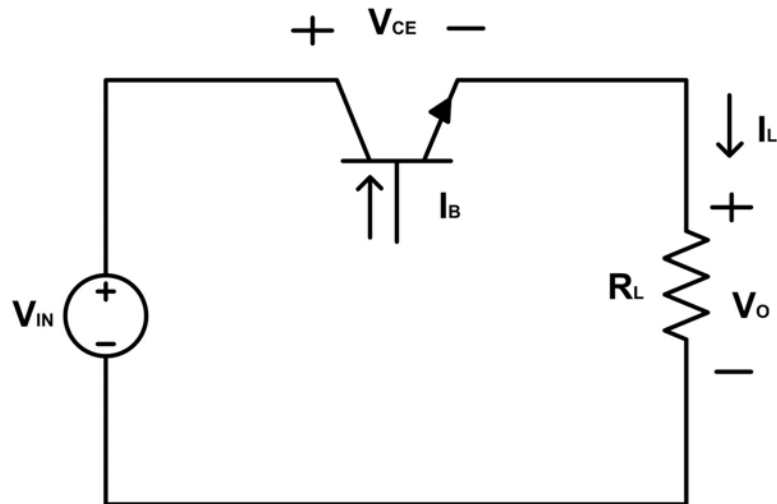


Figure 2.10: A basic linear regulator

## 2.5.2 Switched Mode Regulator

The alternative to linear regulator is the switched mode regulator where the regulating element (transistor) works like a switch which can be turned on and off by an external driver circuit. Being highly efficient such regulator has the added advantage of achieving higher voltage than the supplied voltage which is also a limitation for the linear regulator.

In the switched mode regulator, an energy storage element is used for transferring energy from input to output and as such change of the output voltage is observed. Depending on the converter topology such energy storage element may be an inductor, a capacitor and even a transformer. The current flowing through the energy storage element can change the mode of operation of such converter circuit. When the current in the energy storage element stays positive during the duty cycle (the ratio between on time and total time of operation of the transistor) continuous conduction mode is achieved and an analytical formula related to the duty cycle can be formulated. And when the current becomes zero during the duty cycle discontinuous conduction mode is achieved. In discontinuous conduction mode two duty cycle is taken into calculation for the formulation of an analytical formula. One duty cycle is for the positive current and the other is for the zero current in the energy storage element.

A buck converter delivers an output voltage lower than the input voltage. If the energy storage inductor is replaced with an equivalent transformer, the particular arrangement is termed as the forward converter. This arrangement offers the added advantage of ground isolation, particularly suitable for high power application.

A boost converter delivers an output voltage higher than the input voltage. Though in theory infinite output voltage may be achieved with a boost converter but practical realization causes the output voltage to stay at a finite value.

Buck-boost converter offers further flexibility in controlling the output voltage where both higher and lower output voltage than the input voltage can be achieved depending on the duty cycle. Here a polarity reversal is observed in the output voltage. Like buck converter this particular converter has an equivalent transformer model known as the flyback converter having similar advantage of a forward converter.

The arrangements of the converter discussed above are depicted in Figure 2.11 and the relationship between input and output voltage / current is given in Table 2.1 where continuous conduction mode is assumed and power loss is neglected.

In Ĉuk converter topology the energy storage element is the capacitor unlike the previously mentioned converter where inductor is the energy storage element. It has similar output voltage relationship like buck-boost converter with a polarity reversal. Similar to Ĉuk converter there is another arrangement known as the

Table 2.1: Voltage and current relation of common DC-DC converter [Here, D is the duty cycle, *out* and *in* subscripts represent output and input parameters respectively]

Converter Type	Voltage Relation	Current Relation
Buck Converter	$V_{out} = D * V_{in}$	$I_{out} = \frac{I_{in}}{D}$
Boost Converter	$V_{out} = \frac{V_{in}}{(1-D)}$	$I_{out} = (1 - D) * I_{in}$
Buck Boost Converter	$V_{out} = -\frac{D}{(1-D)} * V_{in}$	$I_{out} = \frac{(1-D)}{D} * I_{in}$

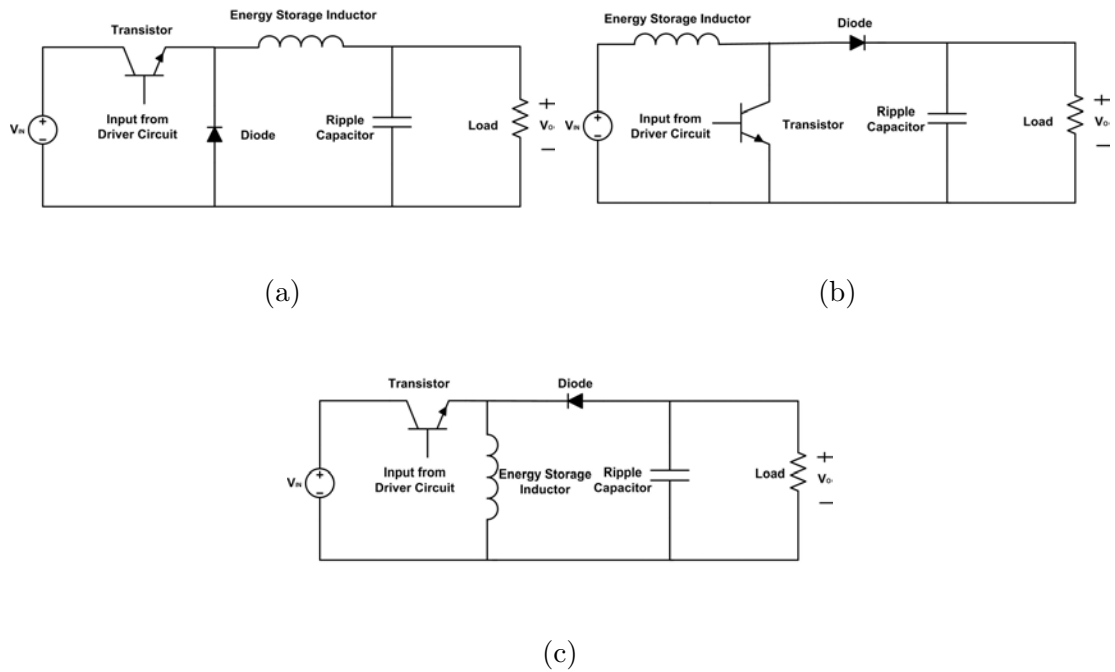


Figure 2.11: Circuit realization of (a) Buck Converter (b) Boost Converter and (c) Buck-Boost Converter

Single Ended Primary Inductance Converter (SEPIC).

The converter mentioned above are single quadrant converter which means that the current and voltage can be either positive or negative but not both in any particular arrangement. Besides these there are multi quadrant converters which are used in power transfer in transmission system and braking in motor operated machinery like an electric car.

The suitability of the converter circuit and other specialized converter circuits relevant in this study are further detailed in **Chapter 4** for better understanding.

Apart from the already established research that is going on the industry with thin film technology which are mass production of a feasible solar cell at the least cost possible, this study discusses some of the unconventional means which could be incorporated with conventional line of work to achieve even a better result. Here it is focused on to achieving a complete independence in the small power application devices and thereby making the necessity of storage devices practically obsolete. And



as such this work is based on achieving the optimal performance with the already established top of the line CZTSSe solar cell with other form of lighting source and also improving it on the way and powering a remote node with a self-driven power electronic driver.

# Chapter 3

## Performance Improvement

Chalcopyrite based CZTSSe material has gained quite importance in the field of thin film solar cell technology because of its earth abundance and toxic free matter content. Here in this chapter numerical solution technique has been used to model the current champion CZTSSe-based solar cell with its improved performance under indoor lighting condition as compared to outdoor condition and proposed an improved structure to further enhance the performance of the current CZTSSe champion cell.

CZTSSe-based semiconducting material has a direct type forbidden band gap. In this arrangement electrons residing at top of the valence band have maximum energy which mathematically can be summarized as the point having momentum where the wave number  $k$  multiplied by the Planck constant  $h$  divided by  $2\pi$ , is equal to zero. As a result, when light having photon energy,  $E_g$  is impinged on top of the p-type semiconducting material these valence electrons gets excited and reach the bottom of the conduction band from top of the valence band. This transition generates holes in the valence band and equal number of electrons (minority carrier) in the conduction band. Following the law of conservation of momentum this direct transition results smooth optical absorption with the shortest recombination lifetime. This transition is in contrast to the indirect type forbidden band gap observed in the highly used semiconducting material like silicon ( $Si$ ). In  $Si$  the transition of electrons from valence band to conduction band takes place at the point, where the conduction band minimum momentum nears,  $\pi$  divided

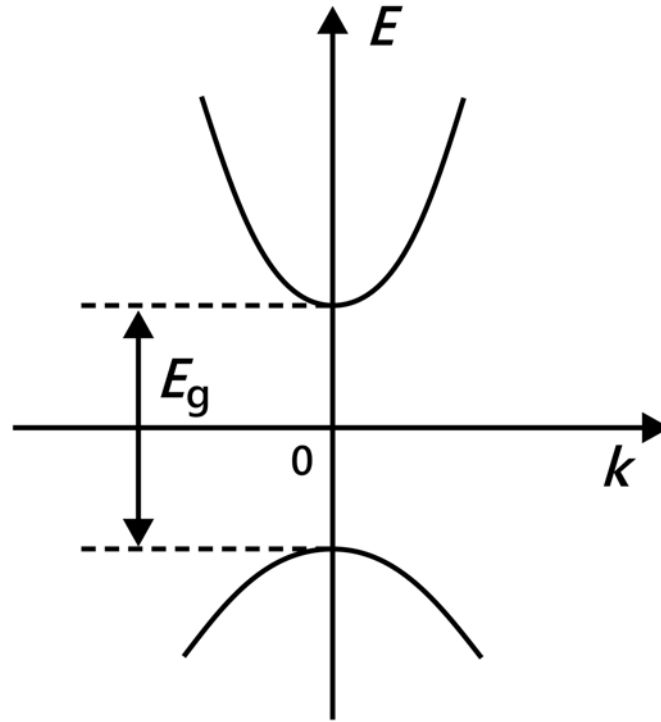


Figure 3.1:  $E$  plotted as a function of  $k$  curve for a direct band gap semiconductor

by the crystal lattice constant,  $a$  of  $Si$ . And the momentum of valence band is at the point zero. To follow the law of conservation of momentum in indirect transition, a third particle known as phonon with wavelength equating to  $2a$  is also injected. This is known as the radiative recombination which has a much longer recombination lifetime. This particular phenomenon account for both high absorption coefficient and recombination coefficient in direct type material making it suitable for pertaining in thin film solar cell. This whole process is depicted in Figure 3.1 and Figure 3.2.

## 3.1 Modeling of Champion Cell/Device A

### 3.1.1 Theoretical Modeling of Device A

The champion CZTSSe solar cell is fabricated with non-vacuum technique which uses hydrazine-based pure solution approach. In this stoichiometric approach Zn rich environment was used. The layers having the constituent elements were spin

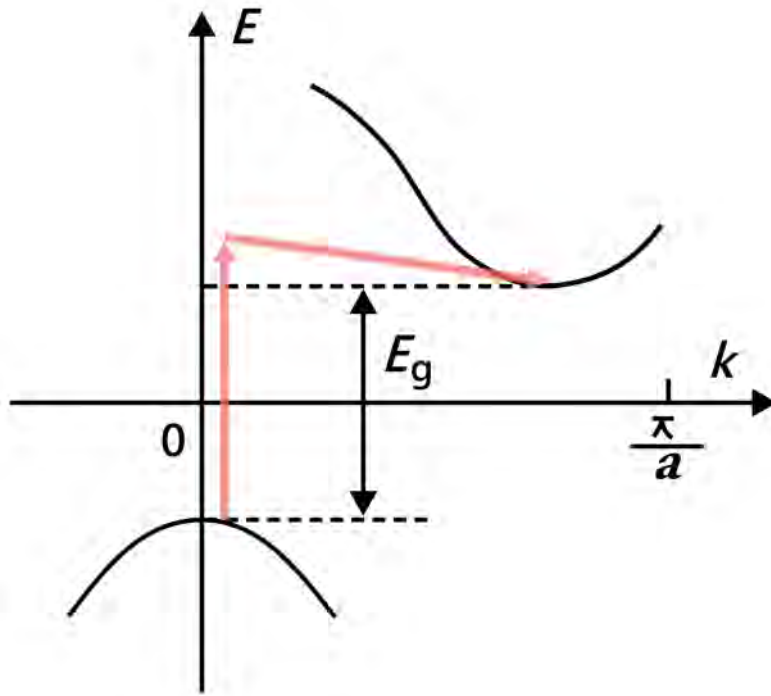


Figure 3.2: E plotted as a function of k curve for an indirect band gap semiconductor

coated in a Mo coated soda lime glass. In this deposition technique p-type CZTSSe layer (absorber layer) having a thickness of  $2\mu\text{m}$  was deposited on to the glass layer. This was later followed by a chemical bath deposition of 25nm thick n-type CdS layer (window layer). On top of it n-type zinc oxide (ZnO) (buffer layer) having 10nm thickness and indium tin oxide (ITO) (transparent conducting oxide) having thickness of 50nm were sputtered. Ni/Al metal contact was used on the top surface having a thickness of  $2\mu\text{m}$ . In this work this particular structure is regarded as device A which would be later used to represent the champion CZTSSe solar cell [46].

In this study the main focus is given on the theoretical modeling of the champion CZTSSe cell and its performance improvement. The theoretical model considered is based on numerical solution of Poisson's equation and continuity equation under optical generation-recombination conditions [80]. One-dimensional (1-D) Poisson's equation, drift-diffusion equation and continuity equations are solved in a coupled manner for each layer of the heterostructure, taking into account relevant boundary conditions at the hetero-interfaces and at the top and bottom contacts of the device.

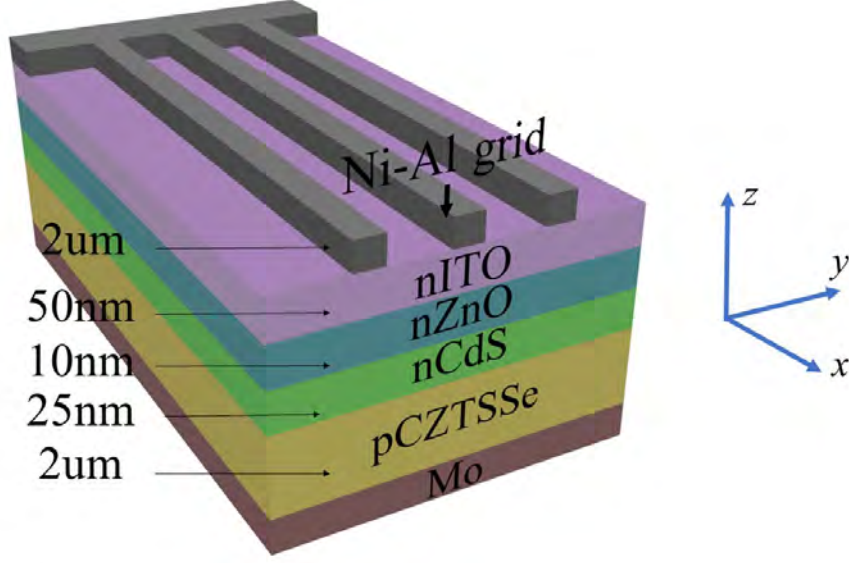


Figure 3.3: Illustration of the geometric description of device A

Considering  $z$ -axis to be the direction of light propagation and carrier transport through the device (Figure 3.3), the 1-D Poisson's equation used in this model is as follows:

$$\frac{\varepsilon_r(z)}{q} \frac{\partial^2 \varphi(z)}{\partial z^2} = p(z) - n(z) + N_D(z) - N_A(z) \quad (3.1)$$

Here  $\varepsilon_r(z)$  is the dielectric permittivity of the medium,  $q$  is the electron charge,  $N_A(z)$  and  $N_D(z)$  are the acceptor and donor concentrations, and  $n(z)$ ,  $p(z)$  are the free electron and hole densities respectively. Upon solving Poisson's equations, the following continuity equations and drift-diffusion equations are solved iteratively in a coupled manner to obtain the electron and hole current densities, which are denoted as  $J_n$  and  $J_p$  respectively.

$$J_n = q\mu_n n(z) \frac{\partial}{\partial z} E_{Fn}(z) \quad (3.2)$$

$$J_p = q\mu_p p(z) \frac{\partial}{\partial z} E_{F_p}(z) \quad (3.3)$$

$$-\frac{1}{q} \frac{\partial J_n}{\partial z} = G_n(z) - R_n(z) \quad (3.4)$$

$$+\frac{1}{q} \frac{\partial J_p}{\partial z} = G_p(z) - R_p(z) \quad (3.5)$$

Here,  $E_{F_n}$  and  $E_{F_p}$  are the electron and hole quasi-Fermi levels, which are estimated from Boltzmann approximation of the Fermi-Dirac distribution function.

### 3.1.2 Theoretical Validation of Device A in AM 1.5

In order to validate the theoretical model, experimentally measured series and shunt resistance values of  $0.72 \Omega\text{cm}^2$  and  $621 \Omega\text{cm}^2$  have been considered respectively in the numerical analysis, which consequently takes into account the effect of non-radiative recombination effects resulting from defects, interface states and high injections. The electron recombination rates  $R_n$  and hole recombination rates  $R_p$  appearing in Equations 3.4 and 3.5 respectively are calculated using the following relation considering band to band recombination under steady state condition.

$$R(z) = r^{BB} \left\{ n(z)p(z) - N_C N_V e^{-E_g(z)/kT} \right\} \quad (3.6)$$

Here  $E_g(z)$  is the material band gap,  $k$  is the Boltzmann constant,  $T$  is the operating temperature,  $N_C(z)$  and  $N_V(z)$  are effective density of states of the conduction and valence bands respectively, and  $r^{BB}$  is the band to band recombination coefficient of the corresponding layer as shown in Table 3.1 The electron generation rates and hole generation rates, denoted as  $G_n$  and  $G_p$  in

Equations 3.5 and 3.6 are calculated using the following relation:

$$G(z) = \int d\lambda \phi_0(\lambda) R(\lambda) A(\lambda) \alpha(\lambda) e^{-\alpha(\lambda)z} \quad (3.7)$$

Here  $\lambda$  is wavelength of the incident light,  $\alpha(\lambda)$  is the absorption coefficient of the material and  $\phi_0(\lambda)$  is the incident photon flux. Spectrally resolved reflectance ( $R(\lambda)$ ) and absorptance ( $A(\lambda)$ ) resulting from coherent or incoherent internal multiple reflections are calculated considering complex refractive index and total internal reflection in the semiconductor stack. The theoretical model has been validated based on the experimental results of the champion CZTSSe cell and is depicted in Figure 3.4.

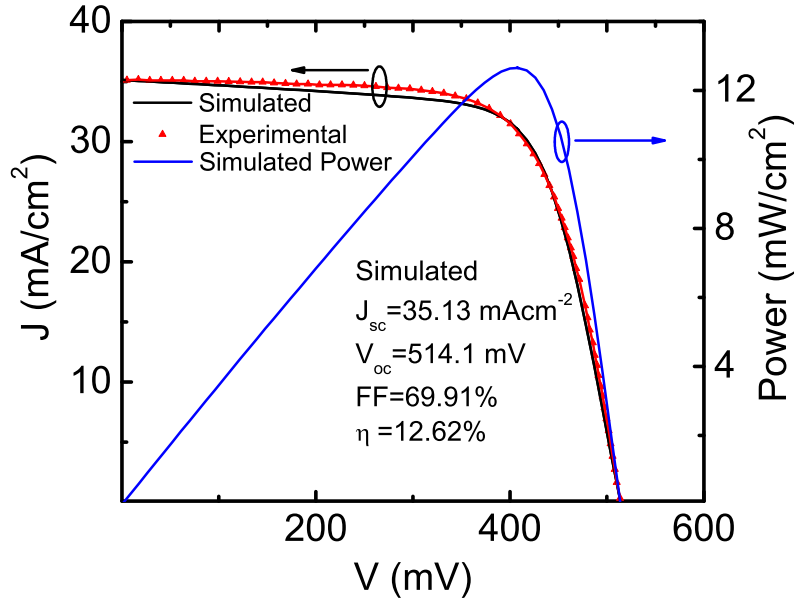


Figure 3.4: Theoretically calculated current density vs. voltage and power density vs. voltage relations along with experimentally measured values reported for the champion CZTSSe solar cell

### 3.1.3 Parameters of Device A

Different material parameters used for the analysis of Device A are listed in Table 3.1. These values have been taken from previous works reported in [46, 81–94].

Table 3.1: Values of material parameters used for Device A

Parameters	n-ITO	n-ZnO	n-CdS	p-CZTSSe
Layer Thickness (cm)	$5 \times 10^{-6}$	$1 \times 10^{-6}$	$2.5 \times 10^{-6}$	$2 \times 10^{-4}$
Mobility Gap (eV)	3.65	3.4	2.4	1.13
Optical Gap (eV)	3.65	3.4	2.4	1.13
Donor Doping ( $\text{cm}^{-3}$ )	$7 \times 10^{19}$	$1 \times 10^{16}$	$1.5 \times 10^{16}$	0
Acceptor Doping ( $\text{cm}^{-3}$ )	0	0	0	$1 \times 10^{16}$
Dielectric Constant	5.2	7.96	10	10
Electronic Affinity (eV)	4.515	4.515	4.34	4.422
Effective Density of States (DOS) in Conduction Band (CB) ( $\text{cm}^{-3}$ )	$3 \times 10^{21}$	$3.92 \times 10^{18}$	$2.22 \times 10^{18}$	$4.22 \times 10^{18}$
Effective Density of States (DOS) in Valence Band (VB) ( $\text{cm}^{-3}$ )	$2 \times 10^{21}$	$3.34 \times 10^{18}$	$1.8 \times 10^{21}$	$4.2 \times 10^{18}$
Electron Mobility ( $\text{cm}^2 \text{V}^{-1} \text{s}^{-1}$ )	75	40	340	40
Hole Mobility ( $\text{cm}^2 \text{V}^{-1} \text{s}^{-1}$ )	40	3	40	10
Auger Electron Recombination Coefficient ( $\text{cm}^6 \text{s}^{-1}$ )	0	0	$5 \times 10^{-10}$	$3.5 \times 10^{-22}$
Auger Hole Recombination Coefficient ( $\text{cm}^6 \text{s}^{-1}$ )	0	0	0	$1.5 \times 10^{-26}$
Band to Band Recombination Coefficient ( $\text{cm}^3 \text{s}^{-1}$ )	$5 \times 10^{-07}$	$5 \times 10^{-06}$	$9 \times 10^{-08}$	$1 \times 10^{-09}$
Series Resistance ( $\Omega \text{cm}^2$ )	0.72			
Shunt Resistance ( $\Omega \text{cm}^2$ )	621			



## 3.1.4 Performance Enhancement of Device A in Indoor Lighting Condition

### 3.1.4.1 Detailed Balance Theory

In **section 3.1.2**, the theoretical model of device A was calculated for outdoor lighting condition which is popularly known as the AM 1.5 . Before proceeding further with the performance of device A under other lighting condition the theoretical background of the Shockley-Queisser limit is needed. The Shockley-Queisser limit for other lighting condition can best be understood with the help of detailed balance theory. In fact, Shockley and Queisser were the first people to use the detailed balance theory for p-n junction in 1961 [45]. Detailed balance theory has its foundation in the law of conservation of energy. Two types of phenomena go on in a photovoltaic device they are photo absorption and photon emission. In dark condition the law of conservation of energy dictates that in steady state the carrier charge concentration must remain constant and as such the rate of photon absorption should equal to the rate of photon emission. As a result, the current density ( $J_{abs}(E)$ ) absorbed by the photovoltaic cell can be obtained from the following:

$$J_{abs}(E) = q(1 - R(E)) a(E)b_a(E) \quad (3.8)$$

Here,  $a(E)$  and  $R(E)$  are the probability of photon absorption and the probability of photon reflection respectively with photon having energy,  $E$ . Whereas,  $b_a(E)$  is the spectral photon flux of the ambient condition which follows the same equation as the spectral flux of a black body taken at a temperature of 5760K as mentioned in **Chapter 2**.

Similarly, the current density ( $J_{rad}(E)$ ) emitted from the photovoltaic cell can be calculated as follows:

$$J_{rad}(E) = q(1 - R(E)) \varepsilon(E)b_a(E) \quad (3.9)$$

Here,  $\varepsilon(E)$  is the probability of emitting a photon having energy,  $E$ . For simplicity it is assumed that the photovoltaic cell has the same temperature as

the ambient condition and as a result the spectral photon flux from the photovoltaic device could be taken as  $b_a(E)$ . In steady state  $J_{abs}(E)$  and  $J_{rad}(E)$  is taken as equal which leads to the following condition:

$$a(E) = \varepsilon(E) \quad (3.10)$$

This is summarized as the probability of absorption which is equivalent to the emission of photon having energy,  $E$ . In illuminated condition the photovoltaic cell absorbs photon from both the light source and the ambient which further modifies the current density ( $J_{abs}(E)$ ) absorbed by the photovoltaic cell as follows:

$$J_{abs}(E) = q(1 - R(E)) a(E) \left( b_s(E) + \left(1 - \frac{F_s}{F_e}\right) b_a(E) \right) \quad (3.11)$$

Here, the coefficient  $(1 - F_s/F_e)$  is the fraction of the spectral flux that could not be replaced by the incident flux from the light source. In general, the spectral flux, also known as the luminous flux is symbolized as  $F$  and the subscripts  $s$  and  $e$  are for source and ambient respectively and this is obtained from the following equation:

$$F = 683 \frac{lm}{watt} \int_0^{\infty} V(\lambda) L(\lambda) d\lambda \quad (3.12)$$

Here, the coefficient  $683lm/watt$  is the sensitivity of human eye at 555nm wavelength of the lighting source,  $V(\lambda)$  is the luminosity function which could be generalized as the spectral response of human eye or in a more simplistic manner as the perception of human eye to the brightness of different light at

different frequencies and  $L(\lambda)$  is the irradiance of the light source varying with the wavelength,  $\lambda$ .

In a similar manner, the current density ( $J_{rad}(E)$ ) of Equation 3.9 emitted by the photovoltaic cell also gets modified as follows:

$$J_{rad}(E) = q(1 - R(E))\varepsilon(E)b_e(E, \Delta\mu) \quad (3.13)$$

Here,  $\Delta\mu$  is the electrochemical potential energy of the photovoltaic cell. Thus, the total current density ( $J_{tot}(E)$ ) is given as follows:

$$J_{tot}(E) = J_{abs}(E) - J_{rad}(E) = q(1 - R(E))a(E) \left( b_s(E) + \left( 1 - \frac{F_s}{F_e} \right) b_a(E) - b_e(E, \Delta\mu) \right) \quad (3.14)$$

The total current density ( $J_{tot}(E)$ ) could be further split up into photocurrent density ( $\Delta J_{sc}(E)$ ) and radiative recombination current density ( $\Delta J_{rec}(E)$ ) as given in Equation 3.15 and 3.16 .

$$\Delta J_{sc}(E) = q(1 - R(E))a(E) \left( b_s(E) - \frac{F_s}{F_e} b_a(E) \right) \quad (3.15)$$

$$\Delta J_{rec}(E) = q(1 - R(E))a(E) (b_a(E) - b_e(E, \Delta\mu)) \quad (3.16)$$

Integrating the Equation 3.11 over the entire range of energy gives the total photocurrent density,  $J_{sc}$  which is given in **Chapter 2** Equation 2.1 .

It is important to notice that the spectral flux density is quite different for different spectral content and intensity of the spectrum. The photocurrent density  $J_{sc}(E)$  is quite pivotal in the design of a photovoltaic cell as this defines the maximum limit of the photocurrent available for that particular photovoltaic cell and the quantum efficiency  $QE(E)$  determines the maximum photocurrent available to the external circuit.

### 3.1.4.2 Generalized Shockley-Queisser Limit

From the knowledge of the detailed balance theory the Shockley-Queisser efficiency limit can be reached as a function of band gap for different lighting condition. But in order to plot this efficiency for different lighting condition other than the AM 1.5 further simplification of the dark current density ( $J_{dark}$ ), open circuit voltage equation ( $V_{oc}$ ) and ( $FF$ ) is required [95].

$$J_{dark} = q \frac{2\pi kT}{h^3 c^2} (E_g + kT)^2 e^{-\frac{E_g}{kT}} \quad (3.17)$$

Here,  $k$  is the Boltzmann's constant,  $E_g$  is the band gap,  $h$  is the plank's constant,  $c$  is the velocity of light and for simplicity the value of absolute temperature  $T$  is taken to be 300K. From the knowledge of the photocurrent density and the dark current density, the open circuit voltage  $V_{oc}$  can be calculated and also for achieving simplicity of  $FF$  the normalized form of the open circuit voltage  $v_{oc}$  is taken as follows:

$$V_{oc} = \frac{kT}{q} \ln \left( \frac{J_{sc}}{J_{dark}} + 1 \right) \quad (3.18)$$

$$v_{oc} = \frac{V_{oc}}{kT/q} \quad (3.19)$$

The simplistic form of the  $FF$  is calculated from the following:

$$FF = (v_{oc} - \ln(v_{oc} + 0.72))/(v_{oc} + 1) \quad (3.20)$$

Now if the input radiation has the power ( $P_{in}$ ) the generalized Shockley-Queisser limit efficiency can be found from the following:

$$\eta = \frac{V_{oc}J_{sc}FF}{P_{in}} \quad (3.21)$$

### 3.1.4.3 Performance Enhancement with White LED

The indoor light source considered in this study is a commercially available 15W, 497 lumen white LED, which is measured to have a color rendering index of 75.74% and correlated color temperature of 6175K. Its emission spectrum was measured using an integrating sphere. It has a peak appearing around wavelength of  $\lambda=450\text{nm}$  of the LED spectrum which is the characteristic of the commercially available white LEDs employing blue emitting diodes to generate secondary emission at longer wavelengths.

The Shockley-Queisser efficiency as a function of band gap for both indoor lighting (white LED) and outdoor lighting (AM 1.5) condition is shown in Figure 3.5 . From this figure the theoretical maximum efficiency limit for outdoor lighting condition is found to be at 33.7% and for indoor lighting condition it is 59.102%. This high efficiency limit proved to be quite insightful to continue the study with CZTSSe

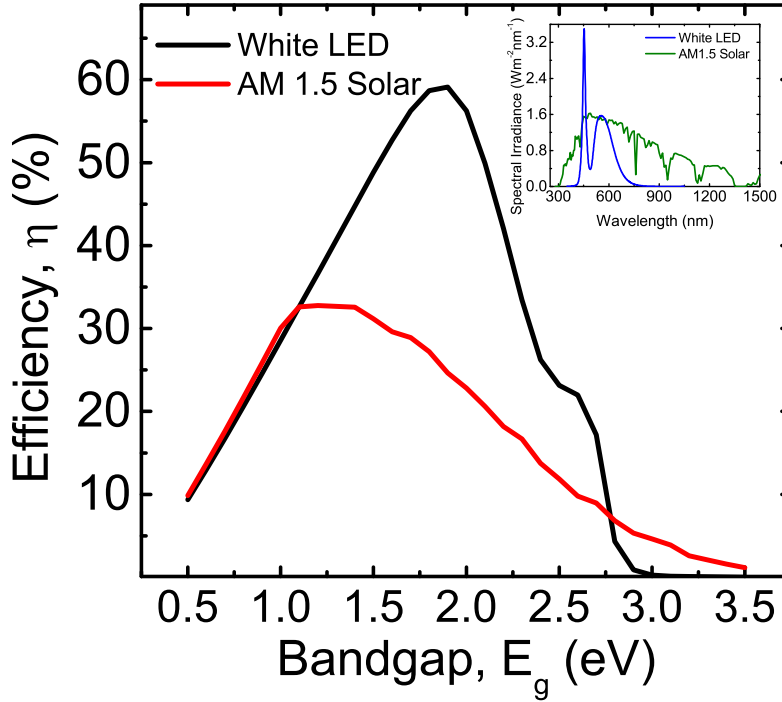


Figure 3.5: Shockley-Queisser efficiency as a function of band gap for both indoor [white LED] and outdoor [AM 1.5 solar] lighting condition. [Inset: Spectral irradiance for indoor and outdoor lighting condition varying with wavelength]

material. So further data extraction from this particular figure the theoretical efficiency limit is also found to be higher for a single junction thin-film CZTSSe cell having a band gap of 1.13eV, the efficiency limit for outdoor lighting condition is 32.6% and for indoor lighting condition it is 40.6%. So far, the highest reported efficiency is 12.6% for CZTSSe photovoltaic cell with the champion cell that is modeled in device A. With the same device structure and its intrinsic defects like the parasitic resistance, band to band recombination and Auger recombination the performance of device A under outdoor lighting condition is predicted.

In this section the performance of device A under indoor lighting condition is studied with detailed analysis. In order to compare the performance of device A under indoor lighting with respect to outdoor lighting the indoor illumination is taken to be  $300\text{Wm}^{-2}$ . In this illumination the efficiency and the  $FF$  of device A are obtained to be 13.77% and 71.05% respectively, which are both higher than the experimental results obtained under outdoor condition as shown in Figure 3.6. The reason behind the selection of this particular illumination is that at very low illumination the parasitic resistance and defects contributes a lot towards the dark current and though at very low illumination device A also has better efficiency

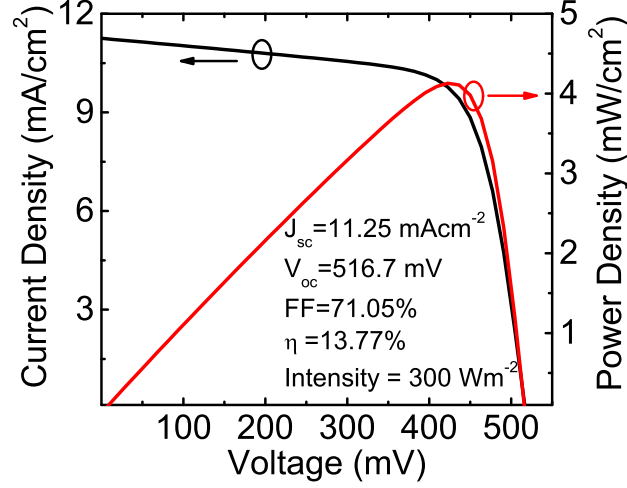


Figure 3.6: Current and power densities as a function of voltage in Device A

under indoor lighting, this illumination is high enough to overcome those parasitic effect and proved to have a pragmatic superior performance.

To ascertain that the increased efficiency is intrinsically related to the nature of the indoor spectrum rather than to the intensity level of the illuminating light source, the efficiency and  $FF$  of the device are calculated under varying intensities of solar and indoor radiation. As shown in Figure 3.7 , the efficiency of the device is higher under indoor condition at all intensity levels of the light source. Thus, proving the performance of the device is quite independent of the illumination of the spectra selected.

To explain the observed behavior, the variation of open-circuit voltage ( $V_{oc}$ ) and short circuit current density ( $J_{sc}$ ) of Device A is shown as a function of irradiance in Figure 3.8. It is obvious that at higher intensities of both solar and indoor radiation, the efficiency tends to saturate because of the saturation of the open-circuit voltage and  $FF$ . This is related to the following dependence of  $V_{oc}$  and  $J_{sc}$  on radiation intensity ( $I_0$ ):

$$V_{oc} = \frac{kT}{q} \ln \left( \frac{\eta_i I_0 q}{h\nu J_0} \right) \quad (3.22)$$

$$J_{sc} = \frac{\eta_i I_0 A q}{h\nu} \quad (3.23)$$

Here,  $A$  is the area of the cell,  $T$  is the cell temperature,  $\nu$  is the frequency of the illuminating light,  $J_o$  is reverse saturation current and  $\eta_i$  is the fraction of absorbed incident radiation.

Thus, the logarithmic dependence of open-circuit voltage on irradiance results in the saturation of  $V_{oc}$  at high intensities (around  $300\text{Wm}^{-2}$ ), whereas  $J_{sc}$  increases linearly because of its direct proportionality with  $I_0$ .

It is further shown in Figure 3.7 and Figure 3.8 that at high levels of intensity, efficiency enhancement under indoor illumination mainly arises from the marginal increase of  $FF$  and open circuit voltage  $V_{oc}$ , and the significant increase of short circuit current density,  $J_{sc}$ .

In order to further impose the dominance of indoor lighting condition over outdoor lighting condition the illustration of the percentage increase of  $FF$ ,  $J_{sc}$ ,  $V_{oc}$  and overall efficiency under indoor spectrum with respect to the values obtained under outdoor solar radiation is shown in Figure 3.9.

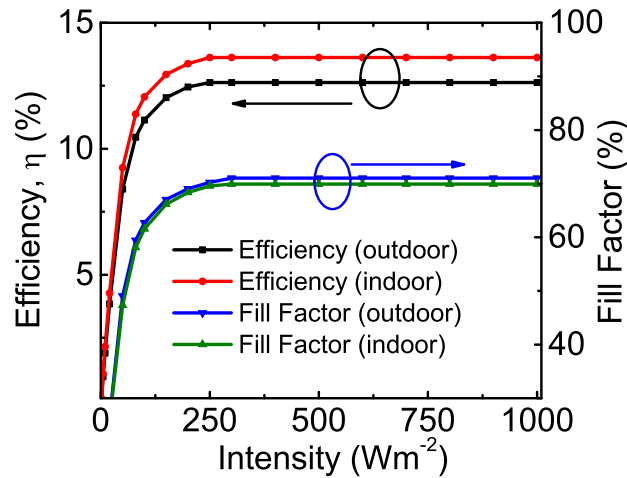


Figure 3.7: Efficiency and  $FF$  as a function intensity under both indoor and solar illumination conditions in Device A



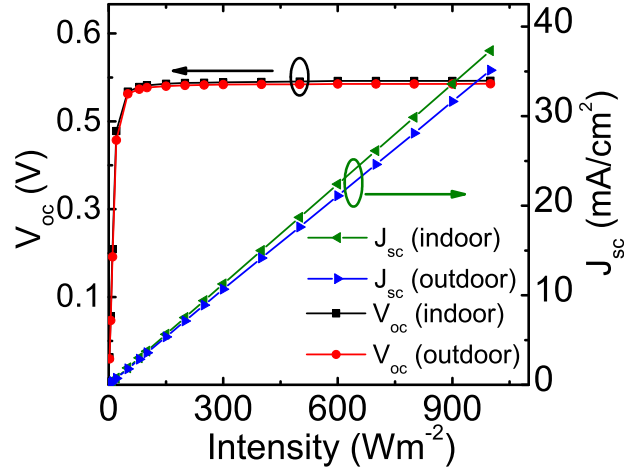


Figure 3.8: Open circuit voltage ( $V_{oc}$ ) and short circuit current density ( $J_{sc}$ ) as a function intensity under both indoor and solar illumination conditions in Device A

A unique finding of the relative enhancement of device A under indoor spectrum with respect to outdoor spectrum is that at radiation intensities above  $150\text{Wm}^{-2}$ , the relative enhancement of short circuit current density is about twice of the values obtained for  $\Delta V_{oc}$  and  $\Delta FF$ . However, for lower intensities, the efficiency enhancement is dominated by the relative increase of the open circuit voltage. The maximum enhancement of overall efficiency under this condition is 14%. Such performance enhancements support the suitability of this device for operation under low-intensity indoor lighting conditions.

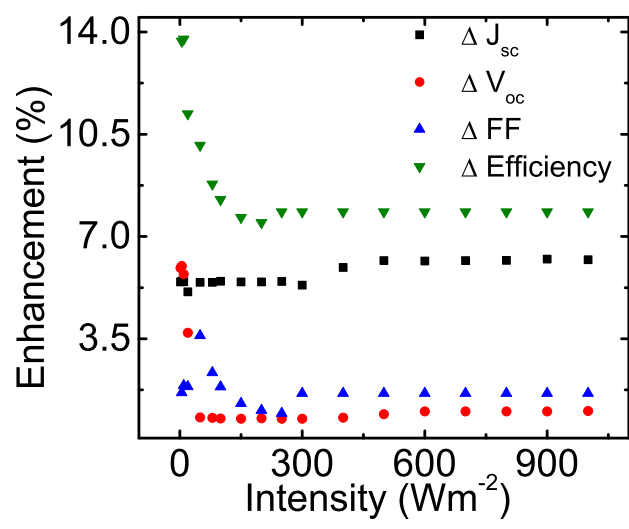


Figure 3.9: Relative enhancement of  $J_{sc}$ ,  $V_{oc}$ ,  $FF$  and efficiency with respect to outdoor solar illumination conditions for varying intensities of the illuminating source

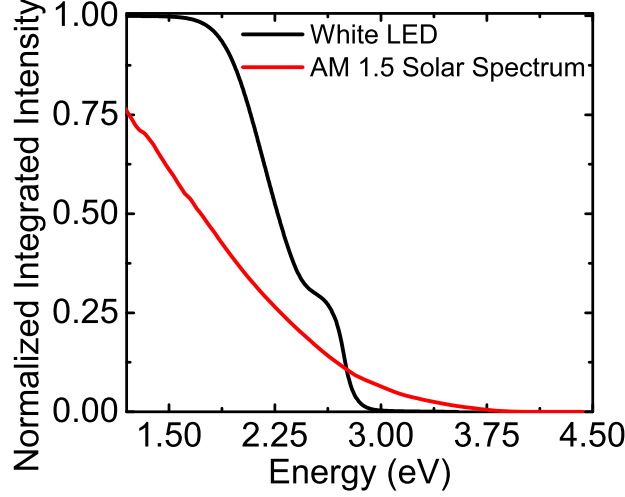


Figure 3.10: Normalized integrated intensity (photon yield) as a function of photon energy for white LED and solar spectra

The underlying reason behind the enhancement of the short circuit current density and open circuit voltage under indoor condition is photon yield of both white LED and solar spectrum which are calculated and plotted in Figure 3.10. The indoor lighting sources are commercially developed so as to emit photons in the visible range from 380nm to 780nm and all has a peak sensitivity at 555nm [95]. This phenomenon is also analogous to having significantly higher photon yield of the commercially available indoor lighting sources with respect to outdoor lighting condition (AM 1.5 solar radiation) when paired with photovoltaic converters having a band gap in the range of 1eV to 1.5eV. The white LED used in the experimental setup is not an exception to this particular phenomenon. For the considered white LED spectrum, a photon yield of  $\sim 100\%$  over the bandgap range of CZTSSe was obtained, whereas for solar irradiation this value ranges from 60-75%. Because of these high photon yields, enhancement of both  $J_{sc}$  and  $V_{oc}$  are obtained at all intensities of the indoor spectrum in comparison with the outdoor condition.

In spite of the high photon yield for white LED which is approximately 25% more when compared to AM 1.5 solar radiation an efficiency improvement of only 13.77% is achieved for device A. This marginal efficiency enhancement can be explained by the device A's external quantum efficiency ( $EQE$ ) profile shown in Figure 3.11. For both indoor and outdoor conditions, the  $EQE$  peaks at  $\sim 2.5\text{eV}$  and since the photon yields for solar and indoor radiations are rather comparable

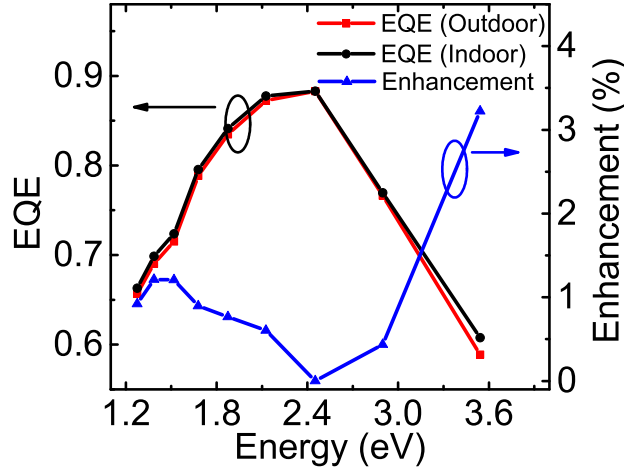


Figure 3.11: External quantum efficiency (EQE) profiles for indoor and solar illumination condition in Device A along with the relative enhancement of EQE

at this energy, the overall efficiency enhancement is relatively low.

In order to further verify the hypothesis concerning photon yield, the spectral response of the device under both AM1.5 and white LED spectra are calculated and plotted in Figure 3.12. From the figure it is known that the enhancement of spectral response ranges from 0.28% to 7.8% depending on the incident photon energy. The spectral response obtained under indoor condition increases significantly for photon energies above 3.5eV, which is indicative of the better performance characteristics of this device in the short wavelength region. This is further supported by the carrier generation profiles in different regions of the device A obtained and plotted in Figure 3.13 by the equations of generation rate as discussed previously.

From the Figure 3.13 it is obtained that the generation rate in the vicinity of the p-n junction is higher for the case of indoor illumination. As photo-generation near the junction is dominated by absorption of short-wavelength component of the spectrum, it is likely that the high photon yields at short wavelengths of the LED spectrum results in higher generation rates in the CZTSSe device compared to the rates obtained under solar radiation.

The results discussed so far indicate that enhancement of efficiency and  $FF$  of

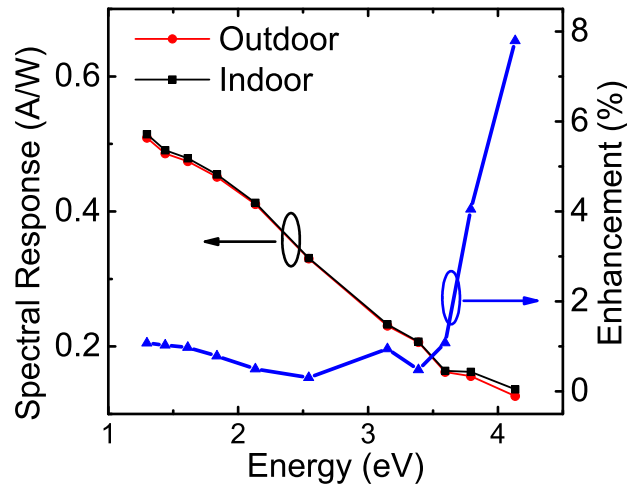


Figure 3.12: Spectral response for indoor and solar illumination along with the relative increase of spectral response for indoor illumination with respect to solar illumination condition

a CZTSSe photovoltaic device under indoor condition is related to the high photon yield of the illuminating indoor spectrum, which results in higher generation rates, spectral response and subsequently higher  $V_{oc}$  and  $J_{sc}$  at low and high intensities respectively.

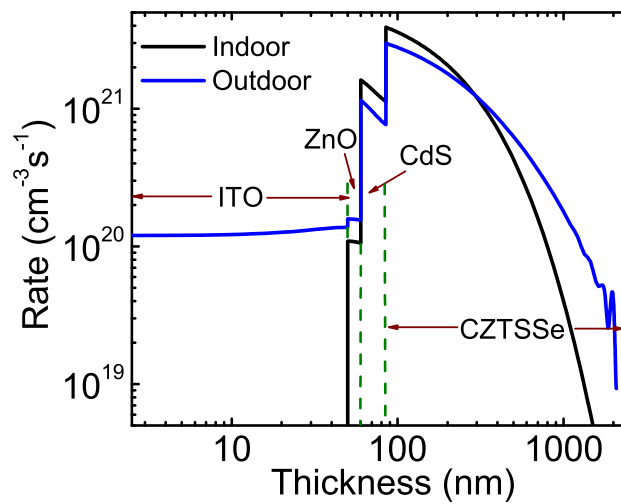


Figure 3.13: Generation rates in different regions of Device A

## 3.2 Modeling of Improved Cell/Device B

### 3.2.1 Type I and Type II Band Type Structure

The intrinsic characteristic of a photovoltaic device is to contain a metallurgically intimate junction between a p-type semiconductor and an n-type semiconductor. As discussed previously a p-type absorber is suitable for forming an efficient photovoltaic cell, CZTSSe offers quite the promising feature of being an inherently doped p-type semiconductor. So, in the formation of a pn-heterojunction for photovoltaic cell a different n-type semiconductor having characteristic feature of wide band gap is utilized with the p-type absorber. A suitable semiconducting material which is popularly utilized as the wide band gap acting as a buffer with n-type conductivity is cadmium sulphide (CdS).

Depending on the selection of buffer layer with the subsequent window and transparent conducting oxide layer there may arise the type I (straddling) and type II (staggered) band gap as shown in Figure 3.14 and 3.15 respectively.

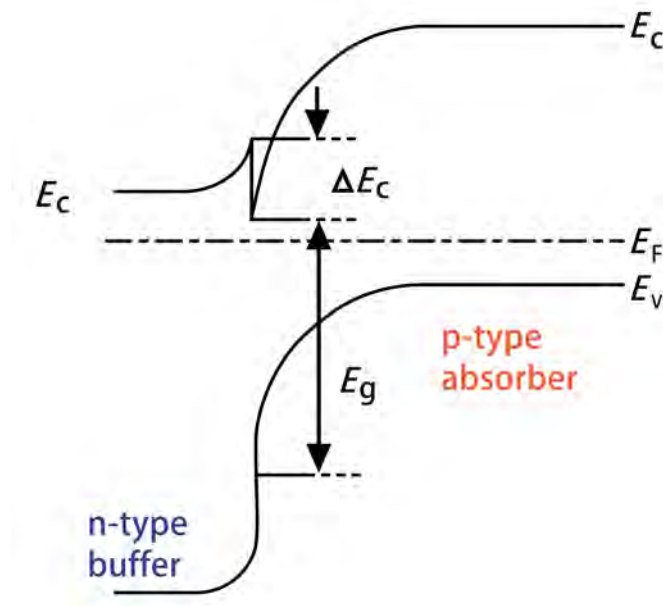


Figure 3.14: Generalized energy band diagram of type I (straddling) pn-heterojunction photovoltaic cell

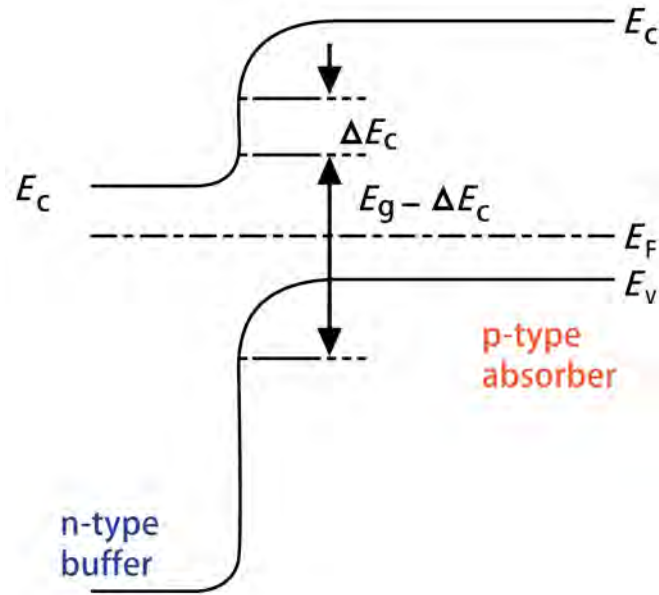


Figure 3.15: Generalized energy band diagram of type II (staggered) pn-heterojunction photovoltaic cell

The experimental model that is labelled as device A uses the type I band gap and as such it has a low open circuit voltage ( $V_{oc}$ ). In the previous section indoor lighting has been employed to enhance the efficiency of this particular device but in spite of having all the characteristic feature of a highly efficient photovoltaic cell under indoor lighting, the efficiency enhancement was very much limited. One particular trait that is discovered behind this low efficiency enhancement is the marginal increase of open circuit voltage under indoor lighting as compared to outdoor lighting. So, in this section a modified structure which is labelled as device B is utilized for further efficiency enhancement under indoor lighting condition . This is labelled and depicted in Figure 3.16 [96]. Where light impinges on the device on z-axis.

In this structure, the n-doped ZnO and n-ITO layers of device A are replaced with intrinsic ZnO and n-doped ZnO respectively, keeping the materials of other layers unchanged. The proposed device can be experimentally fabricated employing low-cost, nonvacuum deposition techniques reported previously for the fabrication of CZTSSe-based PV devices [97].

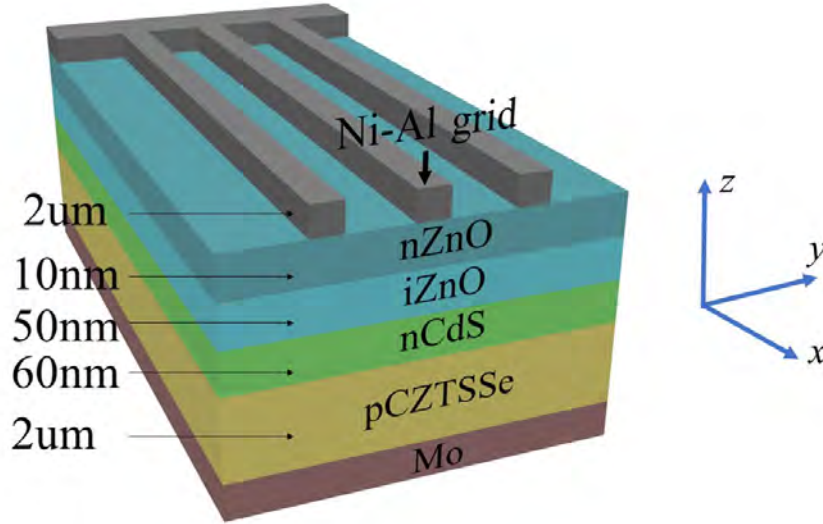


Figure 3.16: Schematic diagram of proposed device B

Another unique feature of this particular device lies in the selection of ZnO since Al doped ZnO is considered as an effective replacement of ITO as a transparent conductive oxide because of its equivalent performance characteristics at relatively low cost [98].

In Figure 3.17 the JV characteristic of device B is plotted for indoor and outdoor lighting condition and the comparison is done at an illuminating radiation of  $300\text{Wm}^{-2}$  as used previously. This shows that the value of efficiency is 13.77% under outdoor lighting as compared to device A which has an efficiency of 12.6%. Also, the efficiency under indoor condition for device B is 15.3% as compared to device A's 13.77%.

### 3.2.2 Performance Enhancement

A comparison of energy band diagram in the equilibrium condition between device A and device B as depicted in Figure 3.18 reveals that device A has a straddling (type I) heterostructure and device B is staggered (type II) in nature because of the conduction band offsets between ZnO and CZTSSe [99]. It is known that energy spike appearing in the conduction band of straddling gap heterostructure can possibly increase the open circuit voltage of the device [100]. This comparison also

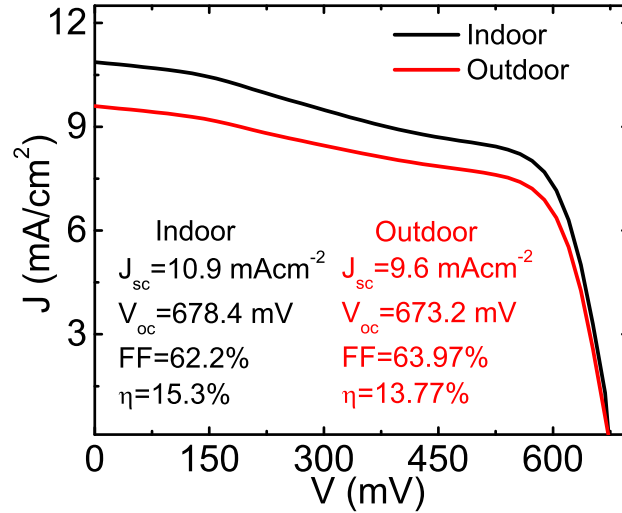


Figure 3.17: J-V characteristics of Device B for both indoor and solar illumination conditions

reveals that the intrinsic ZnO layer in device B results in a built-in field of  $6.6 \times 10^8 \text{ Vcm}^{-1}$ , which is approximately 11% higher than the value obtained for device A. This higher built in field effectively enhances separation of photo-generated carriers near the junction, thereby enhancing the open-circuit voltage of the device.

In an attempt to further illustrate this effect, the energy band diagrams of both devices are shown in Figure 3.19 under a non-equilibrium condition of indoor

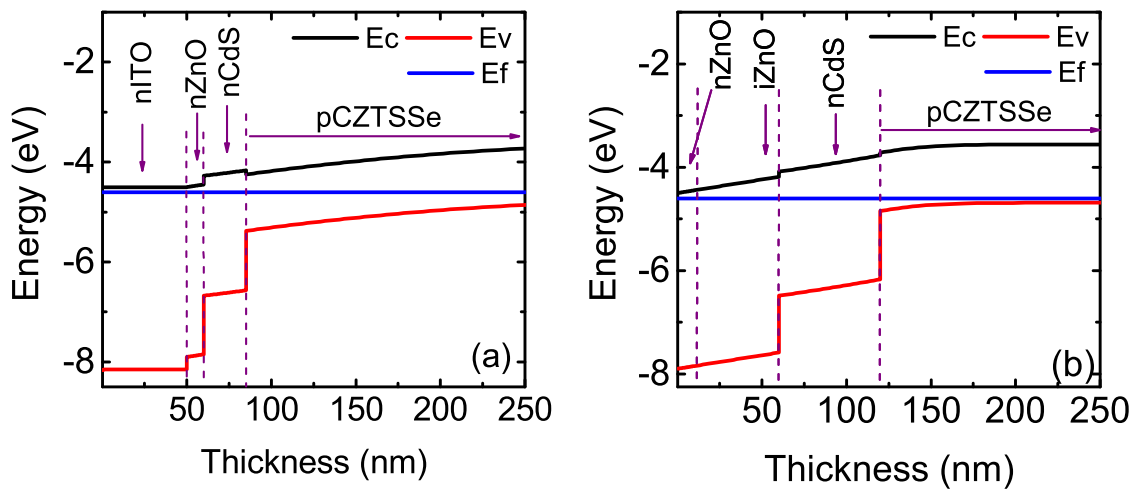


Figure 3.18: (a) Energy band diagram of device A and (b) Energy band diagram of device B at equilibrium condition



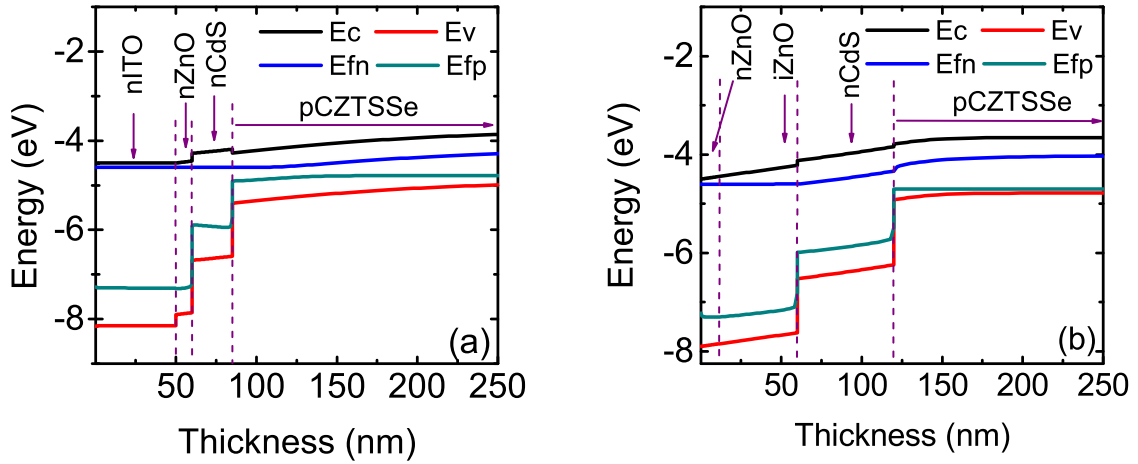


Figure 3.19: (a) Energy band diagram of device A and (b) Energy band diagram of device B under indoor illumination condition

illumination. As can be observed, the maximum energy difference ( $\Delta E_f$ ) of the quasi Fermi levels in device B is 0.68eV whereas for device A the value is 0.52 eV. Hence it is expected that under identical operating conditions, the proposed PV device should exhibit a higher open circuit voltage under indoor illumination.

In order to compare the output performance characteristics, the calculated short-circuit current density and open-circuit voltages of both device A and B under indoor illumination of varying intensities are plotted in Figure 3.20 . At an illumination of  $1000\text{Wm}^{-2}$ , the built-in voltage of device B is observed to be 0.17V higher than that of device A, and this value decreases to 0.14V at a low intensity of  $50\text{Wm}^{-2}$ . In spite of the higher  $V_{oc}$ , the short-circuit current density in Device B remains lower than that of Device A at all intensity levels. This is related to the incorporation of the n-ZnO layer, which has higher absorption characteristics than that of ITO within 400-800nm range of the electromagnetic spectrum [101].

In spite of the lowering of the short circuit current density, the enhanced open circuit voltage results in an overall increase of the efficiency of the device under white LED illumination. This is shown in Figure 3.21, where the calculated

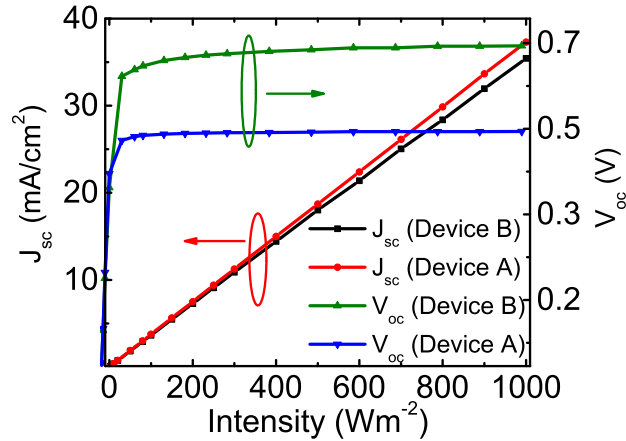


Figure 3.20:  $J_{sc}$  and  $V_{oc}$  of device A and device B for different intensities of the illuminating white LED source.

efficiencies of both of device A and B are plotted as a function of radiation intensity. It is noteworthy that in spite of the increased efficiency, the  $FF$  of device B remains lower than that of device A. This lowering of  $FF$  is related to the increase of defects in device B, which results from the relatively lower electron and hole mobilities of the introduced i-ZnO layer compared to those of the ITO layer used in device A [90].

Therefore, for indoor applications, an optimization needs to be reached in the design of PV devices such that the efficiency can be increased by significantly enhancing the  $V_{oc}$ , and at the same time the shunt and series resistances can be kept low enough so that a high value of  $J_{sc}$  and  $FF$  can be maintained.

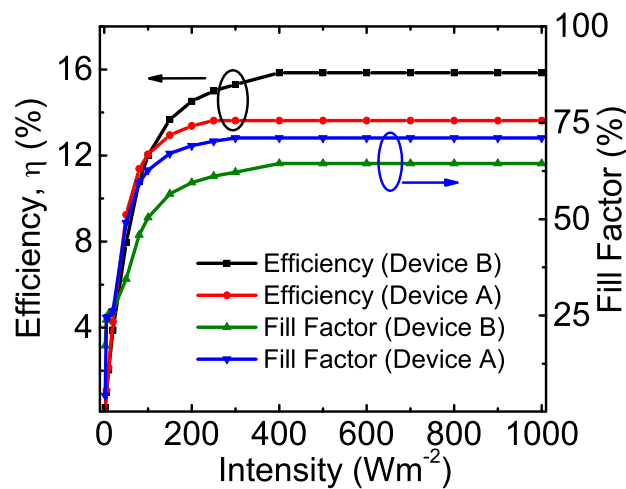


Figure 3.21: Efficiency and  $FF$  of device A and device B plotted as a function of the intensity of illuminating white LED

### 3.2.3 Parameters of Device B

Material parameters used for the analysis of Device B are listed in Table 3.2. These values have been taken from previous works reported in [46, 81–94].

Table 3.2: Values of material parameters used for Device B

Parameters	n-ITO	i-ZnO	n-CdS	p-CZTSSe
Layer Thickness (cm)	$1 \times 10^{-6}$	$5 \times 10^{-6}$	$6 \times 10^{-6}$	$2 \times 10^{-4}$
Mobility Gap (eV)	3.4	3.4	2.4	1.13
Optical Gap (eV)	3.4	3.4	2.4	1.13
Donor Doping ( $\text{cm}^{-3}$ )	$2.2 \times 10^{19}$	0	$1.1 \times 10^{16}$	0
Acceptor Doping ( $\text{cm}^{-3}$ )	0	0	0	$7 \times 10^{16}$
Dielectric Constant	7.96	7.96	10	10
Electronic Affinity (eV)	4.5	4.5	4.34	4.422
Effective Density of States (DOS) in Conduction Band (CB) ( $\text{cm}^{-3}$ )	$3.92 \times 10^{18}$	$3.92 \times 10^{18}$	$2.22 \times 10^{18}$	$4.22 \times 10^{18}$
Effective Density of States (DOS) in Valence Band (VB) ( $\text{cm}^{-3}$ )	$3.34 \times 10^{18}$	$3.34 \times 10^{18}$	$1.8 \times 10^{18}$	$4.2 \times 10^{18}$
Electron Mobility ( $\text{cm}^2 \text{V}^{-1} \text{s}^{-1}$ )	40	40	340	40
Hole Mobility ( $\text{cm}^2 \text{V}^{-1} \text{s}^{-1}$ )	3	3	40	10
Auger Electron Recombination Coefficient ( $\text{cm}^6 \text{s}^{-1}$ )	0	0	$5 \times 10^{-10}$	$3.5 \times 10^{-22}$
Auger Hole Recombination Coefficient ( $\text{cm}^6 \text{s}^{-1}$ )	0	0	0	$1.5 \times 10^{-26}$
Band to Band Recombination Coefficient ( $\text{cm}^3 \text{s}^{-1}$ )	$5 \times 10^{-07}$	$5 \times 10^{-06}$	$9 \times 10^{-08}$	$1 \times 10^{-09}$
Series Resistance ( $\Omega \text{cm}^2$ )	0.72			
Shunt Resistance ( $\Omega \text{cm}^2$ )	621			

In summary performance characteristics of CZTSSe photovoltaic device with respect to indoor energy harvesting applications is investigated using numerical analysis. The heterostructure of the highest efficiency CZTSSe solar cell is first considered for performance evaluation under an experimentally measured, commercial white LED spectrum. The efficiency of the device is obtained to be higher under indoor condition because of the enhanced open circuit voltage and short circuit current. Enhancement of the open circuit voltage is more pronounced under low intensities, whereas under high intensity the enhancement of short-circuit current dominates. These enhancements are attributed to the higher photon yield of the white LED corresponding to the bandgap of CZTSSe, which results in higher generation rate and spectral response under indoor condition. Further performance enhancement is obtained by designing a type-II heterostructure, in which better charge separation caused by the intrinsic ZnO layer further improves the open circuit voltage. The study shows that in spite of the high photon yield, efficiency enhancement in a CZTSSe device is limited by its external quantum efficiency profile, the peak of which does not coincide with the high photon yield regime corresponding to the indoor spectrum. So a detailed analysis could be done with the design of spectra that have photon yield coinciding with peak of the external quantum efficiency of the device.

# Chapter 4

## Converter Circuit for Energy

### Harvesting with CZTSSe-based

### Solar Cell

The modern era has seen a lot of advancement in the field of electronics where the size of electronic devices is diminishing with the passage of time. This particular advancement has made possible for the electronic devices to be interconnected coming from variegated sources forming a network which is most popularly known as IoT or the Internet of Things. This means that the devices will consume less power and as a result data coming with the help of such devices will form a centralized automated system. The data may include all sorts of information from sensors located at a particular point which could be termed as sensor nodes. The sensor could provide data ranging from heating, cooling, ventilation, security, image processing and so on. The data could be processed and transmitted through wireless communication system and thus forming a truly automated system. And this mode of communication has urged the need to provide power supplies for the sensor nodes. One particular mean could be wired connection but this would ruin the purpose of going wireless with total automation. Another mode that is widely popular is the use of battery which has been the pragmatic solution of this problem and has been going on for quite some time now. But this particular solution has two problems which needs to be addressed. Firstly, the battery needs to be replaced as all battery no matter how good the technology is needs to be replaced. Secondly,

all types of battery have emission which is harmful for the environment. Again this pragmatic solution does not quite achieve the goal of going entirely automated.

In order to bypass the problem, renewable sources could be used and a lot of research has been going on in this field. The energy harvesting or energy scavenging is a term quite popular in this respect and photovoltaic cell has gained much prominence because of its higher efficiency and reliability compared to other renewable sources as the likes of piezoelectric vibrator and energy from thermal sources. In this particular aspect two photovoltaic cells based on CZTSSe have been proposed which have open circuit voltages ranging from 500mV to 690mv, short circuit current density from  $30\text{mAcm}^{-2}$  to  $35\text{mAcm}^{-2}$  and having a range of efficiency from 12% to 15% based on the spectrum used; which could be both outdoor solar radiation and indoor lighting from LED sources as discussed in **Chapter 3**. Though the output performance achieved through these cells have been quite admirable as compared to the current state of the art CZTSSe based photovoltaic cell, these are not suitable enough for a small load like a remote sensor node, a microprocessor or a driver circuit whose biasing voltage ranges from 2V to 5V. Though modern technology has made possible to lower the voltages of electronic devices nevertheless it has not been able to lower the voltage such that a single photovoltaic cell would be able to drive the entire load, let alone a sensor node where multiple sensors are connected. So energy harvesting only with a single photovoltaic cell no matter how attractive it sounds will fail to meet the practical need. One solution of this problem could be to use a number of photovoltaic cell connected in series and parallel but this would be bulky and limit the research which focuses on energy harvesting. To surpass the problem power electronic drivers could be used but still the same level of hindrance would be faced since all power electronic driver comprises of a switch (a BJT, a MOSFET or a SCR depending on the condition required) which should be driven by a driver circuit and the biasing voltages of these driver circuit is from 2V to 5 V.

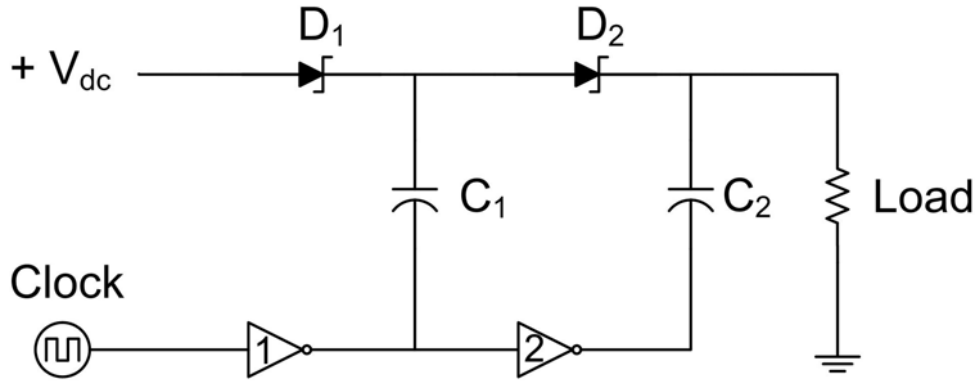


Figure 4.1: A simple charge pump circuit diagram

## 4.1 Converter Technology for Energy Harvesting

In order to solve the particular problem associated with high voltage (approximately 5V) two forms of startup circuits have gained prominence. They are circuits based on charge pumps and oscillator. The charge pump circuit is based on the topology of voltage doubler where depending on the output voltage required the number of inverters (made with an NMOS and a PMOS) are connected and each inverter increases voltage at each stage. Though in theory such type of circuit based on charge pump could achieve any amount of voltage but in practical condition such technique is quite a waste as it harms the basic underlying feature which focusses on reducing the number of switches and in this aspect the number of inverters which means more power loss in these devices as shown in Figure 4.1. For quite a long period of time such circuit could not be a better solution for driving a load. So in this study a recent solution towards this problem has been proposed and this is the oscillator based power converter [43,44].

### 4.1.1 Conventional Converter for Up Conversion of Voltage

Before discussing the oscillator based converter used in this study some analogy is drawn between a widely popular DC-DC converter known as the boost converter for up conversion of voltage. The boost converter is chosen for analogy as its mode

of operation is similar to the oscillator based converter. The circuit diagram of the boost converter is shown in Figure 4.2. Here two values of inductance is chosen such that it operates in continuous conduction mode (CCM) and discontinuous conduction mode (DCM) where the value of inductance remains at 25mH and 7.5mH respectively. CCM is referred to the condition when the inductor current stays positive for the entire switching time and DCM is the condition when the inductor current is interrupted such that it becomes zero for a particular time period in the switching time. But it has been discovered with the help of transient analysis that the inductor current actually goes negative for the converter circuit which is impossible for a conventional boost converter with a constant voltage source because as soon as the inductor current becomes negative the diode stops conducting and the current conduction path is eliminated (Figure 2.11(b)), this condition is popularly known as DCM. But here there is another path for the conduction of current. It is through the photovoltaic cell itself because unlike an ideal voltage source a photovoltaic cell has other elements when looked closely at its circuit parameters. A photovoltaic source has an ideal current source in parallel with a diode and parasitic shunt resistance; moreover, there is another series parasitic resistance attached to it. So the current conduction path is through the photovoltaic diode and parasitic shunt resistance when the inductor current becomes negative. The duty cycle and frequency of operation of the boost converter is taken to be 85.71% and 1kHz. These values are similar to the operating condition of oscillator based converter. The reason behind the choice of these parametric values is further discussed in **Section 4.2** with detailed Equation in 4.1 and 4.2.

Here, the output voltage and efficiency of the boost converter is observed by varying both the open circuit voltage ( $V_{oc}$ ) and short circuit current density ( $J_{sc}$ ) of the CZTSSe based photovoltaic cell such that it operates in the range between device A and device B as discussed in **Chapter 3**, this is also further shown in Table 4.3.



#### 4.1.1.1 Output Response by Varying $V_{oc}$ of conventional boost converter

In this part of the simulation work the output voltage and efficiency of the boost converter is observed by varying the  $V_{oc}$  of the photovoltaic cell while keeping  $J_{sc}$  constant as observed in both device B and device A respectively and also the  $FF$  is kept constant at 69%. The simulation results are tabulated in Table 4.1 and the output response is plotted in Figure 4.3. It is observed from the figure that both  $V_{out}$  and Efficiency of the converter is directly proportional to  $V_{oc}$  of the photovoltaic device irrespective of the mode of operation of the converter (CCM and DCM). This particular characteristic is further summarized in the following subsection.

#### 4.1.1.2 Output Response by Varying $J_{sc}$ of conventional boost converter

Here, the output voltage and efficiency of the boost converter is observed by varying the  $J_{sc}$  of the photovoltaic device while keeping  $V_{oc}$  constant as observed in both device B and device A respectively and also the  $FF$  is kept constant at 69%. The simulation results are tabulated in Table 4.2 and the output response is plotted in Figure 4.4. It is discovered from the figure that both  $V_{out}$  and Efficiency of

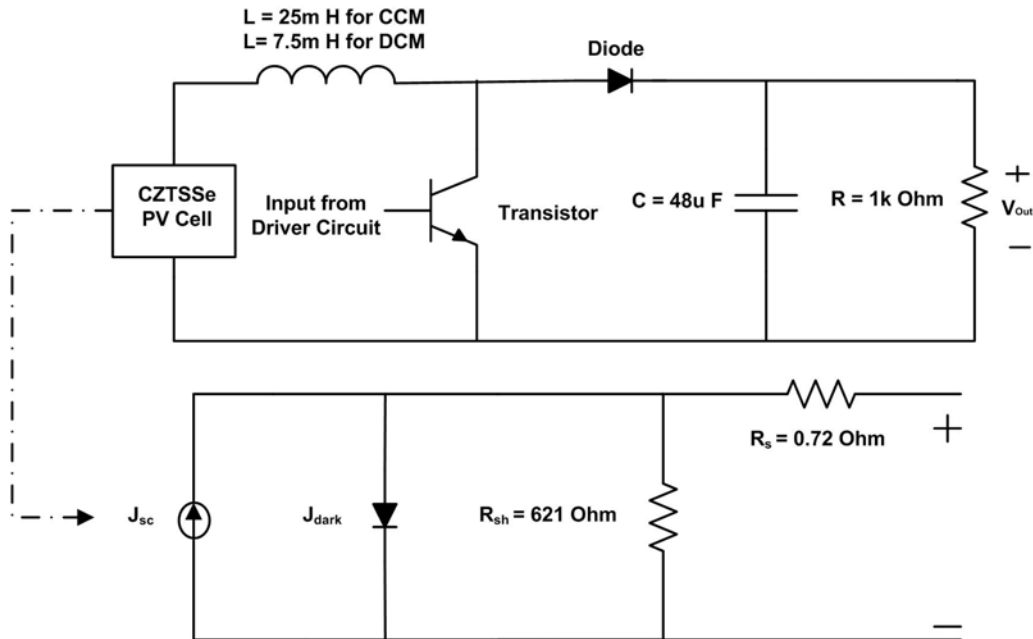


Figure 4.2: Circuit diagram of conventional boost converter with equivalent circuit of CZTSSe PV cell

Table 4.1: Varying  $V_{oc}$  while keeping  $FF$  and  $J_{sc}$  constant for both device A and device B (CCM parameters are tabulated without parenthesis and DCM parameters are tabulated in parenthesis of conventional boost converter)

Device A							
PV Device Parameters						Boost Converter Parameters	
$V_{oc}$ (mV)	$J_{sc}$ (mAcm <sup>-2</sup> )	$V_{max}$ (mV)	$J_{max}$ (mAcm <sup>-2</sup> )	FF (%)	$\eta_{solar}$ (%)	$V_{out}$ (V)	$\eta_{boost}$ (%)
688.5	35.2	557	30.05	69.06	16.74	2.862 (1.947)	60.99 (54.28)
653.5	35.2	529	30.05	69.11	15.90	2.820 (1.925)	60.88 (54.21)
618.5	35.2	501	30.05	69.15	15.06	2.763 (1.904)	60.72 (54.14)
583.5	35.2	472	30.05	69.06	14.18	2.677 (1.881)	60.46 (54.04)
548.5	35.2	444	30.05	69.10	13.34	2.552 (1.847)	59.95 (53.88)
514.2	35.2	416	30.05	69.07	12.50	2.395 (1.799)	59.79 (54.36)
Device B							
PV Device Parameters						Boost Converter Parameters	
$V_{oc}$ (mV)	$J_{sc}$ (mAcm <sup>-2</sup> )	$V_{max}$ (mV)	$J_{max}$ (mAcm <sup>-2</sup> )	FF (%)	$\eta_{solar}$ (%)	$V_{out}$ (V)	$\eta_{boost}$ (%)
688.5	30.85	557	26.32	69.02	14.66	2.540 (1.706)	58.92 (51.58)
653.5	30.85	529	26.32	69.06	13.92	2.513 (1.685)	58.82 (51.48)
618.5	30.85	501	26.32	69.10	13.19	2.482 (1.664)	58.71 (50.55)
583.5	30.85	472	26.32	69.01	12.42	2.439 (1.643)	58.55 (51.26)
548.5	30.85	444	26.32	69.06	11.69	2.381 (1.622)	58.31 (51.16)
514.2	30.85	416	26.32	69.02	10.95	2.291 (1.600)	57.92 (51.02)

the converter is directly proportional to  $J_{sc}$  of the photovoltaic device. Here this condition also holds true for the mode of operation of the converter (CCM and DCM).

The output characteristics of the conventional boost converter operating in both CCM and DCM is plotted in order to form an analogy with the oscillator

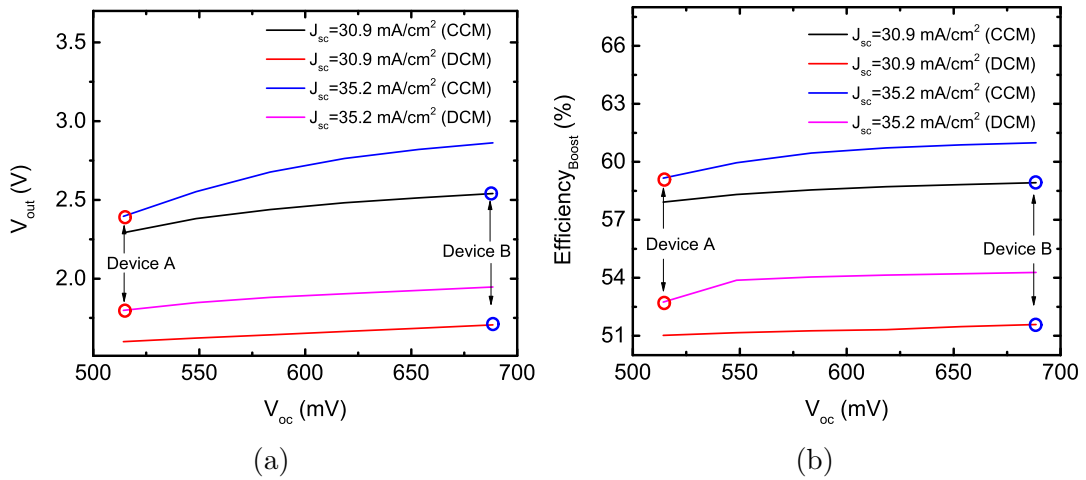


Figure 4.3: (a)  $V_{out}$  as a function of  $V_{oc}$  and (b) Efficiency as a function of  $V_{oc}$  of conventional boost converter [Device A and Device B indicate the actual operating point]

Table 4.2: Varying  $J_{sc}$  while keeping  $FF$  and  $V_{oc}$  constant for both device A and device B (CCM parameters are tabulated without parenthesis and DCM parameters are tabulated in parenthesis of conventional boost converter)

Device A							
PV Device Parameters						Boost Converter Parameters	
$V_{oc}$ (mV)	$J_{sc}$ (mAcm <sup>-2</sup> )	$V_{max}$ (mV)	$J_{max}$ (mAcm <sup>-2</sup> )	FF (%)	$\eta_{solar}$ (%)	$V_{out}$ (V)	$\eta_{boost}$ (%)
514.2	30.85	416	26.32	69.02	10.95	2.291 (1.600)	57.92 (51.02)
514.2	31.72	416	27.10	69.12	11.27	2.320 (1.647)	58.25 (51.65)
514.2	32.59	416	27.80	69.01	11.56	2.342 (1.693)	58.51 (52.21)
514.2	33.46	416	28.60	69.15	11.89	2.363 (1.741)	58.75 (52.79)
514.2	34.33	416	29.30	69.05	12.19	2.379 (1.787)	58.96 (53.32)
514.2	35.20	416	30.05	69.07	12.50	2.395 (1.836)	59.16 (53.87)
Device B							
PV Device Parameters						Boost Converter Parameters	
$V_{oc}$ (mV)	$J_{sc}$ (mAcm <sup>-2</sup> )	$V_{max}$ (mV)	$J_{max}$ (mAcm <sup>-2</sup> )	FF (%)	$\eta_{solar}$ (%)	$V_{out}$ (V)	$\eta_{boost}$ (%)
688.5	30.85	557	26.32	69.02	14.66	2.540 (1.706)	58.92 (51.58)
688.5	31.72	557	27.10	69.11	15.09	2.607 (1.754)	59.38 (52.18)
688.5	32.59	557	27.80	69.00	15.48	2.671 (1.799)	59.79 (52.70)
688.5	33.46	557	28.60	69.15	15.93	2.738 (1.851)	60.23 (53.29)
688.5	34.33	557	29.30	69.05	16.32	2.800 (1.898)	60.61 (53.79)
688.5	35.20	557	30.05	69.06	16.74	2.862 (1.947)	60.99 (54.29)

based converter. It is later shown in **Section 4.2** that the conventional converter operating in DCM closely resembles the oscillator based converter used in this study.

To summarize the results of Table 4.1 and 4.2 it can be stated that the simulation of the conventional boost converter circuit with high  $J_{sc}$  and high  $V_{oc}$  has higher

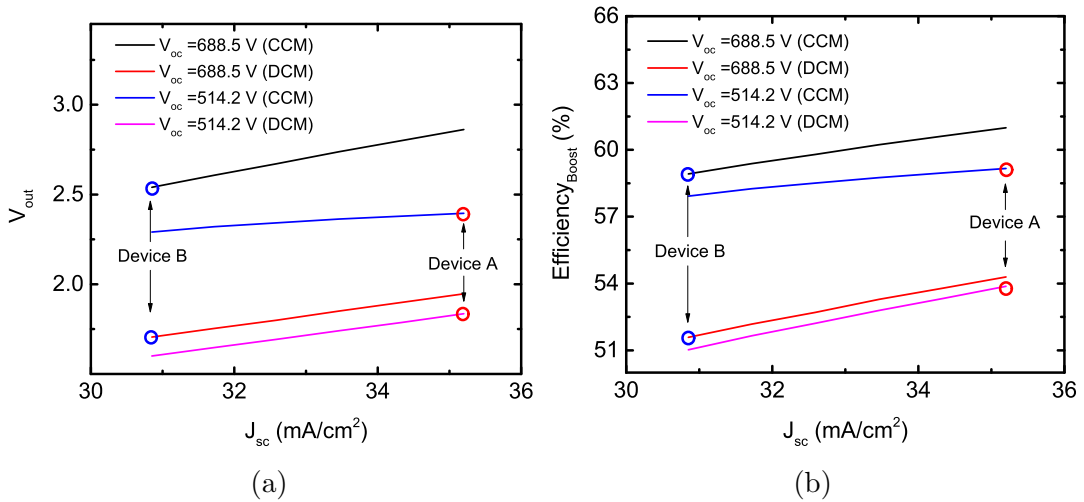


Figure 4.4: (a)  $V_{out}$  as a function of  $J_{sc}$  and (b) Efficiency as a function of  $J_{sc}$  of conventional boost converter [Device A and Device B indicate the actual operating point]

output voltage and output efficiency respectively. Though the results are obtained for the sake of simulation in reality such high values of  $J_{sc}$  and  $V_{oc}$  may not be achieved with device A and B. In practice the operating point of device A and B are circled in the Figure 4.3 and 4.4 when operated with a conventional boost converter which reveals that device B with the converter has higher  $V_{out}$  and lower efficiency when compared to device A with the converter.

### 4.1.2 Oscillator Based Converter

The oscillator circuit is based on the topology of Meissner oscillator [44]. The oscillator drives the switch used in the power electronic circuit where no additional circuit is required to drive the switch, as a result it saves power in low power devices and being a self-driven circuit it could power up a sensor node. The oscillator circuit takes power from the secondary side of a transformer or a mutual inductance or of an inductor having the same inductance from the side with alternate polarity connected in series with the switch. The concept of using the alternate polarity is to provide the switching signal for the switch used in the converter. For the purpose of this study JFET is used as the switching device unlike other conventional switches where MOSFET, BJT or SCR is used. JFET is not suitable for high power and high frequency converter as its high frequency performance is not optimal and for this study the Meissner oscillator keeps the frequency of JFET to be around the 1 kHz mark. This particular frequency and low power application makes it a wise choice for using JFET as the switch of the design. But the main reason behind the use of JFET lies in the concept of its working principle as unlike other conventional switches JFET conducts in its natural state and a negative voltage has to be provided to its gate to turn it off or to stop conducting. The same result could also be achieved by using a depletion type MOSFET which is also a normally ‘ON’ device. The main problem in other circuit design was to turn on the switch with an energy harvesting device such as a photovoltaic cell which is proposed earlier in **Chapter 3** so that energy stored in the inductance could be transferred to the load and in this design consideration the switch remains ‘ON’ in its natural state. The block diagram of the converter is shown in Figure 4.5.

Here the boost converter topology has been used for driving a load with the proposed photovoltaic cells. But there are some modifications in the design compared to a conventional boost converter. Instead of a simple inductance there are some other choices which could do the same task of the inductor like a transformer which is more common in the design of a flyback converter or a mutual inductance. The size and turns of the transformer if used is not relevant to the design as the purpose of the transformer is to provide opposite polarity which could also be achieved with a mutual inductance or simply an inductor having the same equivalent inductance. So to reduce the size mutual inductance could be an advantageous design choice. During the startup condition the current through the primary inductance increases, this causes the JFET to conduct and as a result opposite polarity voltage is induced in the secondary inductance. The size of the inductance is chosen such that it goes quickly in the saturation condition which further makes sure for the smaller size of the inductor. Thus in the saturation condition the current through the primary inductance does not increase further, this condition of current being limited could also be achieved by choosing a JFET whose on state resistance lies in the  $50\Omega$  range. At the same time opposite polarity voltage in the secondary winding increases such that the JFET becomes pinched off and stops conducting. This opposite voltage is dissipated by the Meissner based oscillator formed with the combination of capacitor and inductor. The capacitor and inductor of the oscillator circuit determines both the switching frequency and duty cycle of the JFET. For the given parameter the switching frequency of the driver was around 1 kHz and the duty cycle remained in the vicinity of 85.71% [102, 103]. The design concept with the relevant parameters are shown in Figure 4.6.

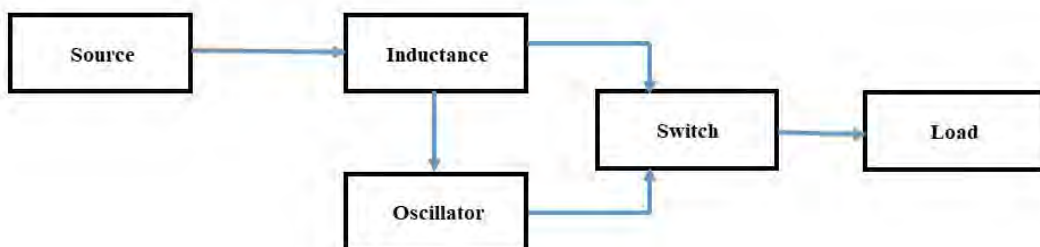


Figure 4.5: Block diagram of the design

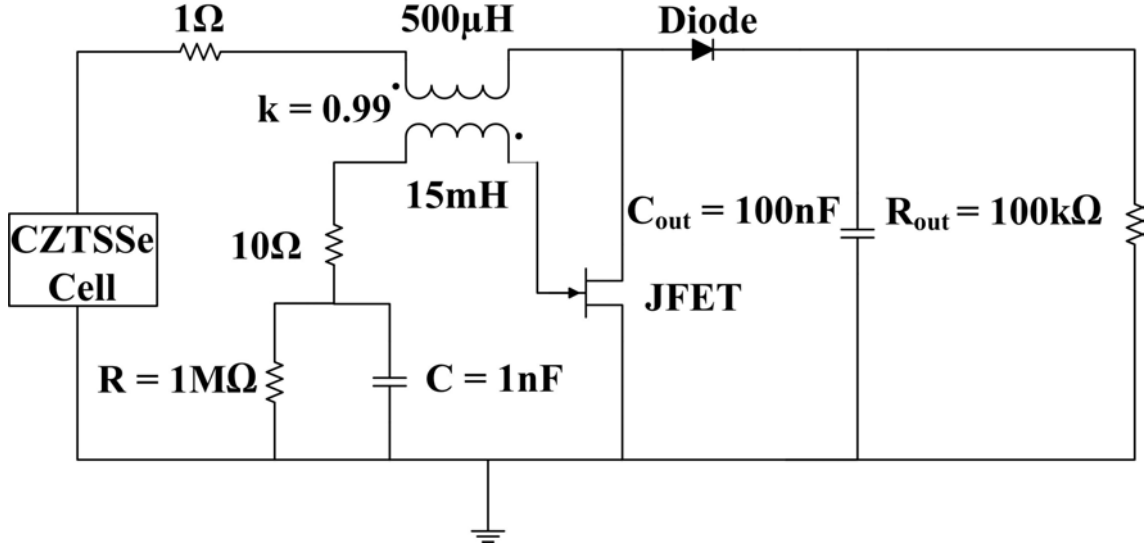


Figure 4.6: Circuit diagram of the converter

Similar simulation work has been performed by taking a depletion type MOSFET such that its gate to source biasing voltage remains at 1.7V and the gate to source threshold voltage remains at -0.12V. By ensuring this condition similar level of output performance can be achieved when compared with a JFET whose gate to source biasing voltage remains at 0V.

### 4.1.3 Output Response of Oscillator Based Converter

For testing the output performance of the converter the previously studied PV devices have been considered as the input source. One of them is device A, the other one is device B proposed in this work. Device B has higher  $V_{oc}$  but lower  $J_{sc}$  and  $FF$  but the overall efficiency is higher whereas device A has lower  $V_{oc}$  but higher  $J_{sc}$  and  $FF$  but the overall efficiency is lower. Both of their parameters are shown in Table 4.3. For getting a deep understanding of the converter the performance limiting parameters ( $V_{oc}$ ,  $J_{sc}$  and  $FF$ ) of both the cell have been taken as the boundary condition. A wide range of simulations by varying the open circuit voltage while keeping short circuit current, maximum voltage and maximum current constant and vice versa have been done which would be described subsequently.

#### 4.1.3.1 Output Response by Varying $FF$ of Oscillator Based Converter

In the first part of the simulation work the  $FF$  of device B is varied while keeping everything constant and the performance of the converter is checked. From the simulation work a very subtle change in the performance of the driver circuit is found which is shown in Table 4.4. Because of subtlety of the output response especially the output voltage change, it is deemed that the variance is caused by error employed in numerical analysis and as such the simulation by varying the  $FF$  for device A is not proceed further. This needs to be mentioned that all simulation results are taken when the driver circuit has reached steady state.

#### 4.1.3.2 Output Response by Varying $V_{oc}$ of Oscillator Based Converter

In the next part of the simulation work  $V_{oc}$  is varied while keeping  $J_{sc}$  and  $FF$  constant. This is done for both the CZTSSe-based photovoltaic devices and the output response is tabulated in Table 4.5. It is quite insightful to note that device B performed poorly with the converter compared to device A with the converter. The results are also plotted ( $V_{out}$  and efficiency) in Figure 4.7 to get a precise idea about what is happening with the converter. This particular outcome has deemed it necessary to further look into other parameters of the device and carry out the simulation by varying those.

#### 4.1.3.3 Output Response by Varying $J_{sc}$ of Oscillator Based Converter

Finally, for the steady state simulation,  $J_{sc}$  is varied while keeping both  $V_{oc}$  and  $FF$  constant for both the devices. This particular approach also led to the earlier findings where device A performed better with the converter circuit. The findings

Table 4.3: Parametric value of both device

Cell Design	$V_{oc}$ (mV)	$J_{sc}$ (mAcm <sup>-2</sup> )	FF (%)	Efficiency (%)
Device A	514.2	35.2	69.8	12.6
Device B	688.5	30.85	66.45	14.1

Table 4.4: Varying  $FF$  while keeping  $V_{oc}$  and  $J_{sc}$  constant for device B

PV Device Parameters						Oscillator Based Converter Parameters	
$V_{oc}$ (mV)	$J_{sc}$ (mAcm <sup>-2</sup> )	$V_{max}$ (mV)	$J_{max}$ (mAcm <sup>-2</sup> )	$FF$ (%)	$\eta_{solar}$ (%)	$V_{out}$ (V)	$\eta_{oscillator}$ (%)
688.5	30.85	552.63	25.54	66.45	14.11	5.852	20.40
688.5	30.85	557	25.55	67	14.23	5.864	20.43
688.5	30.85	564	25.61	68	14.44	5.895	20.55
688.5	30.85	571	25.67	69	14.66	5.918	20.60
688.5	30.85	574	25.93	70	14.88	5.975	20.92

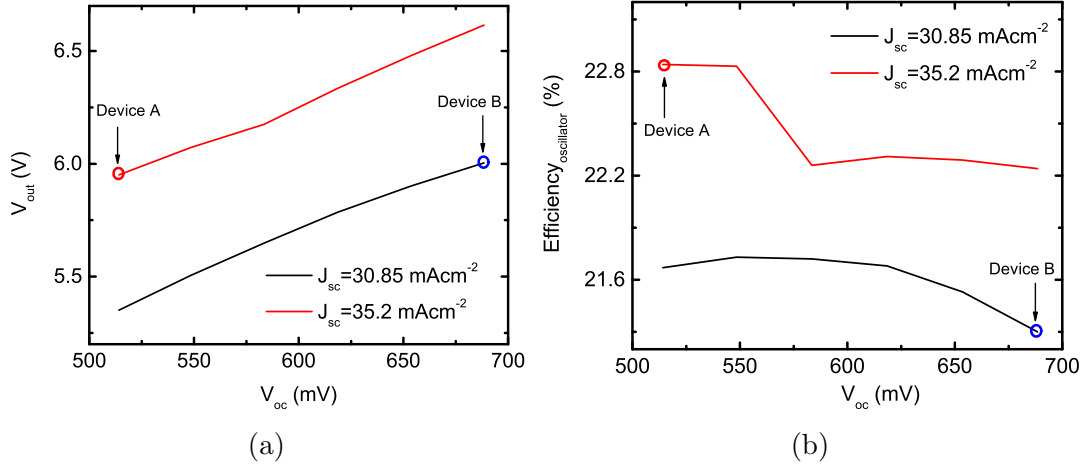


Figure 4.7: (a)  $V_{out}$  as a function of  $V_{oc}$  and (b) Efficiency as a function of  $V_{oc}$  [Device A and Device B indicate the actual operating point]

are tabulated in Table 4.6 and plotted in Figure 4.8. The simulation results though quite insightful did not provide with enough data about the reason behind the better performance of device A with the converter which has an overall inferior

Table 4.5: Varying  $V_{oc}$  while keeping  $FF$  and  $J_{sc}$  constant for both device A and device B of oscillator based converter

Device A							
PV Device Parameters						Oscillator Based Converter Parameters	
$V_{oc}$ (mV)	$J_{sc}$ (mAcm <sup>-2</sup> )	$V_{max}$ (mV)	$J_{max}$ (mAcm <sup>-2</sup> )	$FF$ (%)	$\eta_{solar}$ (%)	$V_{out}$ (V)	$\eta_{oscillator}$ (%)
688.5	35.2	557	30.05	69.06	16.74	6.615	22.24
653.5	35.2	529	30.05	69.11	15.90	6.479	22.29
618.5	35.2	501	30.05	69.15	15.06	6.334	22.31
583.5	35.2	472	30.05	69.06	14.18	6.175	22.26
548.5	35.2	444	30.05	69.10	13.34	6.072	22.83
514.2	35.2	416	30.05	69.07	12.50	5.951	22.84
Device B							
PV Device Parameters						Oscillator Based Converter Parameters	
$V_{oc}$ (mV)	$J_{sc}$ (mAcm <sup>-2</sup> )	$V_{max}$ (mV)	$J_{max}$ (mAcm <sup>-2</sup> )	$FF$ (%)	$\eta_{solar}$ (%)	$V_{out}$ (V)	$\eta_{oscillator}$ (%)
688.5	30.85	557	26.32	69.02	14.66	6.004	21.30
653.5	30.85	529	26.32	69.06	13.92	5.901	21.53
618.5	30.85	501	26.32	69.10	13.19	5.785	21.68
583.5	30.85	472	26.32	69.01	12.42	5.648	21.72
548.5	30.85	444	26.32	69.06	11.69	5.505	21.73
514.2	30.85	416	26.32	69.02	10.95	5.351	21.67



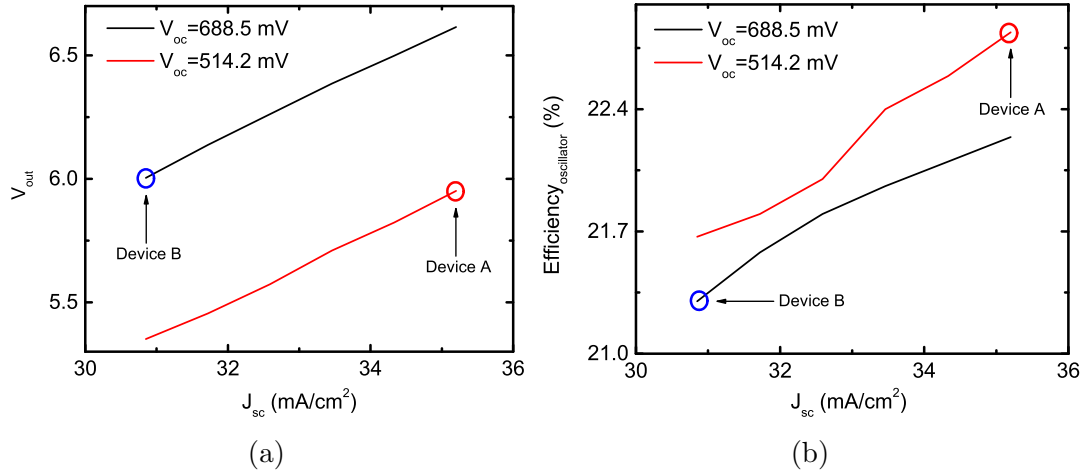


Figure 4.8: (a)  $V_{out}$  as a function of  $J_{sc}$  and (b) Efficiency as a function of  $J_{sc}$  of oscillator based converter [Device A and Device B indicate the actual operating point]

efficiency compared to device B that has been proposed. One hypothesis that could be reached is that the input photovoltaic source which have higher short circuit current will perform better with converter circuit compared to input photovoltaic source having higher open circuit voltage. In order to impose this hypothesis, the simulation should be approached from other point which is the transient analysis of the entire circuit at each element.

Table 4.6: Varying  $J_{sc}$  while keeping  $FF$  and  $V_{oc}$  constant for both device A and device B

Device A								
PV Device Parameters						Oscillator Based Converter Parameters		
$V_{oc}$ (mV)	$J_{sc}$ (mAcm <sup>-2</sup> )	$V_{max}$ (mV)	$J_{max}$ (mAcm <sup>-2</sup> )	FF (%)	$\eta_{solar}$ (%)	$V_{out}$ (V)	$\eta_{oscillator}$ (%)	
514.2	30.85	416	26.32	69.02	10.95	5.351	21.67	
514.2	31.72	416	27.10	69.12	11.27	5.455	21.80	
514.2	32.59	416	27.80	69.01	11.56	5.573	22.00	
514.2	33.46	416	28.60	69.15	11.89	5.710	22.40	
514.2	34.33	416	29.30	69.05	12.19	5.823	22.59	
514.2	35.20	416	30.05	69.07	12.50	5.951	22.84	
Device B								
PV Device Parameters						Oscillator Based Converter Parameters		
$V_{oc}$ (mV)	$J_{sc}$ (mAcm <sup>-2</sup> )	$V_{max}$ (mV)	$J_{max}$ (mAcm <sup>-2</sup> )	FF (%)	$\eta_{solar}$ (%)	$V_{out}$ (V)	$\eta_{oscillator}$ (%)	
688.5	30.85	557	26.32	69.02	14.66	6.004	21.30	
688.5	31.72	557	27.10	69.11	15.09	6.138	21.58	
688.5	32.59	557	27.80	69.00	15.48	6.262	21.80	
688.5	33.46	557	28.60	69.15	15.93	6.386	21.72	
688.5	34.33	557	29.30	69.05	16.32	6.499	22.10	
688.5	35.20	557	30.05	69.06	16.74	6.615	22.24	

## 4.2 Transient Analysis with Conventional Boost Converter

The analysis of the entire circuit led to one particular insightful finding. It has been discovered that the inductor current actually goes negative for the designed converter circuit. When the inductor current is negative, the current conduction path is through oscillator circuit of the converter which is the marvel of the design and the other conduction path is through the photovoltaic diode and parasitic shunt resistance of the photovoltaic device. This condition holds true for a conventional converter operating in DCM which is revealed with transient analysis.

For a conventional boost converter, same switching frequency and duty cycle have been used. From the Equation 4.1 and 4.2 the minimum value of inductance and capacitance is obtained to keep the mode of operation in the continuous conduction mode and ripple factor to be around 8.57%.

$$L_{\min} = \frac{D(1-D)^2 R}{2f} \quad (4.1)$$

$$C = \frac{D}{R(\Delta V_0/V) f} \quad (4.2)$$

Here,  $D$  is the duty cycle,  $f$  is the switching frequency,  $R$  is the output load resistance which is the same as the previous oscillator based circuit and  $\Delta V_0/V$  is the output ripple voltage. Following Equation 4.1 it is needed to maintain the value of inductance above the  $L_{\min}$  to keep the mode of operation in the continuous conduction mode and if it is kept below the  $L_{\min}$  value the mode of operation will change to discontinuous conduction mode, for the purpose of simulation the value of inductor has been taken to be 25mH which is well above the calculated value of 8.75mH so that it remains in the continuous conduction mode. Equation 4.2 is widely used for calculating the value of the capacitance for keeping the value of ripple within the allowed margin.

In order to check whether the inductor current becomes negative in the discontinuous conduction mode the help of transient analysis along with the previous oscillator based circuit has been taken into account and the results with plots are explained in the following sections.

#### **4.2.1 Transient Analysis of Device A with Conventional Converter**

The transient analysis of device A with the conventional converter in CCM shows that it reaches close to steady state in 6ms and in that time it takes around 4.5 switching cycles. During this time the output voltage reaches 1.79V a higher value than device B during this time but its steady state output voltage is lower compared to device B and the inductor current reaches 34.6mA in CCM. The interesting feature from this analysis is that device A reaches steady state a bit quicker than device B. This is depicted in Figure 4.9 . On the other hand device A completes 7.5 switching cycles in 6ms in this time the inductor current reaches a value of 34.6mA in DCM. The output voltage at this time reaches 1.54V which is lower than the CCM operation. Here the inductor current has a steeper downward slope in DCM compared to CCM. This condition also holds when compared to the DCM operation mode of device B, the plot of inductor current is taken for 20ms where in this time the inductor current reaches negative. This is depicted in Figure 4.10.

#### **4.2.2 Transient Analysis of Device B with Conventional Converter**

The transient analysis of device B with the conventional converter in CCM shows that it reaches close to steady state in 6ms and in that time it takes around 5.5 switching cycles. In this time the output voltage reaches a value of 1.666V and the inductor current reaches 30mA. This is depicted in Figure 4.11. On the other hand in DCM device B completes 6.5 switching cycles in 6ms and in this time the inductor current reaches a value of 30mA. The output voltage at this time reaches

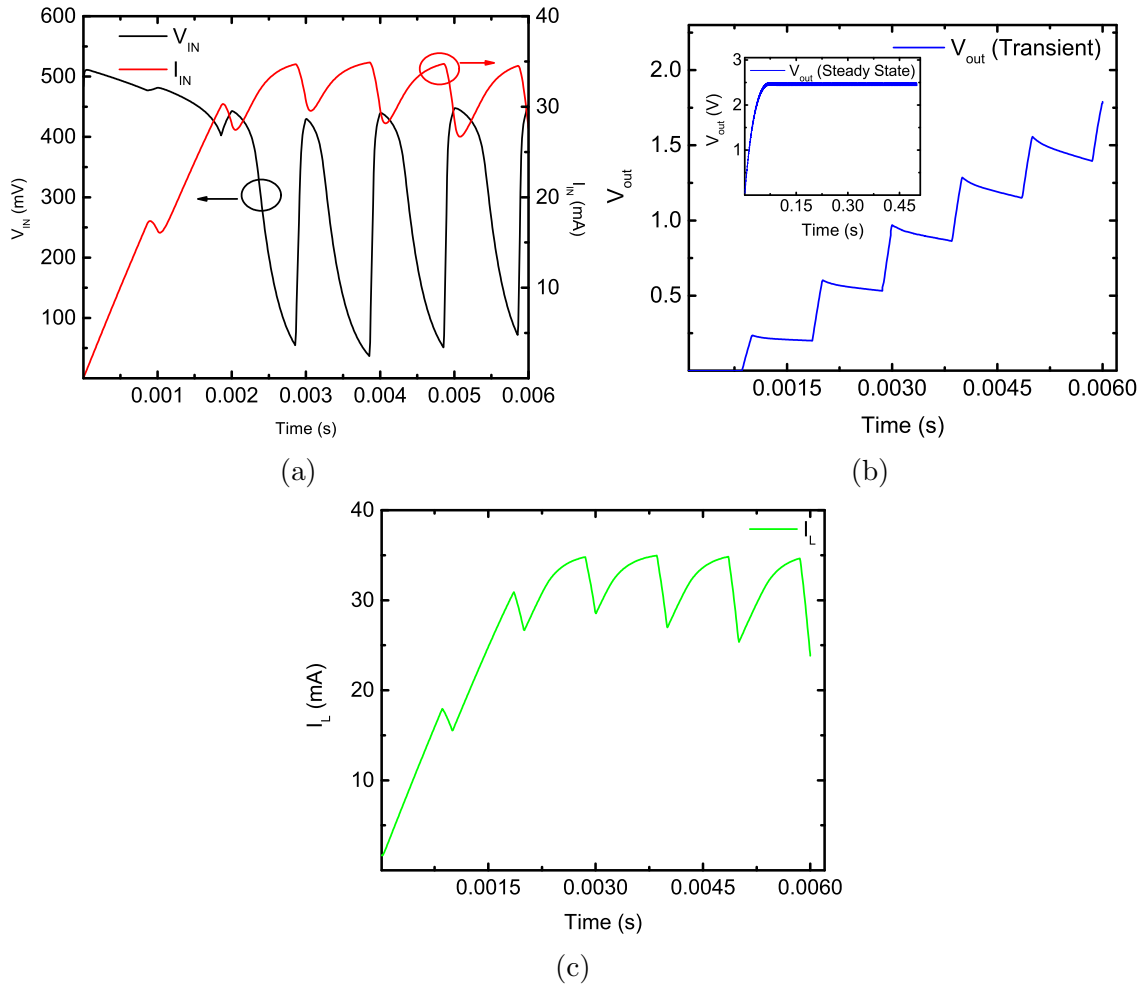


Figure 4.9: Device A in CCM with conventional boost converter (a)  $V_{in}$  and  $I_{in}$  with time (b)  $V_{out}$  with time [inset:  $V_{out}$  with time in steady state] and (c) Inductor current ( $I_L$ ) with time

1.4V which is lower than the CCM operation. Since the inductor current has a steeper downward slope in DCM compared to CCM, the plot of inductor current is taken for 30ms where in this time the inductor current reaches negative. This is depicted in Figure 4.12.

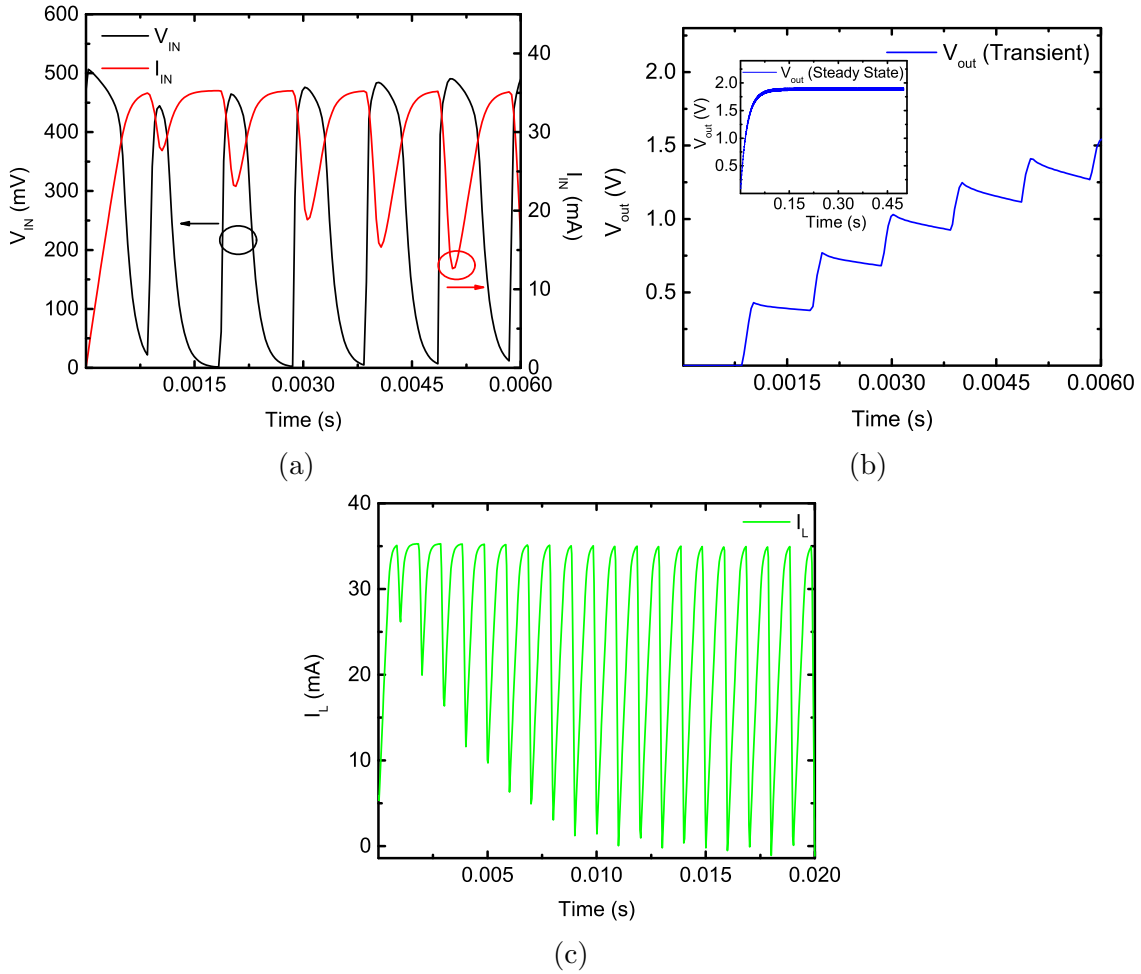


Figure 4.10: Device A in DCM with conventional boost converter (a)  $V_{in}$  and  $I_{in}$  with time (b)  $V_{out}$  with time [inset:  $V_{out}$  with time in steady state] and (c) Inductor current ( $I_L$ ) with time

## 4.3 Transient Analysis with Oscillator Based Converter

### 4.3.1 Transient Analysis of Device A with Oscillator Based Converter

The transient analysis of device A with the oscillator based converter shows that it reaches close to steady state in 6ms and in that time it takes around 5.5 switching cycles. In this time the output voltage reaches a value of 3.769V where as the steady state value is 5.951V and the inductor current goes negative in the first switching cycle. This is depicted in Figure 4.13. This shows that the steady state is reached a lot quicker than the conventional converter. Another unique feature

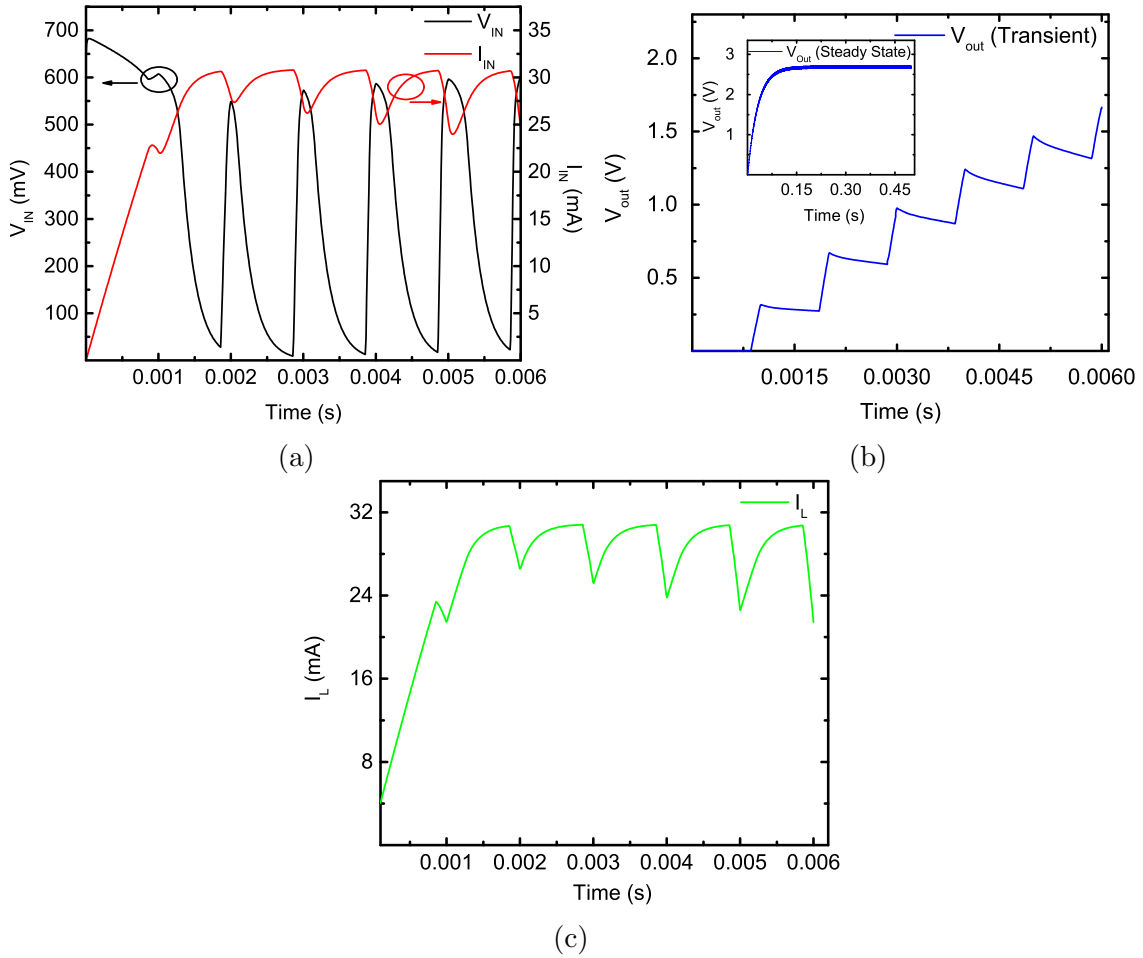


Figure 4.11: Device B in CCM with conventional boost converter (a)  $V_{in}$  and  $I_{in}$  with time (b)  $V_{out}$  with time [inset:  $V_{out}$  with time in steady state] and (c) Inductor current ( $I_L$ ) with time

about this analysis is that the steady state is reached quicker with device A when driven with an oscillator-based converter compared to device B with the converter.

### 4.3.2 Transient Analysis of Device B with Oscillator Based Converter

The transient analysis of device B with the oscillator based converter shows that it reaches close to steady state in 6ms and in that time it takes around 5.5 switching cycles. In this time the output voltage reaches a value of 4.08V where as the steady state value is 6.004V and the inductor current goes negative in the first switching cycle. This is depicted in Figure 4.14. This shows that the steady state is reached a lot quicker than the conventional converter.

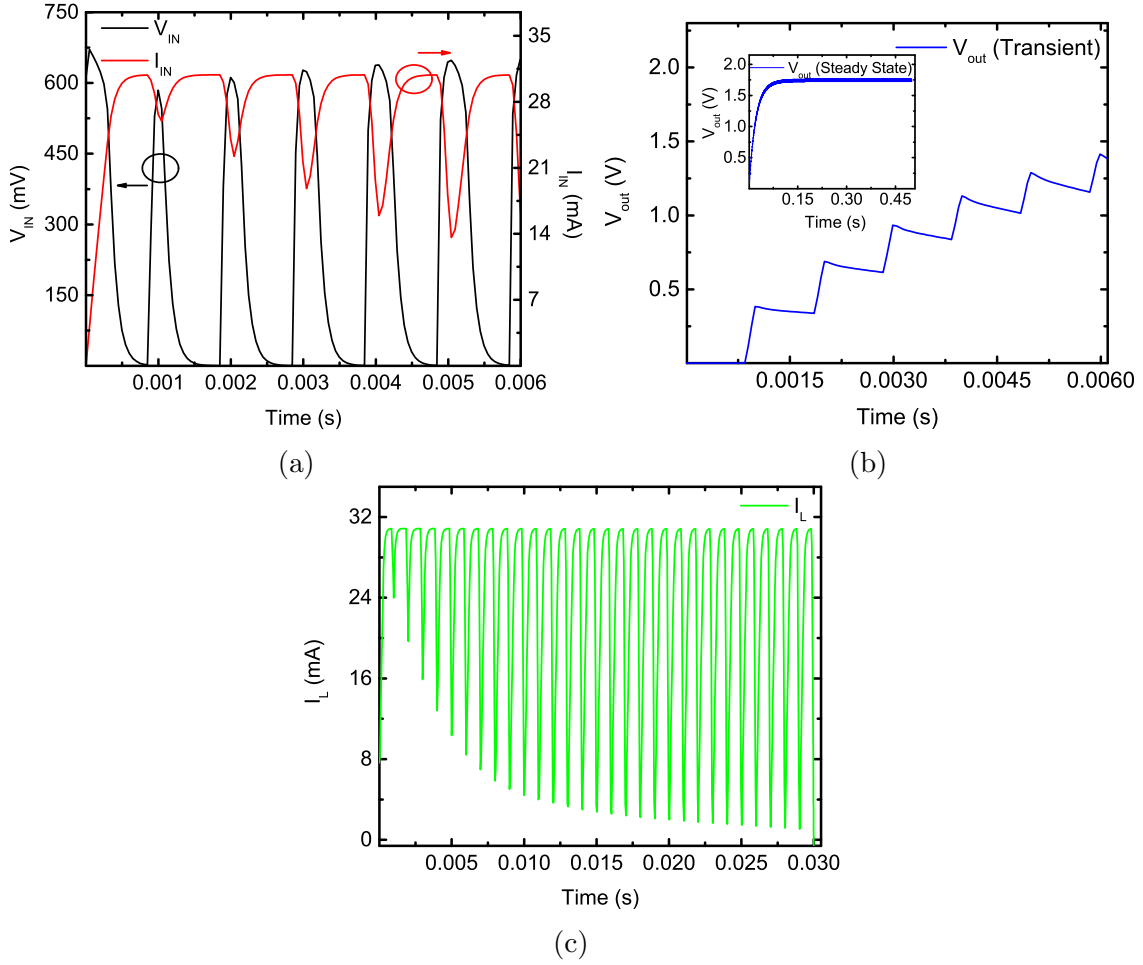


Figure 4.12: Device B in DCM with conventional boost converter (a)  $V_{in}$  and  $I_{in}$  with time (b)  $V_{out}$  with time [inset:  $V_{out}$  with time in steady state] and (c) Inductor current ( $I_L$ ) with time

## 4.4 Optimization of Oscillator Converter

In the oscillator based converter there are two circuit components that could be further optimized for having a better output performance. They are the R, C component of the oscillator circuit and the  $R_{out}$ ,  $C_{out}$  component of the output load where  $C_{out}$  is the ripple capacitor. The optimization process of the converter is deemed necessary as the efficiency of the converter is quite low when compared with a conventional boost converter. So the optimization process is done to increase the efficiency at the cost of the output voltage such that its output voltage remains higher when compared with a conventional boost converter but at the same time

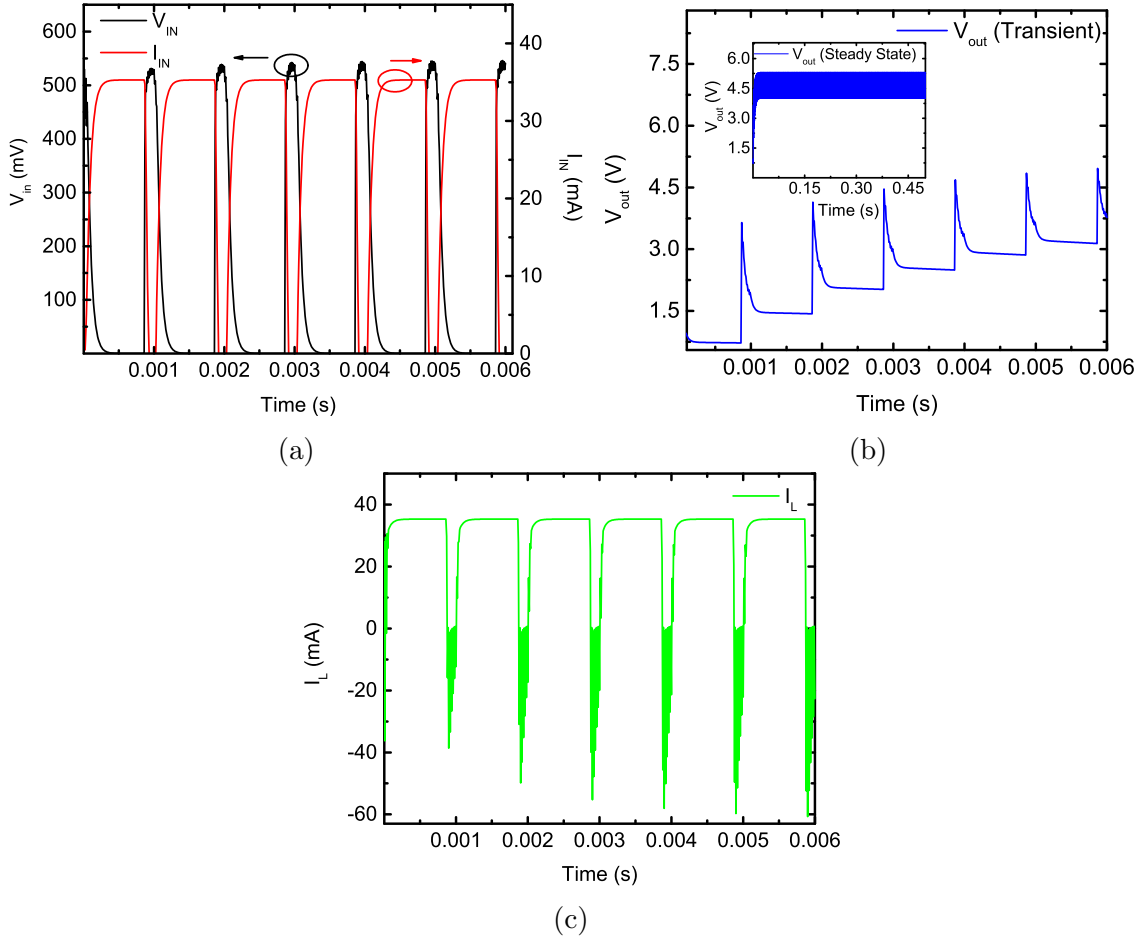


Figure 4.13: Device A with oscillator-based converter (a)  $V_{in}$  and  $I_{in}$  with time (b)  $V_{out}$  with time [inset:  $V_{out}$  with time in steady state] and (c) Inductor current ( $I_L$ ) with time

its efficiency increases. The simulation is done taking both device A and device B as the source.

In this part of the study the simulation is done by varying the ripple capacitor at three steps as shown in Table 4.7 while keeping the output load constant. The output load is also varied later at three steps with the ripple capacitor constant. The entire result is further plotted in Figure 4.15 for getting a better visualization of the tabulated data.

From the simulation results it is understood that with higher load the output voltage increases but the efficiency decreases. And with higher ripple capacitor the output voltage increases at first but later decreases with load (for high value of load) or becomes more or less constant (for low value of load). The efficiency profile



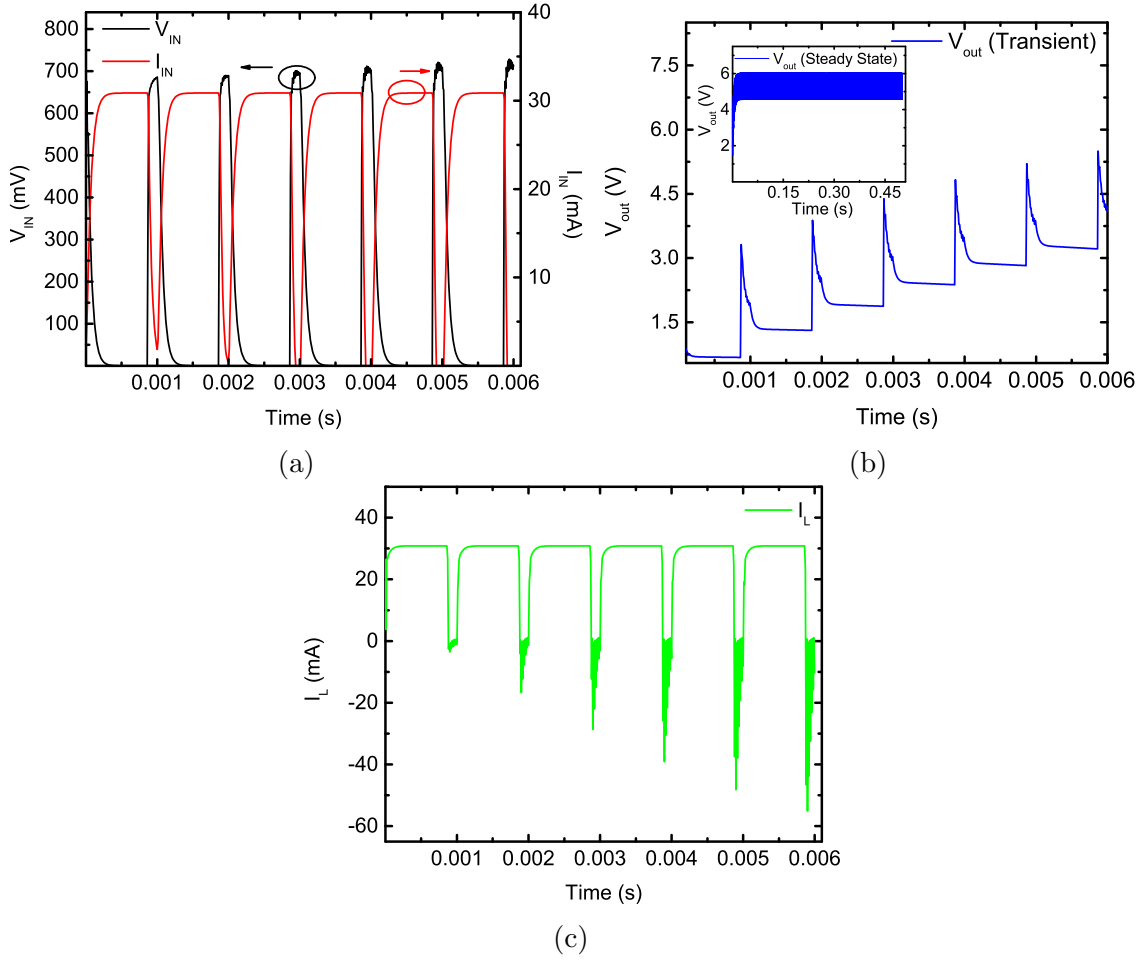


Figure 4.14: Device B with oscillator-based converter (a)  $V_{in}$  and  $I_{in}$  with time (b)  $V_{out}$  with time [inset:  $V_{out}$  with time in steady state] and (c) Inductor current ( $I_L$ ) with time

has inverse relation, here with low load the efficiency increases and becomes more or less constant with the increase of ripple capacitor on the other hand the efficiency rather decreases with ripple capacitor for high value of load. From the simulation result the optimized value of the ripple capacitor can be taken as  $1 \times 10^{-6} \text{F}$  but the optimized value of the load is still unclear. So, further simulation is done varying the oscillator circuit parameter with a hypothetical optimized value of the  $R_{out}$  and  $C_{out}$  of the output load.

For optimizing the oscillator component of the converter three values of the output load is taken as the hypothetical optimized value they are  $R_{out}$  and  $C_{out}$  value pair where the value pairs are  $100 \text{k}\Omega$ ,  $1 \times 10^{-6} \text{F}$ ;  $50 \text{k}\Omega$ ,  $1 \times 10^{-6} \text{F}$  and  $10 \text{k}\Omega$ ,  $1 \times 10^{-6} \text{F}$ . For the purpose of simulation these value pairs are termed as optimization

Table 4.7: Opimization of the oscillator converter varying the output load and ripple capacitor

<b>Device A</b>			
$\mathbf{R}_{out}$ ( $\Omega$ )	$\mathbf{C}_{out}$ (F)	$\mathbf{V}_{out}$ (V)	$\eta_{oscillator}$ (%)
100k	1E-07	5.951	22.84
	1E-06	6.085	23.24
	1E-05	5.474	18.65
50k	1E-07	4.584	27.19
	1E-06	4.831	29.18
	1E-05	4.660	26.94
10k	1E-07	2.089	29.45
	1E-06	2.461	37.19
	1E-05	2.471	37.03
<b>Device B</b>			
$\mathbf{R}_{out}$ ( $\Omega$ )	$\mathbf{C}_{out}$ (F)	$\mathbf{V}_{out}$ (V)	$\eta_{oscillator}$ (%)
100k	1E-07	6.023	21.85
	1E-06	6.211	22.40
	1E-05	5.552	17.77
50k	1E-07	4.685	26.57
	1E-06	4.887	27.66
	1E-05	4.728	25.64
10k	1E-07	2.134	28.89
	1E-06	2.501	35.51
	1E-05	2.509	35.21

(1), optimization (2) and optimization (3) respectively.

For each value of optimization of the output parameters, two further value pairs of optimization of the RC oscillator are selected they are 100k $\Omega$ , 1x10<sup>-8</sup>F and 1M $\Omega$ , 1x10<sup>-9</sup>F respectively. They are termed as RC optimization (1) and RC optimization (2) respectively. The optimization value pairs of the RC oscillator are chosen such that their product has a time constant which inversely becomes equal to 1kHz becoming equal to the initial switching frequency. The results are shown in Table 4.8 and further plotted in Figure 4.16 for getting a better visualization.

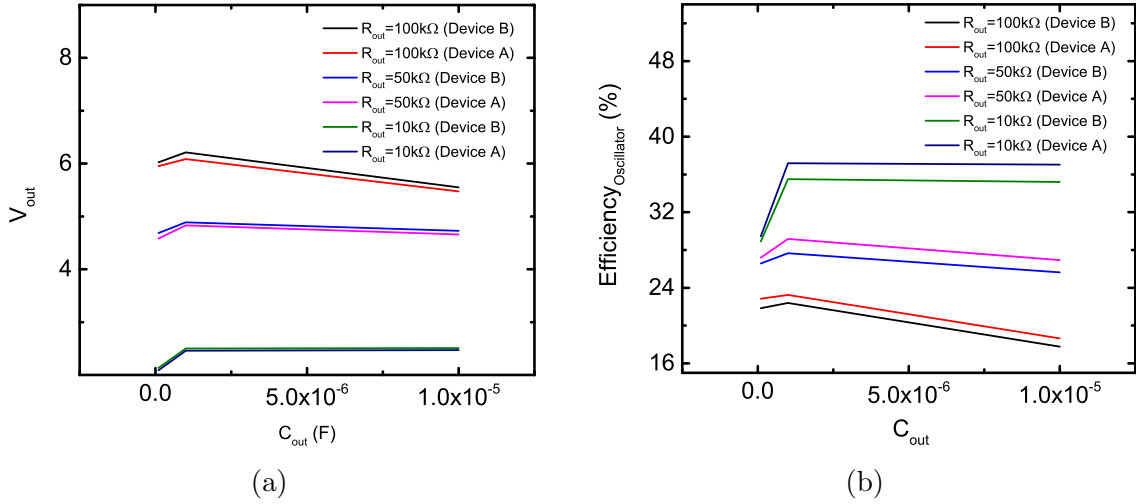


Figure 4.15: (a)  $V_{out}$  as a function of ripple capacitor  $C_{out}$  and (b) Efficiency as a function of ripple capacitor  $C_{out}$  of oscillator based converter

From the simulation results it is found that for device A the efficiency reaches a value of 37.19% while the output voltage lowers to a value of 2.416V when the RC value pair of oscillator circuit is taken as optimization (2) and  $R_{out}$ ,  $C_{out}$  value pair is taken as optimization (3). For the same value of optimization with device B an efficiency of 35.51% can be found where the output voltage lowers to a value of

Table 4.8: Optimization of the oscillator converter varying the RC parameters of the oscillator taking the optimized value of the output load and ripple capacitor [the numerical values in parenthesis indicate optimization value pair for  $R_{out}$  and  $C_{out}$ ]

Device A					
Optimized $R_{out}$ ( $\Omega$ )	Optimized $C_{out}$ (F)	Oscillator R ( $\Omega$ )	Oscillator C (F)	$V_{out}$ (V)	$\eta_{oscillator}$ (%)
100k (1)	1E-06 (1)	100k	1E-08	5.821	23.95
		1M	1E-09	6.085	23.24
50k (2)	1E-06 (2)	100k	1E-08	4.657	28.91
		1M	1E-09	4.831	29.18
10k (3)	1E-06 (3)	100k	1E-08	2.312	36.85
		1M	1E-09	2.461	37.19
Device B					
Optimized $R_{out}$ ( $\Omega$ )	Optimized $C_{out}$ (F)	Oscillator R ( $\Omega$ )	Oscillator C (F)	$V_{out}$ (V)	$\eta_{oscillator}$ (%)
100k (1)	1E-06 (1)	100k	1E-08	6.021	22.11
		1M	1E-09	6.211	22.40
50k (2)	1E-06 (2)	100k	1E-08	4.732	26.78
		1M	1E-09	4.887	27.66
10k (3)	1E-06 (3)	100k	1E-08	2.486	35.12
		1M	1E-09	2.501	35.51

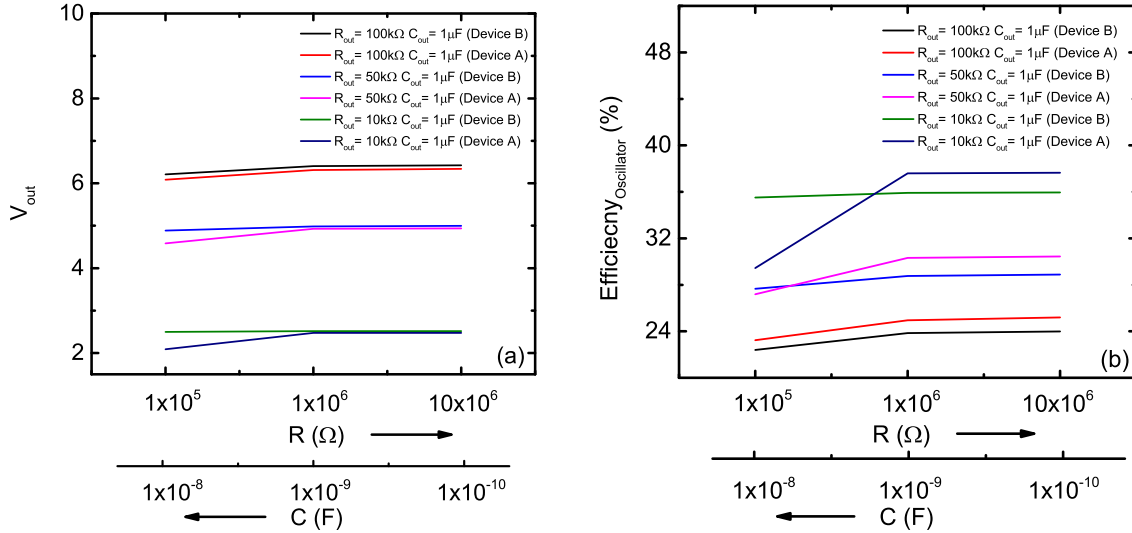


Figure 4.16: (a)  $V_{out}$  as a function of RC oscillator value pairs and (b) Efficiency as a function of RC oscillator value pairs of oscillator based converter

2.501V. Thus it can be summarized that with high  $R$  and  $C$  value of the oscillator circuit and low value of the output circuit higher efficiency of the converter circuit can be achieved at the cost of output voltage. Similarly with low value of the oscillator circuit and high value of the output circuit higher voltage can be achieved at the cost of low efficiency. These assumptions hold for both device A and device B taken as the source.

For having further insight into the design and optimization of the oscillator circuit of the boost converter, its transient characteristics are analyzed with device B since this source is the improved proposed structure. This should be noted that the results here corresponds to the highest and the lowest values of the output voltage from Table 4.8. As can be observed from Figure 4.17(a), when the choice of resistance-capacitor combination results in the highest output voltage, changing the value of  $R$  and  $C$  of the oscillator circuit negligibly influences both the magnitude and shape of  $V_{out}$ . The output steady state voltage remains at  $\sim 6V$  in this case. Comparison between Figure 4.17(a) and 4.17(b) however indicates that changing the values of  $R_{out}$  and  $C_{out}$  has significant impact on the shape of the transient characteristics and thereby on the output voltage level. In spite of the small ripple voltage, the steady state output voltage is only  $\sim 2V$  in this case. It is also noteworthy that changing the values of  $R$  and  $C$  of the oscillator circuit

has comparatively more significant influence on the transient and steady-state output voltage when the load resistance is reduced 10 times for the case shown in Figure 4.17(b), in comparison with the case considered in Figure 4.17(a). Hence, reducing the load resistance value results in greater dependence of the output voltage characteristics on the R-C tank oscillator circuit. The resistance-capacitor combinations considered in Figure 4.17(a) though result in high output voltage, the output efficiency remains low at about  $\sim 22\%$  in comparison with the  $\sim 36\%$  efficiency obtained for the case considered in Figure 4.17(b). This can be attributed to the high ripple voltage obtained for the case of Figure 4.17(a), which is much smaller for the case considered in Figure 4.17(b).

Finally, transient characteristics of the inductor current ( $I_L$ ) are shown in Figure 4.17(c) and 4.17(d) for the  $R_{out}$ ,  $C_{out}$  and R, C values considered in Figure 4.17(a) and 4.17(b). This reveals that the specific shape of the output voltage transient emanates from the particular shape of the currents, which are both quantitatively and qualitatively different when  $R_{out}$  and  $C_{out}$  are changed. Changing the values of R and C components of the oscillator circuit appears to have negligible effect on the shape and value of the transient currents. Hence in terms of both output voltage and inductor/switching current, the load resistor and capacitor combination appears to have dominant role in the circuit under consideration and therefore they serve as the main design parameters as far as design optimization is concerned.

## 4.5 Output Response in Array Formation

In order to find out the output response of the oscillator circuit, device B is connected in array formation. At first device B is connected in series starting with one device and subsequently four such devices are connected sequentially. The simulation is run in the boundary condition of device B as mentioned in Table 4.3, for each case and the output voltage is observed. In theory any DC-DC converter will change any input voltage according to the formula of the duty cycle as long as the current remains more or less proportional with the input voltage. In this

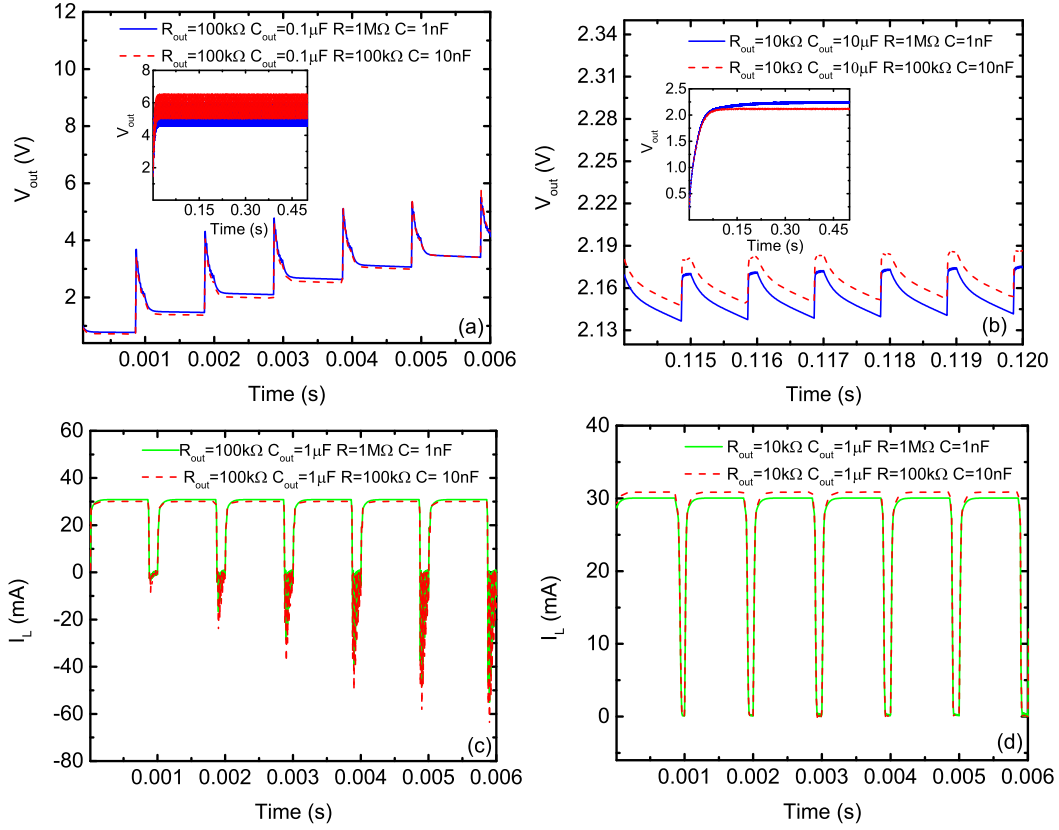


Figure 4.17: (a) Transient value of  $V_{out}$  with  $R_{out}$  at the highest optimized value,  $C_{out}$  at the lowest optimized value and varying  $R, C$  [inset: steady state value of  $V_{out}$ ]; (b) Transient value of  $V_{out}$  with  $R_{out}$  at the lowest optimized value,  $C_{out}$  at the highest optimized value and varying  $R, C$  [inset: steady state value of  $V_{out}$ ]; (c) Transient value of inductor current ( $I_L$ ) with  $R_{out}$  at the highest optimized value,  $C_{out}$  at the lowest optimized value and varying  $R, C$ ; (d) Transient value of inductor current ( $I_L$ ) with  $R_{out}$  at the lowest optimized value,  $C_{out}$  at the highest optimized value and varying  $R, C$

particular arrangement when device B is connected in series the input voltage increases algebraically but the input current increases ever so slightly and becomes saturated when four device B are connected in series formation. This phenomenon causes the output voltage to be saturated. Similar phenomenon is observed when four device B are connected in parallel formation in this case the input voltage becomes saturated but the current increases more or less linearly. The whole output response is tabulated in Table 4.9.

Before connecting the photovoltaic device in series or in parallel with the converter some precautionary measures needs to be taken. As this might happen that one or more photovoltaic device might not get the entire illumination. As

Table 4.9: Output response in array formation of the oscillator circuit with device B [The average values are tabulated]

Device B	One Device		
$V_{out}$ (V)	5.082		
$V_{in}$ (mV)	150.460		
$I_{in}$ (mA)	23.020		
Series Connection			
Device B	2 Devices in Series	3 Devices in Series	4 Devices in Series
$V_{out}$ (V)	8.081	8.715	9.072
$V_{in}$ (mV)	270.180	387.140	511.970
$I_{in}$ (mV)	24.734	26.400	26.443
Parallel Connection			
Device B	2 Devices in Parallel	3 Devices in Parallel	4 Devices in Parallel
$V_{out}$ (V)	6.296	7.402	8.489
$V_{in}$ (mV)	168.912	185.642	201.775
$I_{in}$ (mV)	48.588	69.891	92.618

a result the output voltage of the partially lighted photovoltaic device would be lower and this will start to consume energy from the surrounding photovoltaic devices. And further measures should be taken if there is interruption in the lighting condition. The measures are listed as follows:

- When the photovoltaic devices are connected in series there needs to be a blocking diode in series with every photovoltaic device. As a result the partially illuminated photovoltaic device will not be able to consume energy as current will flow only in one direction.
- When the photovoltaic devices are connected in parallel a bypass diode needs to be connected in parallel with every photovoltaic device. The diode will bypass the partially illuminated photovoltaic device so that it cannot consume energy.
- In case there is interruption of the illumination, back up supply like a battery should be provided. In this particular situation there should be a blocking diode so that when the battery is providing energy to the load the photovoltaic device cannot consume energy.

The measures discussed above suffer from one drawback. There will be a drop of voltage across each diode. Depending on the requirement if the voltage drop outweighs the benefit provided by the diode, the measures may be taken.

## 4.6 Discussion of Results

In the last part of the simulation study the transient analysis is done extensively to check the performance of both the devices with a conventional converter in both continuous conduction mode (CCM) and discontinuous conduction mode (DCM) and then with the oscillator-based converter. The transient analysis revealed that the conventional boost converter circuit in continuous conduction mode takes the longest time to reach the steady state, followed by the conventional boost converter in discontinuous conduction mode. The oscillator-based converter circuit reaches steady state a lot quicker compared to the conventional boost converter. The inductor current goes negative for a conventional boost converter operating in the discontinuous conduction mode and also with the oscillator-based converter circuit. While comparing the speed of steady state reached with the type of photovoltaic device used a quite unique feature is discovered. Device A reaches steady state quicker with both conventional converter and oscillator based converter.

There is another unique feature exclusive with oscillator based converter. From the transient response it is observed that the output voltage rises in staircase formation but unlike a conventional converter there is a peak at every rising step of the output voltage. This is caused when the capacitor of the oscillator circuit gets charged and subsequently discharged. This particular feature results in much higher output voltage with the oscillator based converter compared with a conventional converter. But this feature comes with another drawback; as seen from the efficiency data the conventional converter is 60% efficient where as the oscillator based converter is 36% efficient under optimized condition. This lower efficiency is also the result of the oscillator circuit. But in calculating the efficiency of the conventional converter the power requirement of the switching driver circuit is neglected and unlike a conventional converter the oscillator based converter is



self driving which makes up for the lower efficiency.

For optimization phase of the oscillator based converter the output circuit elements of the converter have a dominating effect when compared with the oscillator circuit element of the converter.

Thus, the final finding is that a photovoltaic device with better performance parameter will perform better with a conventional converter operating in CCM. On the other hand, a photovoltaic device with higher current density and lower output voltage performs better in efficiency of the converter when compared to a photovoltaic device with lower current density and higher output voltage even though its overall photovoltaic efficiency may be more when operated with a converter circuit operating in DCM. And the DCM operation of boost converter is similar to the operation of the oscillator-based converter.

# Chapter 5

## Conclusion

### 5.1 Summary of the Work

Photovoltaic device as renewable form of energy has been a part of research for quite a while now. It has been mainly designed for high intensity outdoor illumination for producing bulk amount of power. The thin film photovoltaic device technology has seen the light of research in space for being light weight where also the research focus has been the outdoor illumination. Now with everything being interconnected and the IoTs being ubiquitous, it is high time photovoltaic device research should focus on energy harvesting. In this study low cost thin material for photovoltaic device has been examined extensively with both indoor and outdoor illumination. Apart from the study of the device physics of thin film material based on spectra, intensive analysis of the photovoltaic device in circuit level has also been the major focus of this study.

To understand the device physics of thin film photovoltaic device, fundamental figure of merits such as the short circuit current, open circuit voltage, fill factor and efficiency have been discussed for photovoltaic devices in general. With a view to energy harvesting both solar irradiation and indoor illuminance have been derived and as such difference between the two has been established. Detailed balance theory has also been derived and with the help of this spectra dependent maximum efficiency under outdoor and indoor condition has also been formulated.

In this study low cost thin material has been studied extensively. In order to know the viability of the low-cost material the technology behind thin film industry has been given an in-depth review. Knowing the current trend in thin film industry, the absorber layer (CZTSSe) has been selected along with the other supporting layers with its associated material parameter like the buffer layer, transparent conducting oxide layer and the metal contact.

After selection of a low-cost material (CZTSSe), the current champion cell with this material has been selected which takes account of low-cost non-vacuum technique for fabrication referred in this study as device A. Here 1-D Poisson's equation, continuity equation and drift-diffusion equation considering both generation and recombination rate have been solved to model device A. With the theoretical validation of device A its performance enhancement has been done with a commercially available white LED. With an in-depth understanding of the indoor light spectrum it has been formulated that device A performs better with the white LED spectrum under all level of illumination when compared with sun light at similar level of illumination.

To get a detailed know how about the performance enhancement under indoor lighting the relative increase in the percentage of short current, open circuit voltage, fill factor and efficiency has been depicted. It has been understood that the relative enhancement of short circuit current is more for high illumination whereas the low illumination is dominated by both open circuit voltage and fill factor. This particular finding is useful for operating the photovoltaic device under low level of illumination.

It has been discovered that the relative enhancement of both short circuit current and open circuit voltage is attributed to photon yield where high level of photon yield is obtained for white LED (~100%) and medium of level of photon yield is obtained for solar spectrum (60-75%). Though high level of photon yield is obtained for white LED, performance enhancement of the device remains marginal. It has been found in this study that this marginal enhancement is related to the external quantum efficiency where external quantum efficiency has the highest peak

near the 2.5eV of photon energy and in this range the photon yield remains same for both solar and white LED spectrum. This is also verified by spectral response which has higher enhancement above 3.5eV of photon energy, indicative of better performance in short wavelength region. The generation rate profile of the material has also been analyzed extensively which suggests higher generation near the p-n junction comprising of short wavelength, also indicative of better performance under white LED.

In this study a new structure has been proposed which takes account of lower open circuit voltage, a particular trait of device A. This new structure has been named as the improved structure and referred in this study as device B. In the improved structure the ITO-based transparent conducting oxide has been replaced with ZnO and the n-type ZnO in device A has also been replaced with intrinsic ZnO. This resulted in a type II energy band gap in device B unlike the type I energy band gap seen in device A and as a consequence resulted in higher open circuit voltage. Here it is also found that the higher open circuit voltage is the result of charge separation of photo-generated carriers due to the intrinsic ZnO. But this higher open circuit voltage resulted in both lower short circuit current and fill factor. This increase in voltage resulted in overall performance enhancement (efficiency) for device B. The performance enhancement holds true for all level of illumination in both indoor and outdoor lighting condition as compared to device A.

In order to verify the performance of both the photovoltaic devices with an actual load, a converter circuit particularly suitable with the photovoltaic device is analyzed in great details. The use of the converter circuit is for the up conversion of the output voltage, since the output voltage available for a photovoltaic device is very low and not suitable for driving a practical load. The converter circuit selected in this study is an oscillator-based converter dependent on the architecture of a conventional boost converter. The unique feature of this particular converter is that it does not need a driving circuit for switching the transistor used in the design. The self-driving oscillator-based converter provided large enough output voltage for driving a load when paired with both the photovoltaic devices. But when the

output efficiency of the converter is compared with both the photovoltaic devices, an interesting feature is discovered in this study. Device A showed better efficiency with the converter when compared with the same experimental setup taking device B into consideration. In order to verify this concept extensive simulation was done varying the fill factor, open circuit voltage and short circuit current of both the cells and each time the simulation leads to the same result.

To find out the output response of the photovoltaic devices with a conventional boost converter, two modes of operation is selected. They are the continuous conduction mode (CCM) and discontinuous conduction mode (DCM). Device B showed better efficiency with the conventional converter in CCM when compared with device A. On the other hand, device A had better efficiency in DCM operation. The output voltage remained similar with both cells with a conventional converter though it is lower when compared with the oscillator-based converter.

In this study when both converters (oscillator-based and conventional) were compared with both the photovoltaic devices, the efficiency of oscillator-based converter was  $\sim 36\%$  where as the efficiency of the conventional converter was  $\sim 60\%$ . The output voltage of the oscillator-based converter was more than 5V and for the conventional converter it is  $\sim 3V$ . The oscillator-based converter reached steady state quickly compared to the conventional converter.

The better performance of device A with the oscillator-based converter is attributed to the negative inductor current as it is discovered from the simulation of conventional converter in DCM. In DCM the inductor current of conventional converter becomes negative. So, in this study it is hypothesized that when the inductor current becomes negative, the photovoltaic device with higher short circuit current will have better efficiency and the when the inductor current remains positive the photovoltaic device with higher open circuit voltage will have better efficiency.

## 5.2 Scopes of Future Works

A list of future works related to this study is as follows:

- 1D Poisson's equation has been solved in modeling the device physics of the photovoltaic device; 2-D Poisson's equation related to the device physics would have provided even more detailed analysis.
- CZTSSe, a low-cost earth abundant material has been selected as the absorber layer for the photovoltaic device. CZTS material could also have been studied employing similar non vacuum fabrication technique.
- In this study for indoor lighting condition white LED has been used. A detailed spectra dependent analysis of the absorber material could have provided in-depth knowledge relating to energy harvesting.
- Depending on the spectra, external quantum efficiency profile would have revealed other optimized absorber material and taking that material optimized photovoltaic device could have been fabricated.
- In this study power electronics converter have been studied for up conversion of the voltage. Depending on the application modular photovoltaic devices with suitable output voltage may have designed.
- Oscillator-based converter has been analyzed in this study. Charge pump-based converter though bulky could also have been analyzed which takes the concept of MEMS (Micro Electro-Mechanical System) in design analysis.

# Bibliography

- [1] M. A. Green, “The path to 25% silicon solar cell efficiency: History of silicon cell evolution,” *Progress in Photovoltaics: Research and Applications*, vol. 17, no. 3, pp. 183–189, 2009. [Online]. Available: <https://onlinelibrary.wiley.com/doi/abs/10.1002/pip.892>
- [2] D. Pulfrey and R. McOuat, “Schottky-barrier solar-cell calculations,” *Applied Physics Letters*, vol. 24, no. 4, pp. 167–169, 1974.
- [3] H. C. Card and E. S. Yang, “Electronic processes at grain boundaries in polycrystalline semiconductors under optical illumination,” *IEEE Transactions on Electron Devices*, vol. 24, no. 4, pp. 397–402, 1977.
- [4] M. V. Sullivan and J. H. Eigler, “Electroless nickel plating for making ohmic contacts to silicon,” *Journal of the electrochemical Society*, vol. 104, no. 4, pp. 226–230, 1957.
- [5] S. Flynn and A. Lennon, “Copper penetration in laser-doped selective-emitter silicon solar cells with plated nickel barrier layers,” *Solar Energy Materials and Solar Cells*, vol. 130, pp. 309–316, 2014.
- [6] M. Green and S. Wenham, “Australian patent no. 5703309,” 1984.
- [7] A. Blakers, J. Zhao, A. Wang, M. Milne, X. Dai, and M. Green, “23% efficient silicon solar cel,” in *9th European Communities Photovoltaic Science and Engineering Conference*. Dordrecht, The Netherlands: Kluwer, 1989, pp. 328–329.

- [8] M. A. Green, J. Zhao, A. Wang, and S. R. Wenham, “Very high efficiency silicon solar cells-science and technology,” *IEEE Transactions on electron devices*, vol. 46, no. 10, pp. 1940–1947, 1999.
- [9] L. B. Rubin and G. L. Rubin, “Electrode for photovoltaic cells, photovoltaic cell and photovoltaic module,” Oct. 7 2008, uS Patent 7,432,438.
- [10] A. Schneider, L. Rubin, G. Rubin, A. Osipov, A. Smirnov, and P. Antipov, “A new approach in solar cell module interconnection technique resulting in 5-10% higher pv module power output,” in *2006 IEEE 4th World Conference on Photovoltaic Energy Conference*, vol. 2. IEEE, 2006, pp. 2073–2076.
- [11] E. Maruyama, A. Terakawa, M. Taguchi, Y. Yoshimine, D. Ide, T. Baba, M. Shima, H. Sakata, and M. Tanaka, “Sanyo’s challenges to the development of high-efficiency hit solar cells and the expansion of hit business,” in *2006 IEEE 4th World Conference on Photovoltaic Energy Conference*, vol. 2. IEEE, 2006, pp. 1455–1460.
- [12] M. Green, Y. Hishikawa, E. Dunlop, D. H. Levi, J. Hohl-Ebinger, and A. Ho-Baillie, “Solar cell efficiency tables (version 51),” *Progress in Photovoltaics*, vol. 26, pp. 3–12, Dec 2017.
- [13] R. M. Swanson, “Method of fabricating back surface point contact solar cells,” May 22 1990, uS Patent 4,927,770.
- [14] R. Hall, R. Birkmire, J. Phillips, and J. Meakin, “Thin-film polycrystalline  $\text{Cu}_2\text{S}/\text{Cd}_{1-x}\text{Zn}_x\text{S}$  solar cells of 10% efficiency,” *Applied Physics Letters*, vol. 38, no. 11, pp. 925–926, 1981.
- [15] A. Goetzberger and V. U. Hoffmann, *Photovoltaic solar energy generation*. Springer Science & Business Media, 2005, vol. 112.
- [16] I. Repins, M. A. Contreras, B. Egaas, C. DeHart, J. Scharf, C. L. Perkins, B. To, and R. Noufi, “19.9%-efficient  $\text{ZnO}/\text{CdS}/\text{CuInGaSe}_2$  solar cell with 81.2% fill factor,” *Progress in Photovoltaics: Research and applications*, vol. 16, no. 3, pp. 235–239, 2008.



- [17] X. Wu, R. Dhere, D. Albin, T. Gessert, C. DeHart, J. Keane, A. Duda, T. Coutts, S. Asher, D. Levi *et al.*, “High-efficiency CTO/ZTO/CdS/CdTe polycrystalline thin-film solar cells,” National Renewable Energy Lab., Golden, CO.(US), Tech. Rep., 2001.
- [18] D. Abou-Ras, T. Kirchartz, and U. Rau, *Advanced characterization techniques for thin film solar cells*. Wiley Online Library, 2011.
- [19] D. E. Carlson and C. R. Wronski, “Amorphous silicon solar cell,” *Applied Physics Letters*, vol. 28, no. 11, pp. 671–673, 1976.
- [20] R. Chittick, J. Alexander, and H. Sterling, “The preparation and properties of amorphous silicon,” *Journal of the Electrochemical Society*, vol. 116, no. 1, pp. 77–81, 1969.
- [21] J. Poortmans and V. Arkhipov, *Thin film solar cells: fabrication, characterization and applications*. John Wiley & Sons, 2006, vol. 5.
- [22] D. Staebler and C. Wronski, “Reversible conductivity changes in discharge-produced amorphous si,” *Applied physics letters*, vol. 31, no. 4, pp. 292–294, 1977.
- [23] M. Stutzmann, W. Jackson, and C. Tsai, “Annealing of metastable defects in hydrogenated amorphous silicon,” *Physical Review B*, vol. 34, no. 1, p. 63, 1986.
- [24] H. M. Branz, “Hydrogen collision model: Quantitative description of metastability in amorphous silicon,” *Physical Review B*, vol. 59, no. 8, p. 5498, 1999.
- [25] J. Meier, S. Dubail, R. Fluckiger, D. Fischer, H. Keppner, and A. Shah, “Intrinsic microcrystalline silicon ( $\mu/c$ -Si: H)-a promising new thin film solar cell material,” in *Proceedings of 1994 IEEE 1st World Conference on Photovoltaic Energy Conversion-WCPEC (A Joint Conference of PVSC, PVSEC and PSEC)*, vol. 1. IEEE, 1994, pp. 409–412.

- [26] M. A. Green, “Third generation photovoltaics: Ultra-high conversion efficiency at low cost,” *Progress in Photovoltaics: Research and Applications*, vol. 9, no. 2, pp. 123–135, 2001.
- [27] A. De Vos, “Detailed balance limit of the efficiency of tandem solar cells,” *Journal of Physics D: Applied Physics*, vol. 13, no. 5, p. 839, 1980.
- [28] R. King, D. Law, K. Edmondson, C. Fetzer, G. Kinsey, H. Yoon, R. Sherif, and N. Karam, “40% efficient metamorphic GaInP/ GaInAs/ Ge multijunction solar cells,” *Applied physics letters*, vol. 90, no. 18, p. 183516, 2007.
- [29] J. Geisz, D. Friedman, J. Ward, A. Duda, W. Olavarria, T. Moriarty, J. Kiehl, M. Romero, A. Norman, and K. Jones, “40.8% efficient inverted triple-junction solar cell with two independently metamorphic junctions,” *Applied Physics Letters*, vol. 93, no. 12, p. 123505, 2008.
- [30] N. Reichl, “Weak light performance and spectral response of different solar cell types,” *20th EUPVSEC, 2005*, 2005.
- [31] J. Randall and J. Jacot, “Is AM1. 5 applicable in practice? modelling eight photovoltaic materials with respect to light intensity and two spectra,” *Renewable Energy*, vol. 28, no. 12, pp. 1851–1864, 2003.
- [32] A. S. Teran, J. Wong, W. Lim, G. Kim, Y. Lee, D. Blaauw, and J. D. Phillips, “AlGaAs photovoltaics for indoor energy harvesting in mm-scale wireless sensor nodes,” *IEEE Transactions on Electron Devices*, vol. 62, no. 7, pp. 2170–2175, 2015.
- [33] A. S. Teran, E. Moon, W. Lim, G. Kim, I. Lee, D. Blaauw, and J. D. Phillips, “Energy harvesting for gaas photovoltaics under low-flux indoor lighting conditions,” *IEEE transactions on electron devices*, vol. 63, no. 7, pp. 2820–2825, 2016.
- [34] I. Mathews, P. J. King, F. Stafford, and R. Frizzell, “Performance of III–V solar cells as indoor light energy harvesters,” *IEEE Journal of Photovoltaics*, vol. 6, no. 1, pp. 230–235, 2015.

- [35] J. Russo, W. Ray II, and M. S. Litz, “Low light illumination study on commercially available homojunction photovoltaic cells,” *Applied energy*, vol. 191, pp. 10–21, 2017.
- [36] V. Janošević, M. Mitrić, N. Bundaleski, Z. Rakočević, and I. L. Validžić, “High-efficiency  $\text{Sb}_2\text{S}_3$ -based hybrid solar cell at low light intensity: cell made of synthesized Cu and Se-doped  $\text{Sb}_2\text{S}_3$ ,” *Progress in Photovoltaics: Research and Applications*, vol. 24, no. 5, pp. 704–715, 2016.
- [37] G. Lucarelli, F. Di Giacomo, V. Zardetto, M. Creatore, and T. M. Brown, “Efficient light harvesting from flexible perovskite solar cells under indoor white light-emitting diode illumination,” *Nano Research*, vol. 10, no. 6, pp. 2130–2145, 2017.
- [38] F. Di Giacomo, V. Zardetto, G. Lucarelli, L. Cinà, A. Di Carlo, M. Creatore, and T. Brown, “Mesoporous perovskite solar cells and the role of nanoscale compact layers for remarkable all-round high efficiency under both indoor and outdoor illumination,” *Nano Energy*, vol. 30, pp. 460–469, 2016.
- [39] A. F. Jaimes and F. R. de Sousa, “Simple modeling of photovoltaic solar cells for indoor harvesting applications,” *Solar Energy*, vol. 157, pp. 792–802, 2017.
- [40] G. Apostolou, A. Reinders, and M. Verwaal, “Comparison of the indoor performance of 12 commercial pv products by a simple model,” *Energy science & engineering*, vol. 4, no. 1, pp. 69–85, 2016.
- [41] M. Katiyar, M. van Balkom, C. C. Rindt, C. de Keizer, and H. A. Zondag, “Numerical model for the thermal yield estimation of unglazed photovoltaic-thermal collectors using indoor solar simulator testing,” *Solar Energy*, vol. 155, pp. 903–919, 2017.
- [42] D. Lee, “Energy harvesting chip and the chip based power supply development for a wireless sensor network,” *Sensors*, vol. 8, no. 12, pp. 7690–7714, 2008.
- [43] C. Wang and Z. Li, “A review of start-up circuits for low voltage self-powered dc-type energy harvesters,” *Journal of Circuits, Systems and Computers*, vol. 25, no. 07, p. 1630003, 2016.

- [44] M. Pollak, L. Mateu, and P. Spies, “Step-up dc-dc-converter with coupled inductors for low input voltages,” *Fraunhofer IIS*, vol. 86, pp. 625–632, 2008.
- [45] W. Shockley and H. J. Queisser, “Detailed balance limit of efficiency of p-n junction solar cells,” *Journal of Applied Physics*, vol. 32, pp. 510 – 519, Apr 1961.
- [46] W. Wang, M. T. Winkler, O. Gunawan, T. Gokmen, T. K. Todorov, Y. Zhu, and D. B. Mitzi, “Device characteristics of CZTSSe thin-film solar cells with 12.6% efficiency,” *Advanced Energy Materials*, vol. 4, May 2014.
- [47] I. Repins, J. V. Li, A. Kanevce, C. Perkins, K. Steirer, J. Pankow, G. Teeter, D. Kuciauskas, C. Beall, C. Dehart *et al.*, “Effects of deposition termination on  $Cu_2ZnSnSe_4$  device characteristics,” *Thin Solid Films*, vol. 582, pp. 184–187, 2015.
- [48] S. Merdes, R. Mainz, J. Klaer, A. Meeder, H. Rodriguez-Alvarez, H. Schock, M. C. Lux-Steiner, and R. Klenk, “12.6% efficient CdS/Cu (In, Ga)  $S_2$ -based solar cell with an open circuit voltage of 879 mv prepared by a rapid thermal process,” *Solar Energy Materials and Solar Cells*, vol. 95, no. 3, pp. 864–869, 2011.
- [49] M. Bhushan and A. Catalano, “Polycrystalline  $Zn_3P_2$  schottky barrier solar cells,” *Applied Physics Letters*, vol. 38, no. 1, pp. 39–41, 1981.
- [50] G. M. Kimball, A. M. Müller, N. S. Lewis, and H. A. Atwater, “Photoluminescence-based measurements of the energy gap and diffusion length of  $Zn_3P_2$ ,” *Applied Physics Letters*, vol. 95, no. 11, p. 112103, 2009.
- [51] J. P. Bosco, S. B. Demers, G. M. Kimball, N. S. Lewis, and H. A. Atwater, “Band alignment of epitaxial  $ZnS/Zn_3P_2$  heterojunctions,” *Journal of Applied Physics*, vol. 112, no. 9, p. 093703, 2012.
- [52] H. Känel, R. Hauger, and P. Wachter, “Photoelectrochemistry of monoclinic  $ZnP_2$ : A promising new solar cell material,” *Solid State Communications*, vol. 43, no. 8, pp. 619–621, 1982.
- [53] R. H. Bube and R. H. Bube, “Photovoltaic materials,” 1998.

- [54] M. Konagai, M. Sugimoto, and K. Takahashi, “High efficiency GaAs thin film solar cells by peeled film technology,” *Journal of crystal growth*, vol. 45, pp. 277–280, 1978.
- [55] K. Ito and H. Ito, “Growth of p-type InP single crystals by the temperature gradient method,” *Journal of Crystal Growth*, vol. 45, pp. 248–251, 1978.
- [56] K. Ito and T. Nakazawa, “n-In<sub>2</sub>O<sub>3</sub>/p-InP solar cells,” *Surface Science*, vol. 86, pp. 492–497, 1979.
- [57] K. Ito and T. N., “Heat-resisting and efficient indium oxide/indium phosphide heterojunction solar cells,” *Journal of applied physics*, vol. 58, no. 7, pp. 2638–2639, 1985.
- [58] S. Saito, Y. Hashimoto, and K. Ito, “Efficient ZnO/CdS/InP heterojunction solar cell,” in *Proceedings of 1994 IEEE 1st World Conference on Photovoltaic Energy Conversion-WCPEC (A Joint Conference of PVSC, PVSEC and PSEC)*, vol. 2. IEEE, 1994, pp. 1867–1870.
- [59] C. Keavney, V. Haven, and S. Vernon, “Emitter structures in MOCVD InP solar cells,” in *IEEE Conference on Photovoltaic Specialists*. IEEE, 1990, pp. 141–144.
- [60] K. Ito, “An overview of CZTS-based thin-film solar cells,” *Copper Zinc Tin Sulfide-Based Thin Film Solar Cells*, 2015.
- [61] T. Nakazawa, K. Takamizawa, and K. Ito, “High efficiency indium oxide/cadmium telluride solar cells,” *Applied physics letters*, vol. 50, no. 5, pp. 279–280, 1987.
- [62] K. Ito, N. Matsumoto, T. Horiuchi, K. Ichino, H. Shimoyama, T. Ohashi, Y. Hashimoto, I. Hengel, J. Beier, R. Klenk *et al.*, “Theoretical model and device performance of CuInS<sub>2</sub> thin film solar cell,” *Japanese Journal of Applied Physics*, vol. 39, no. 1R, p. 126, 2000.
- [63] K. Zanio, “Cadmium telluride,” *Semiconductor and semimetals*, vol. 13, p. 34, 1978.

- [64] A. D. Compaan, “The status of and challenges in CdTe thin-film solar-cell technology,” *MRS Online Proceedings Library Archive*, vol. 808, 2004.
- [65] Y. Ogawa, A. Jäger-Waldau, Y. Hashimoto, and K. Ito, “In<sub>2</sub>O<sub>3</sub>/CdS/CuInS<sub>2</sub> thin-film solar cell with 9.7% efficiency,” *Japanese journal of applied physics*, vol. 33, no. 12B, p. L1775, 1994.
- [66] T. Nakabayashi, T. Miyazawa, Y. Hashimoto, and K. Ito, “Over 10% efficient CuInS<sub>2</sub> solar cell by sulfurization,” *Solar energy materials and solar cells*, vol. 49, no. 1-4, pp. 375–381, 1997.
- [67] T. Ohashi, M. Wakamori, Y. Hashimoto, and K. Ito, “Cu(In<sub>1-x</sub>Ga<sub>x</sub>)S<sub>2</sub> thin films prepared by sulfurization of precursors consisting of metallic and gallium sulfide layers,” *Japanese journal of applied physics*, vol. 37, no. 12R, p. 6530, 1998.
- [68] H. Goto, Y. Hashimoto, and K. Ito, “Efficient thin film solar cell consisting of TCO/CdS/CuInS<sub>2</sub>/CuGaS<sub>2</sub> structure,” *Thin Solid Films*, vol. 451, pp. 552–555, 2004.
- [69] P. Jackson, D. Hariskos, E. Lotter, S. Paetel, R. Wuerz, R. Menner, W. Wischmann, and M. Powalla, “New world record efficiency for Cu(In, Ga)Se<sub>2</sub> thin-film solar cells beyond 20%,” *Progress in Photovoltaics: Research and Applications*, vol. 19, no. 7, pp. 894–897, 2011.
- [70] C. Persson, “Electronic and optical properties of Cu<sub>2</sub>ZnSnS<sub>4</sub> and Cu<sub>2</sub>ZnSnSe<sub>4</sub>,” *Journal of Applied Physics*, vol. 107, no. 5, p. 053710, 2010.
- [71] N. Kamoun, H. Bouzouita, and B. Rezig, “Fabrication and characterization of Cu<sub>2</sub>ZnSnS<sub>4</sub> thin films deposited by spray pyrolysis technique,” *Thin Solid Films*, vol. 515, no. 15, pp. 5949–5952, 2007.
- [72] S. Ahn, S. Jung, J. Gwak, A. Cho, K. Shin, K. Yoon, D. Park, H. Cheong, and J. H. Yun, “Determination of band gap energy ( $E_g$ ) of Cu<sub>2</sub>ZnSnSe<sub>4</sub> thin films: on the discrepancies of reported band gap values,” *Applied Physics Letters*, vol. 97, no. 2, p. 021905, 2010.

- [73] H. Katagiri, N. Sasaguchi, S. Hando, S. Hoshino, J. Ohashi, and T. Yokota, “Preparation and evaluation of  $\text{Cu}_2\text{ZnSnS}_4$  thin films by sulfurization of E-B evaporated precursors,” *Solar Energy Materials and Solar Cells*, vol. 49, no. 1-4, pp. 407–414, 1997.
- [74] H. Katagiri, K. Saitoh, T. Washio, H. Shinohara, T. Kurumadani, and S. Miyajima, “Development of thin film solar cell based on  $\text{Cu}_2\text{ZnSnS}_4$  thin films,” *Solar Energy Materials and Solar Cells*, vol. 65, no. 1-4, pp. 141–148, 2001.
- [75] A. Redinger, D. M. Berg, P. J. Dale, and S. Siebentritt, “The consequences of kesterite equilibria for efficient solar cells,” *Journal of the American Chemical Society*, vol. 133, no. 10, pp. 3320–3323, 2011.
- [76] H. Katagiri, K. Jimbo, S. Yamada, T. Kamimura, W. S. Maw, T. Fukano, T. Ito, and T. Motohiro, “Enhanced conversion efficiencies of  $\text{Cu}_2\text{ZnSnS}_4$ -based thin film solar cells by using preferential etching technique,” *Applied physics express*, vol. 1, no. 4, p. 041201, 2008.
- [77] X. Song, X. Ji, M. Li, W. Lin, X. Luo, and H. Zhang, “A review on development prospect of CZTS based thin film solar cells,” *International Journal of Photoenergy*, vol. 2014, 2014.
- [78] G. Zoppi, I. Forbes, R. W. Miles, P. J. Dale, J. J. Scragg, and L. M. Peter, “ $\text{Cu}_2\text{ZnSnSe}_4$  thin film solar cells produced by selenisation of magnetron sputtered precursors,” *Progress in Photovoltaics: Research and Applications*, vol. 17, no. 5, pp. 315–319, 2009.
- [79] D. B. Mitzi, M. Yuan, W. Liu, A. J. Kellock, S. J. Chey, V. Deline, and A. G. Schrott, “A high-efficiency solution-deposited thin-film photovoltaic device,” *Advanced Materials*, vol. 20, no. 19, pp. 3657–3662, 2008.
- [80] R. Varache, C. Leendertz, M. Gueunier-Farret, J. Haschke, D. Muñoz, and L. Korte, “Investigation of selective junctions using a newly developed tunnel current model for solar cell applications,” *Solar Energy Materials and Solar Cells*, vol. 141, pp. 14–23, Oct 2015.

- [81] X. Yang, C. Xu, and N. Giles, “Intrinsic electron mobilities in CdSe, CdS, ZnO, and ZnS and their use in analysis of temperature-dependent hall measurements,” *Journal of Applied Physics*, vol. 104, no. 7, p. 073727, 2008.
- [82] O. Simya, A. Mahaboobbatcha, and K. Balachander, “A comparative study on the performance of kesterite based thin film solar cells using SCAPS simulation program,” *Superlattices and Microstructures*, vol. 82, pp. 248–261, 2015.
- [83] R. Scheer, “Towards an electronic model for  $CuIn_{1-x}Ga_xSe_2$  solar cells,” *Thin Solid Films*, vol. 519, no. 21, pp. 7472–7475, 2011.
- [84] A. Redinger, M. Mousel, M. H. Wolter, N. Valle, and S. Siebentritt, “Influence of S/Se ratio on series resistance and on dominant recombination pathway in  $Cu_2ZnSn(S,Se)_4$  thin film solar cells,” *Thin Solid Films*, vol. 535, pp. 291–295, 2013.
- [85] K. Jacobi, G. Zwicker, and A. Gutmann, “Work function, electron affinity and band bending of zinc oxide surfaces,” *Surface Science*, vol. 141, no. 1, pp. 109–125, 1984.
- [86] R. Islam, K. N. Nazif, and K. C. Saraswat, “Si heterojunction solar cells: A simulation study of the design issues,” *IEEE Transactions on Electron Devices*, vol. 63, no. 12, pp. 4788–4795, 2016.
- [87] R. Herberholz, M. Igalson, and H. Schock, “Distinction between bulk and interface states in  $CuInSe_2/CdS/ZnO$  by space charge spectroscopy,” *Journal of Applied Physics*, vol. 83, no. 1, pp. 318–325, 1998.
- [88] T. Gokmen, O. Gunawan, and D. B. Mitzi, “Semi-empirical device model for  $Cu_2ZnSn(S,Se)_4$  solar cells,” *Applied Physics Letters*, vol. 105, no. 3, p. 033903, 2014.
- [89] J. Xu, J. Lin, and C. Zhuang, “Analysis of the open-circuit voltage of  $Cu_2ZnSn(S,Se)_4$  thin film solar cell,” *Solar Energy*, vol. 164, pp. 231–242, 2018.
- [90] M. Courel, F. Pulgarín-Agudelo, J. Andrade-Arvizu, and O. Vigil-Galán, “Open-circuit voltage enhancement in CdS/ $Cu_2ZnSn(S,Se)_4$ -based thin film



- solar cells: A metal–insulator–semiconductor (mis) performance,” *Solar Energy Materials and Solar Cells*, vol. 149, pp. 204–212, 2016.
- [91] J. Robertson and B. Falabretti, “Electronic structure of transparent conducting oxides,” in *Handbook of transparent conductors*. Springer, 2011, pp. 27–50.
- [92] J. Robertson and S. Clark, “Limits to doping in oxides,” *Physical Review B*, vol. 83, no. 7, p. 075205, 2011.
- [93] M. Gloeckler, A. Fahrenbruch, and J. Sites, “Numerical modeling of CIGS and CdTe solar cells: setting the baseline,” in *3rd World Conference on Photovoltaic Energy Conversion, 2003. Proceedings of*, vol. 1. IEEE, 2003, pp. 491–494.
- [94] S. Sze and K. Ng, “Physics of semiconductor devices 3rd edn john wiley & sons,” *Inc., New Jersey*, p. 293, 2007.
- [95] M. Freunek, M. Freunek, and L. M. Reindl, “Maximum efficiencies of indoor photovoltaic devices,” *IEEE Journal of Photovoltaics*, vol. 3, no. 1, pp. 59–64, 2012.
- [96] M. W. Rahman, “Fabrication and characterization of thin film solar cell using earth abundant elements,” Master’s thesis, Bangladesh University of Engineering and Technology, 8 2016.
- [97] S. Bag, O. Gunawan, T. Gokmen, Y. Zhu, T. K. Todorov, and D. B. Mitzi, “Low band gap liquid-processed CZTSe solar cell with 10.1% efficiency,” *Energy & Environmental Science*, vol. 5, no. 5, pp. 7060–7065, 2012.
- [98] N. Neves, R. Barros, E. Antunes, J. Calado, E. Fortunato, R. Martins, and I. Ferreira, “Aluminum doped zinc oxide sputtering targets obtained from nanostructured powders: processing and application,” *Journal of the European Ceramic Society*, vol. 32, no. 16, pp. 4381–4391, 2012.
- [99] A. Walsh, S. Chen, S.-H. Wei, and X.-G. Gong, “Kesterite thin-film solar cells: Advances in materials modelling of  $\text{Cu}_2\text{ZnSnS}_4$ ,” *Advanced Energy Materials*, vol. 2, no. 4, pp. 400–409, 2012.

- [100] K. Ito, *Copper zinc tin sulfide-based thin film solar cells*. Wiley Online Library, 2014.
- [101] J. Muth, R. Kolbas, A. Sharma, S. Oktyabrsky, and J. Narayan, “Excitonic structure and absorption coefficient measurements of ZnO single crystal epitaxial films deposited by pulsed laser deposition,” *Journal of Applied Physics*, vol. 85, no. 11, pp. 7884–7887, 1999.
- [102] N. Mohan, *Power electronics: a first course*. Wiley, 2011.
- [103] P. Spies, M. Pollak, and L. Mateu, *Handbook of energy harvesting power supplies and applications*. CRC Press, 2015.